

Relationship between microstructure and dynamic properties of metals, alloys and mmc

8th Technical Meeting, 1993
Ispra, Italy

TAYLOR TEST AND THE STRUCTURE OF METALS AND ALLOYS

Jan Krejčí, Petr Ptáček
Institute of Physical Metallurgy ASCR
Žižkova 22, 616 62 Brno, Czech Republic

Jaroslav Buchar
Department of Physics, University of Agriculture
Zemědělská 1, 613 00 Brno, Czech Republic

ABSTRACT

The results of structure analysis of Taylor test specimens from various FCC materials and plain carbon steel are presented. Methods used were: specimen profile measurement, hardness measurement, light and transmission electron microscopy. The results show that above some limiting impact velocity plastic deformation takes place affecting whole volume of the specimen. Interaction of plastic deformation propagating from the impact surface and reflected elastic stress wave gives rise to measurable effects.

1 INTRODUCTION

The Taylor test, i.e., the impact of accelerated cylindrical specimen on the rigid anvil, is commonly used for the determination of dynamic yield strength of metals and alloys. Different theoretical approaches (and thus different equations) basically require two parameters to be measured: impact velocities v_0 and X permanently deformed part of the specimen. The evaluation of Taylor test is principally based on two assumptions: The constancy of plastic front velocity and the existence of two distinguishable parts of specimen, permanently deformed and undeformed part [Jones, 1990]. This contribution is limited to the presentation of experimental results only. Few comments are added. Detail analysis of the results is out of its scope as it requires, according to our opinion, further experiments.

2 EXPERIMENTS

Specimens have diameter 5 mm and length 25 mm (few aluminium bronze polycrystals were 50 mm long). They were placed in light polyester sabots and accelerated by compressed air gun with highly polished 2 m long bar-

Table 1: Quasistatic stress characteristics and SFE of materials used

Material	yield stress [MPa]	UTS [MPa]	SFE [J/m ²]
Cu single crystal			0.040
Cu polycrystals		172	0.040
Cu3Al		330	0.030
Cu30Zn	108	229	0.012
18/8 austenitic steel	215	593	0.013

rel. Different impact velocities are achieved by varying compression time, v_0 was measured by a pair of photo-sensitive cells placed near the gun's exit. Anvil was made from maraging steel. Impact velocities up to 250 ms^{-1} were used. The specimens were Cu single crystals oriented for single slip and polycrystalline OFHC copper, aluminium bronze (3% Al), alpha brass (30% Zn) and cast 18/8 austenitic steel. Preliminary results are available on plain carbon (0.5 wt.% C) steel with different structures obtained by quenching and tempering in the range 150°C - 700°C. Static stress characteristics and stacking fault energies (SFE) are in Tab. 1.

Prior the experiments, the specimens were weighed and their diameters (profiles) were measured. After the impact specimens diameters were measured with 1 mm step along the specimen length. As the cross section of Cu single crystals and cast 18/8 austenite do not stay circular, these specimens were measured in two of planes

Table 2: Minimal impact velocity causing plastic deformation

Material	Minimal velocity [ms ⁻¹]
Cu single crystal	13.0
Cu polycrystal	23.0
Cu3Al	27.0
Cu30Zn	25.0
18/8 austenite	37.5

containing specimens axis. The values used in profile display are average of these measurements.

Some specimens were cut axially and the surface was prepared for light microscopy and hardness measurement. Other specimens were cut perpendicular to the axis for thin foil preparation. Thin foils were prepared in the following order: three foils from the impact surface vicinity (first contains this surface), three from the middle of the specimen (i.e., approximately 11.5, 12.5 and 13.5 mm from the impact surface) and three from the free end of the specimen (last containing it).

3 RESULTS

The Cu single crystals and cast austenite specimens do not retain circular cross section after the test. Both materials are anisotropic. Single crystals were oriented for single slip and final cross section is elliptic with main axis approximately parallel to the original slip direction. Cast austenite has a coarse structure of primary grains (cells) formed during solidification. Resulting shape the specimen is oval cross section which axis rotate along the axis of the specimen (screw-like).

These observations prove that the original structure (its anisotropy) influence the propagation of plastic deformation although more slip systems are always operative. Plain carbon steel specimens heat treated to high hardness (low tempering temperatures) often, especially at higher impact velocities ($> 100 \text{ ms}^{-1}$), fail by fracture. Fracture plain is roughly 45° inclined to the specimen's axis and starts at (or near) the edge of the impact surface. The structure in the proximity of fracture surface is similar to that of adiabatic shear bands.

Other materials remain circular in shape and do not fracture. Profile measurement showed three interesting features of FCC materials:

1. If limiting impact velocity (i.e., the velocity below which no plastic deformation takes place - see Tab. 2) is exceeded, whole length of the specimen undergoes permanent deformation.

2. At approximately 2 mm from impact surface a "tooth" appears on the profile. If longer specimens are used this "tooth" shifts from the impact surface (to roughly 3 mm).

3. Near the free end of the specimen, region where specimen diameter drops (often below its original value) exists.

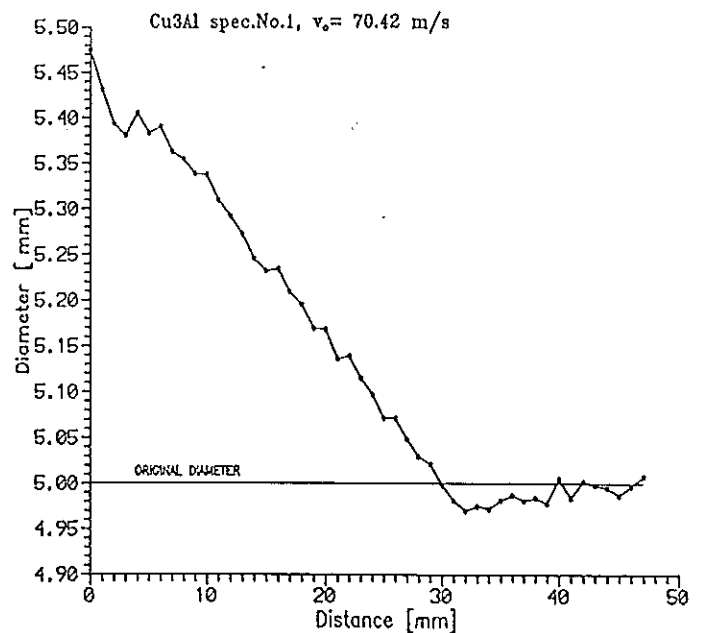


Figure 1: Changes of specimen diameter along the specimen length

Typical example of profile is in Fig. 1. The behaviour of BCC (steel) specimens is similar in character but characteristic features are less pronounced. Detail study of these structures' response to impact loading is anticipated. Hardness was measured on the axial section of the specimen. The values of HV 10 follow similar course as the specimen diameter including the "tooth" at approximately 2 mm from impact surface. The values of hardness remain above the initial ("virgin") value on whole length of the specimen (Fig. 2)

Light microscopy-revealed deformed structure with "smeared" region at ~ 2 mm from impact surface, i.e., in the region of the "tooth" - Fig. 3. Transmission electron microscopy (TEM) observation can be summarized as follows: In higher stacking fault energy material (copper) dislocation cell structure develops. The size of cells gradually increases with the distance from the impact surface (Fig. 4). The cell size in the vicinity of impact surface decreases with increasing impact velocity. The increase of cell size with distance is steady in polycrystals. In single crystals the increase in cell size is steep in the region adjacent to the impact surface, next comes the region of almost constant cell size which extends to the middle of the specimen followed by further rise of cell size (Fig. 5,6).

In materials with low SFE dislocation cells do not appear. The structure consists of high dislocation density that gradually decreases with distance from impact surface (more than one slip system always operative). Near the impact surface (especially at higher impact velocities) stacking faults and twin boundaries are often locally bent (Fig. 7); this is the evidence of high localized shear deformation.

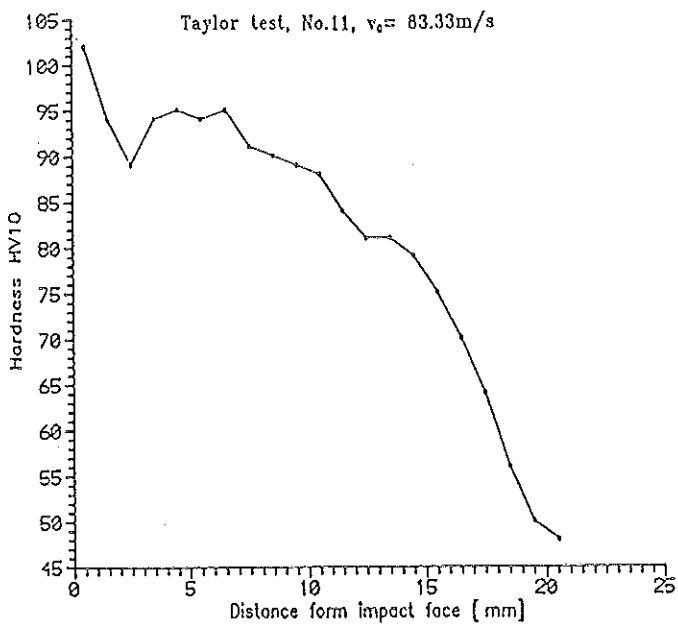


Figure 2: Hardness HV 10 along the specimen length, Cu polycrystal.

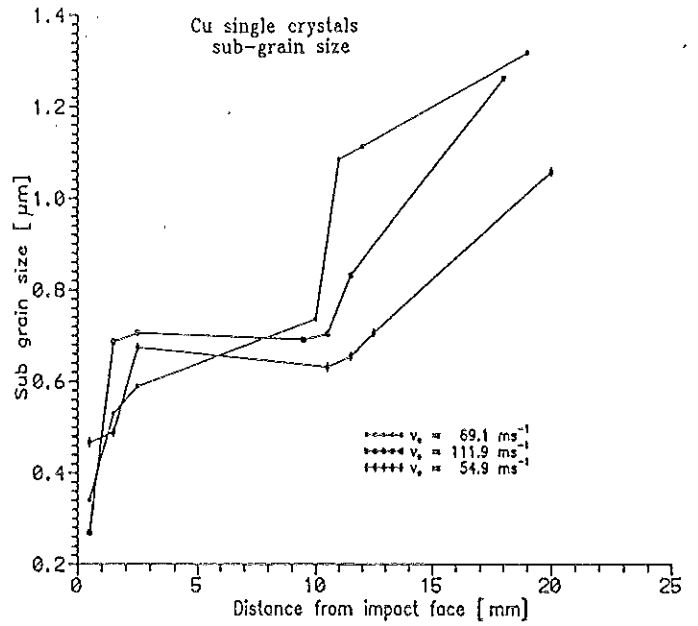


Figure 4: Dependence of sub-grain size on distance from impact surface

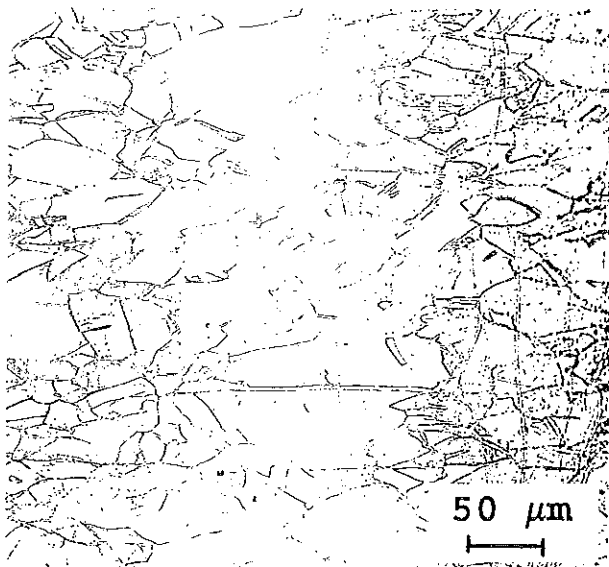


Figure 3: Cu polycrystal. Structure $\sim 2 \text{ mm}$ from impact surface. Light microscopy.

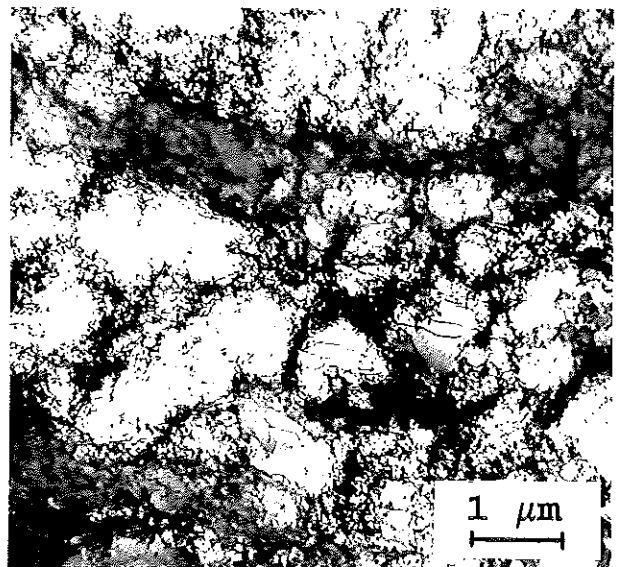


Figure 5: Cu single crystal. The structure at impact surface.

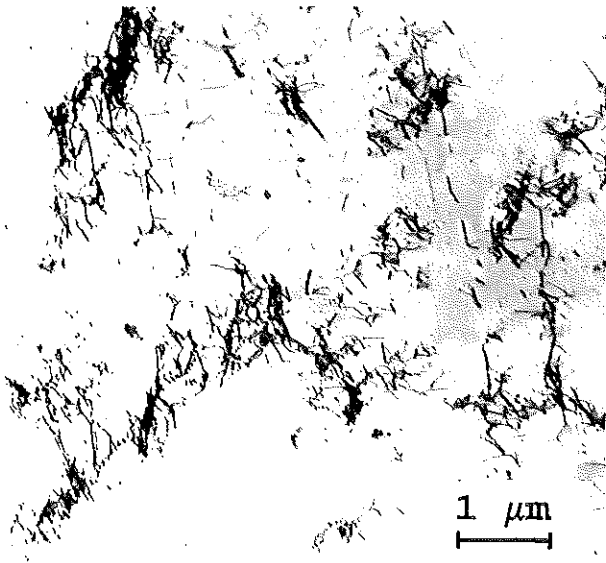


Figure 6: Cu single crystal. The structure near free end.

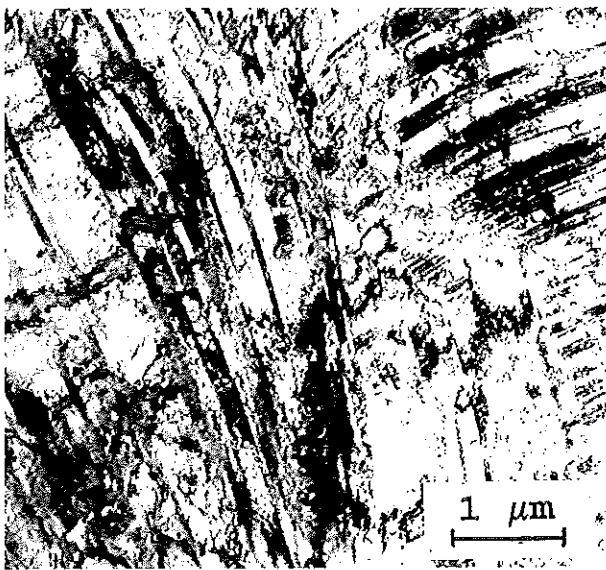


Figure 7: Aluminium bronze (Cu3Al). The structure near impact surface.

4 CONCLUSION

The formation of dislocation cell structure (in copper) or high dislocation density (in low SFE, planar slip alloys) is the evidence of plastic deformation extending through whole specimen's volume. This makes one assumption (the existence of deformed and undeformed portions of loaded specimens), on which the evaluation of Taylor test is based, doubtful.

The existence of breaks in the profile (and hardness) monotonic course is in our opinion, result of the interaction between plastic (compressive) wave propagating toward the free end of specimen and reflected elastic (tensile) stress wave(s). This effect may be used to measure c_p (plastic wave propagation rate) directly.

The decrease of diameter near the free end is apparently due to the mechanism that (at higher loading intensity or more favorable geometry) normally leads to the spall formation.

5 NOMENCLATURE

v_0 = impact velocity, m/s, X = distance, mm, UTS = ultimate tensile strength, Mpa, SFE = stacking fault energy, J/m^2 , c_p = plastic wave propagation rate, m/s.

6 REFERENCE

JONES S.E., GILLES P.P., FOSTER J.C., WILSON L.L. 1990 - *A one-dimensional, two-phase model for Taylor impact specimen*. J. Engng. Technol. Vol. 17; pp 17-29.

EFFECT OF GRAIN SIZE AND STRAIN RATE ON THE TENSILE WORK-HARDENING OF OFHC COPPER

J. P. Noble and J. Harding
Department of Engineering Science, University of Oxford
Parks Road, Oxford OX1 - 3PJ, U.K.

ABSTRACT

Standard cylindrical tensile specimens were prepared from blocks of OFHC copper which had been cold-rolled and annealed to give a range of grain sizes from $15\mu\text{m}$ to $250\mu\text{m}$. Tensile stress-strain curves have been obtained from tests on these specimens at strain rates from quasi-static to $\sim 3000/\text{s}$. Between the quasi-static and the intermediate rates the usual small increase in flow stress with strain rate is observed and there is a continuous decrease in the rate of work-hardening with increasing plastic strain. In contrast, at impact rates of strain a much lower initial work-hardening rate is obtained, leading to flow stresses significantly below those at the same strain in tests at the lower rates of strain. Subsequently, at strains of between 10% and 25%, the work-hardening rate rapidly increases and flow stresses much closer to those at the intermediate rate of straining are obtained. This anomalous behaviour was shown in tests on all grades of copper but was most marked in specimens having the largest grain size.

INTRODUCTION

Although the effect of strain rate on the mechanical behaviour of high-purity copper has been studied by many different investigators, in most cases either a uniaxial compressive loading system [LINDHOLM, 1964] has been used or one involving torsion of a thin-walled tubular specimen [TSAO, 1973]. The type of behaviour normally observed is shown schematically in the stress-strain curves of fig. 1. Although much less work has been done under high rate tensile loading, in an early study, using an electromagnetic pulse loading technique [HARDING, 1971] which produces a strain of $\sim 5\%$ at a mean rate of $\sim 1000/\text{s}$, a very different initial work-hardening behaviour was observed with a small drop in stress at first yield followed by a constant stress plateau,

as shown in Fig. 2. Similar behaviour was also seen [DORMEVAL, 1979] using cylindrical specimens with a gauge length of 30mm, rather longer than is commonly used in Hopkinson-bar impact tests.

More recently the high-rate behaviour of copper in tension has been studied by [GOURDIN, 1991], who used the expanding ring technique, and [PARRY, 1989], who used the split-collar method. In neither case was this anomalous initial work-hardening behaviour reported. It is well known, however, that the expanding ring technique does not allow an accurate determination of the stress-strain response at strains less than $\sim 15\%$ while, because there is a limit on the maximum strain rate that can be reached using the split-collar method, at the highest strain rates only stress-strain curves obtained under compressive loading were presented. This limitation does not apply to the standard version of tensile Hopkinson-bar apparatus [HARDING, 1960] which, in a slightly modified form [NOBLE, 1991], was used in a recent study of the effect of strain rate on the stress-strain behaviour of an annealed OFHC copper. It is significant, therefore, that in these tests the anomalous initial work-hardening behaviour was very clearly apparent. Further confirmation of this effect has also been reported recently [LASSILA, 1992] for tests on a very similar tensile Hopkinson-bar system but on strip, rather than cylindrical, test specimens. In this case the anomalous behaviour was less marked and, it was suggested, arose from errors in the transmitted stress wave due to reflections in the geometrically complex fixtures used to grip the strip specimens. Both [GOURDIN, 1991] and [PARRY, 1989] also studied the effect of grain size on the flow stress of copper at high rates of strain.

In the present investigation standard cylindrical tensile

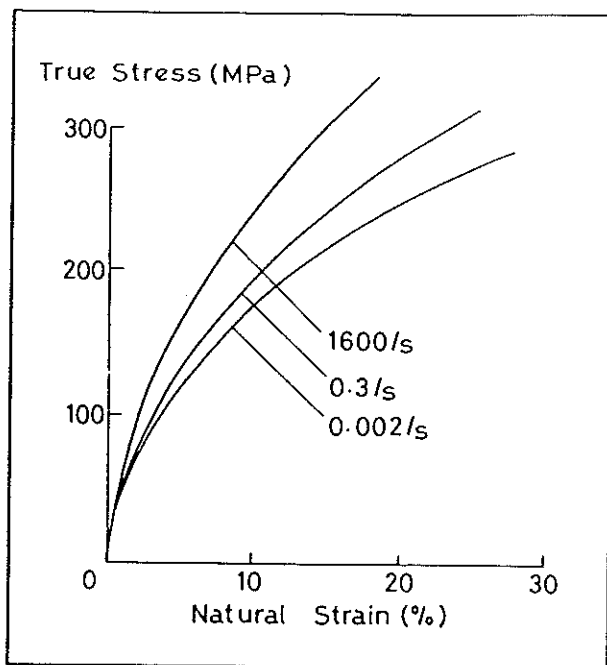


Fig. 1 Effect of Strain Rate on High-Purity Copper in Compression (schematic)

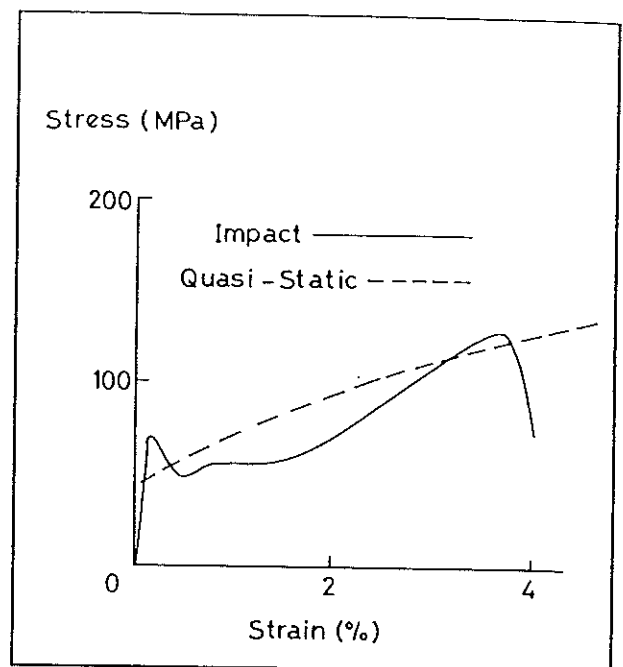


Fig. 2 Effect of Strain Rate on High-Purity Copper in Tension [Harding 1971]

specimens have been prepared from blocks of OFHC copper which had been cold-rolled and annealed to give a range of grain sizes from $15\mu\text{m}$ to $250\mu\text{m}$. Tensile stress-strain curves have been obtained from tests at strain rates from quasi-static to $\sim 3000/\text{s}$. The anomalous initial work-hardening behaviour is confirmed in all tests at the impact rate and found to be the more marked the coarser the grain size of the test specimen. The effect of this behaviour on the grain-size dependence of the flow stress under impact loading is investigated.

EXPERIMENTAL DETAILS

Specimen Materials

Standard cylindrical test specimens, having a gauge diameter of 3.175mm and a nominal gauge length of 8.89mm were machined from blocks of OFHC copper which had been cold-rolled to a reduction of 66% and subsequently annealed for 2 hours at temperatures of 800°C , 600°C and 400°C to give a uniform grain structure with mean grain diameters, measured by the ASTM mean linear intercept method, of $250\mu\text{m}$, $40\mu\text{m}$ and $18\mu\text{m}$ respectively. Specimens were machined after heat treatment of the blocks. In view of the anomalous work-hardening behaviour observed in impact tests on specimens from all three of these blocks a fourth block of even finer grain size material, with a mean grain diameter of $15\mu\text{m}$, was subsequently prepared under carefully controlled conditions.

Experimental Programme

Tests were performed at tensile strain rates from $\sim 0.01/\text{s}$ to $\sim 3000/\text{s}$. A standard screw-driven Instron testing machine was used at quasi-static rates up to $\sim 0.01/\text{s}$, a hydraulically-operated rapid loading machine

at intermediate rates between 0.2 and $100/\text{s}$ and a tensile Hopkinson-bar apparatus at impact rates between 1000 and $3560/\text{s}$. During some of the impact tests high-speed photographs showing the overall elongation of the tensile specimen at $10\mu\text{s}$ intervals during the course of the test were taken using a Cordin framing camera.

RESULTS

Stress-Strain Curves

Tests have been performed for at least one quasi-static, one intermediate and one impact rate on specimens of each of the four grain sizes. Mean engineering stress-engineering strain curves for several tests at each rate on specimens annealed at 800°C (mean grain diameter $250\mu\text{m}$) and 400°C (mean grain diameter $18\mu\text{m}$) are presented in figs. 3 and 4, respectively. In each case the general shape of the stress-strain curves at the quasi-static and intermediate rates follows the expected behaviour and the effect of strain rate is consistent with that usually observed in torsion or compression tests. In contrast, at impact rates and for tests on specimens of both coarse and fine grain size a very different initial work-hardening behaviour is obtained. The effect is most marked for the coarse grained material, fig. 3, where in the impact tests there appears to be no raising of the stress at the start of plastic flow and where the flow stress lies below that for the quasi-static tests at plastic strains $< \sim 15\%$ and below that for the intermediate rate tests at plastic strains $< \sim 20\%$. Immediately following the start of plastic flow the work-hardening rate is very much lower than in the tests at the lower strain rates. It then rapidly increases until the flow stress lies above that for the lower rate tests. For the impact tests in Fig. 3 the limitations of the Hopkinson-bar apparatus made it impossible to con-

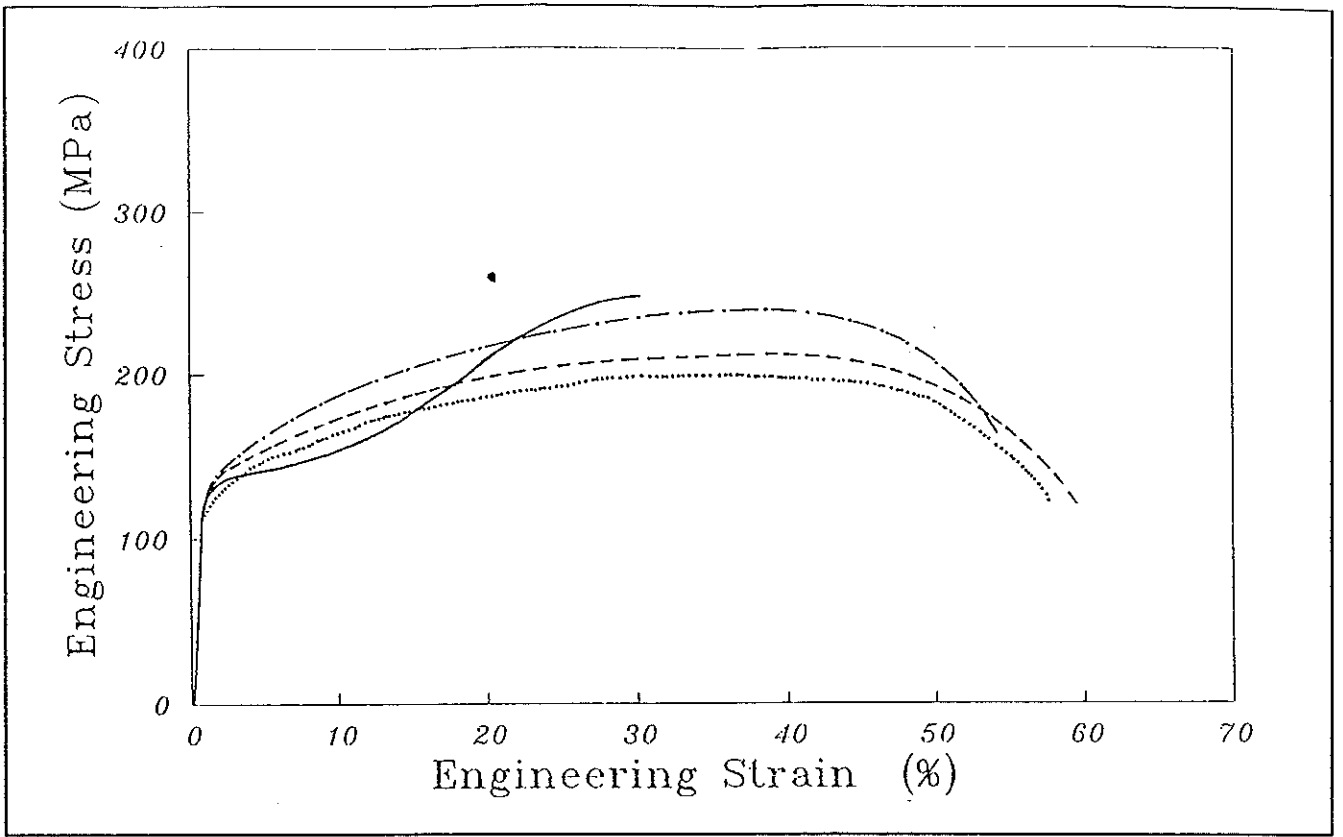


Fig. 3 Engineering Stress-Strain Curves for Copper Annealed at 800°C
 (Average strain rate: 0.01/s; ----- 0.27/s; - · - · - 71/s; ——— 3700/s)

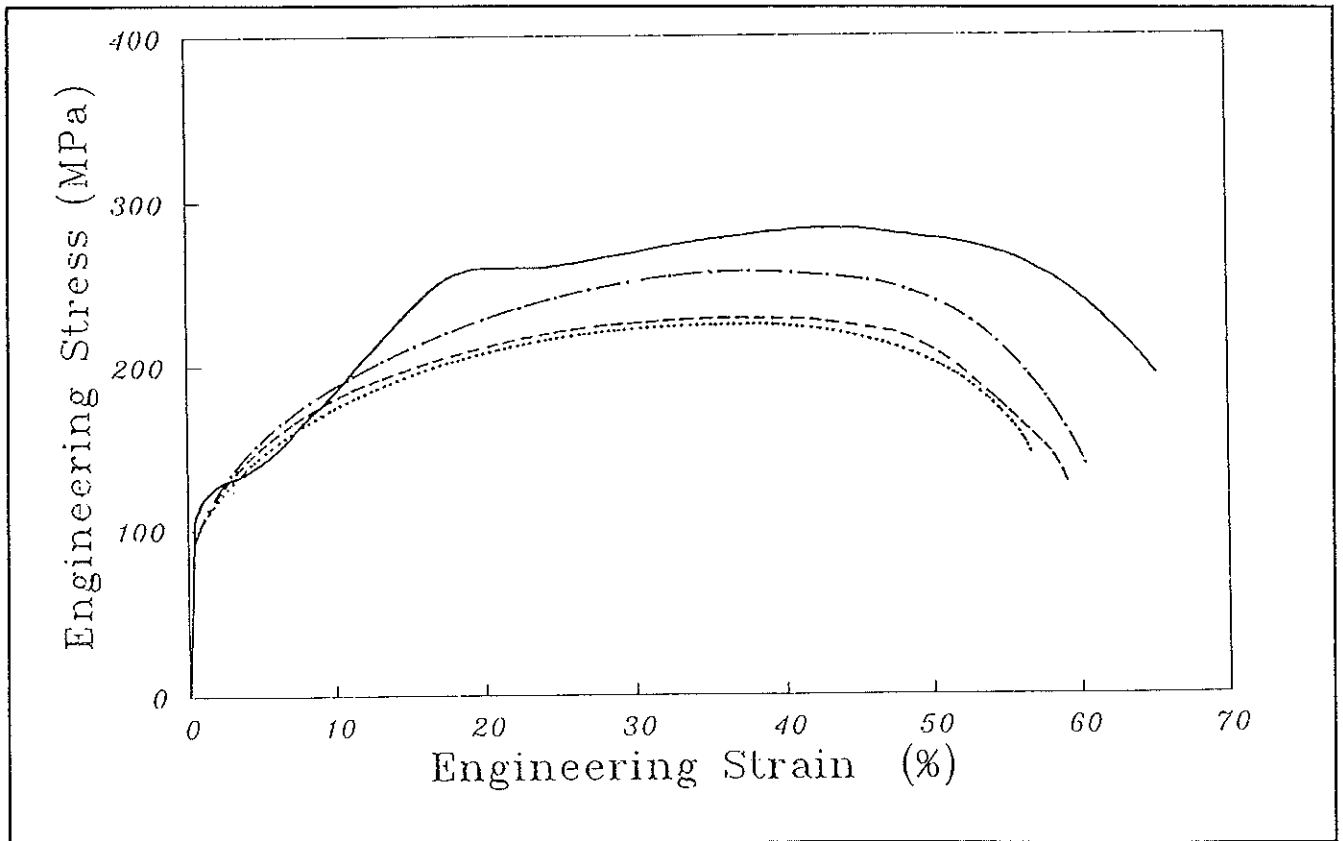


Fig. 4 Engineering Stress-Strain Curves for Copper Annealed at 400°C
 (Average strain rate: 0.002/s; ----- 0.009/s; - · - · - 80/s; ——— 2000/s)

tinue the analysis to strains > about 35%.

These limitations were overcome before the impact tests of fig. 4 were performed so that in this case stress-strain curves at the impact rate could be derived up to strains of about 50%. While the same general stress-strain behaviour is seen in the fine-grained material of fig. 4 as in the coarse-grained material of fig. 3, the range of strains over which the flow stress at the impact rate lies below that at the intermediate or lower rates is reduced to about the first 10% and a small increase in the stress at the start of yielding in the impact tests is also apparent.

An indication of the reliability with which the flow stresses may be determined in the impact tests is given in fig. 5 which shows true stress-natural strain curves for six nominally identical impact tests on specimens having a mean grain diameter of $\sim 40\mu\text{m}$. It is clear that there is a scatter of about $\pm 10\%$ in the measured flow stresses during the early stages of deformation, rather more than the magnitude of the strain rate effect observed at these strains in the stress-strain curves of fig. 4. Nevertheless the anomalous work-hardening behaviour in this region is well-established and clearly seen in all six tests.

High-Speed Photographs

High-speed photographs were obtained in several of the impact tests. A selection of frames taken from the set of photographs for a test on a specimen of $40\mu\text{m}$ mean grain diameter is shown in fig. 6. In any one test a total of 500 frames is obtained, the time interval between each frame being $10\mu\text{s}$. The specimen behaviour, therefore, is recorded over a period of 5ms, well in excess of the time, $\sim 700\mu\text{s}$, required to fracture specimens of this material under impact loading. Only one frame in eight is shown in fig. 6. The first of these (frame 2) shows the undeformed specimen just before the loading wave arrives and the last (frame 74) shows the specimen after fracture.

The variation of the specimen engineering strain with time, calculated from the overall elongation of the specimen as determined from the high-speed photographs, is compared in fig. 7 with that obtained from the standard Hopkinson-bar wave analysis for an identical test on a similar specimen. By adjusting the relative positions of the two curves such that the start of the Hopkinson-bar strain-time curve coincides with frame 2 in fig. 6, very close agreement between the two estimates of strain is obtained over the first $200\mu\text{s}$ of the test. At times greater than $200\mu\text{s}$ from the start of deformation the general shape of the two strain-time curves remains similar but the Hopkinson-bar analysis gives a slightly higher estimate of the strain at any given instant. This is not surprising since waves reflecting from the ends of the projectile and the loading bars lead, in this region, to a marked reduction in the overall strain rate and make the Hopkinson-bar analysis much less accurate. The comparison in fig. 7 is limited to a time of just under $600\mu\text{s}$ from the start of loading, the maximum period over which the Hopkinson-bar analysis

could be performed. While the specimen has not reached fracture in this time it is well beyond the region over which the anomalous work-hardening behaviour is observed in the impact tests.

Grain-Size Dependence

The true flow stress at plastic strains of 5%, 15% and 25%, i.e. at strains both within and beyond the range over which the anomalous work-hardening behaviour was observed, were determined from tests on each material at three nominal strain rates, a quasi-static rate of $\sim 0.01/\text{s}$, an intermediate rate of $\sim 80/\text{s}$ and an impact rate of $\sim 3000/\text{s}$. The variation of the flow stress with the inverse square root of the grain diameter is shown in fig. 8, for tests at the quasi-static rate, and in fig. 9, for tests at the impact rate. All the measured flow stress values are plotted. For clarity of presentation some of the data in fig. 9 for tests on specimens having mean grain diameters of $250\mu\text{m}$ and $40\mu\text{m}$ (corresponding to $(d)^{-1/2}$ values of 2 and 5) have been offset from their correct positions.

In the quasi-static tests, the experimental scatter is seen to be less than $\pm 5\%$ (except for specimens of mean grain diameter $18\mu\text{m}$ where the scatter was about $\pm 10\%$). A linear dependence of flow stress on the inverse square root of the grain diameter, as predicted by the Hall-Petch relationship,

$$\sigma_{\text{fl}} = \sigma_i + k/\sqrt{d}$$

where σ_i is the friction stress and k is the grain boundary stress concentration term, is commonly observed [PARRY, 1989; GOURDIN, 1991]. The present results at both 15% and 25% plastic strain may be fitted to this relationship (although at 15% plastic strain the flow stress for the specimens having a mean grain diameter of $40\mu\text{m}$ lies slightly above the straight-line plot). The corresponding values for the friction stress are $\sim 200\text{MPa}$ and $\sim 250\text{MPa}$ at 15% and 25% plastic strain respectively while k appears to be relatively independent of plastic strain and to have a value of $\sim 8\text{Nmm}^{-3/2}$. This is not the case at 5% plastic strain where, if the results are to be fitted to a straight-line plot, k falls to $\sim 3.2\text{Nmm}^{-3/2}$ and the corresponding value of the friction stress is $\sim 160\text{MPa}$. Here, however, the results for specimens having a mean grain diameter of $40\mu\text{m}$ fall well above the linear plot.

In the impact tests the experimental scatter was greatest, about $\pm 20\%$, in the tests on specimens of the two coarser grain sizes, i.e. those with mean grain diameters of 250 and $40\mu\text{m}$. Nine impact tests were performed on specimens of the coarsest grain size. Some of the experimental scatter in these tests is probably due to specimens having been taken from different regions of the original cold-rolled and annealed block. Also some specimens were cut with their axes parallel to and others with their axes perpendicular to the rolling direction. This appeared to have a bigger effect on the mechanical behaviour under impact loading than at lower rates [RUIZ, 1991]. There were twenty-

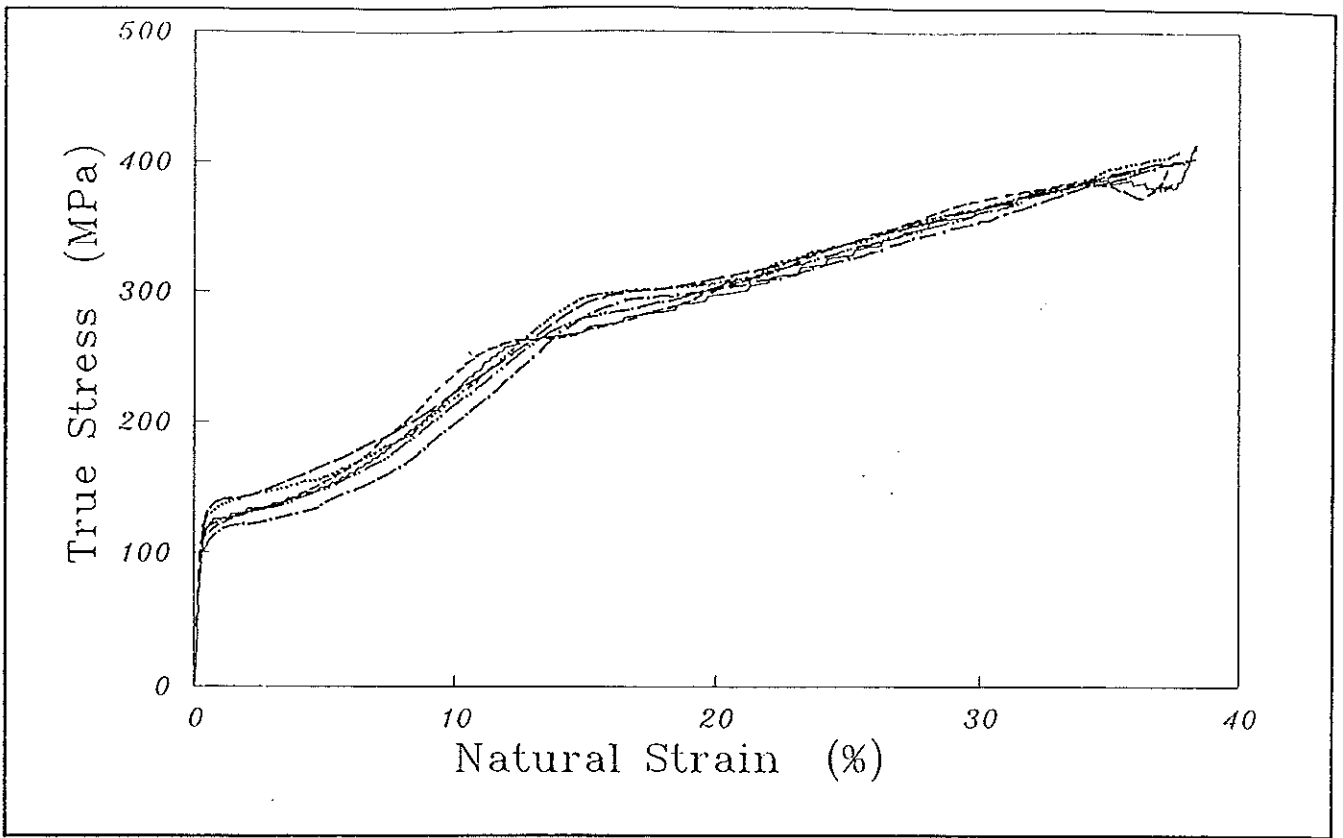


Fig. 5 Stress-Strain Curves for Six Impact Tests on Specimens of Copper Annealed at 600°C
(Average strain rate:- 2790/s)

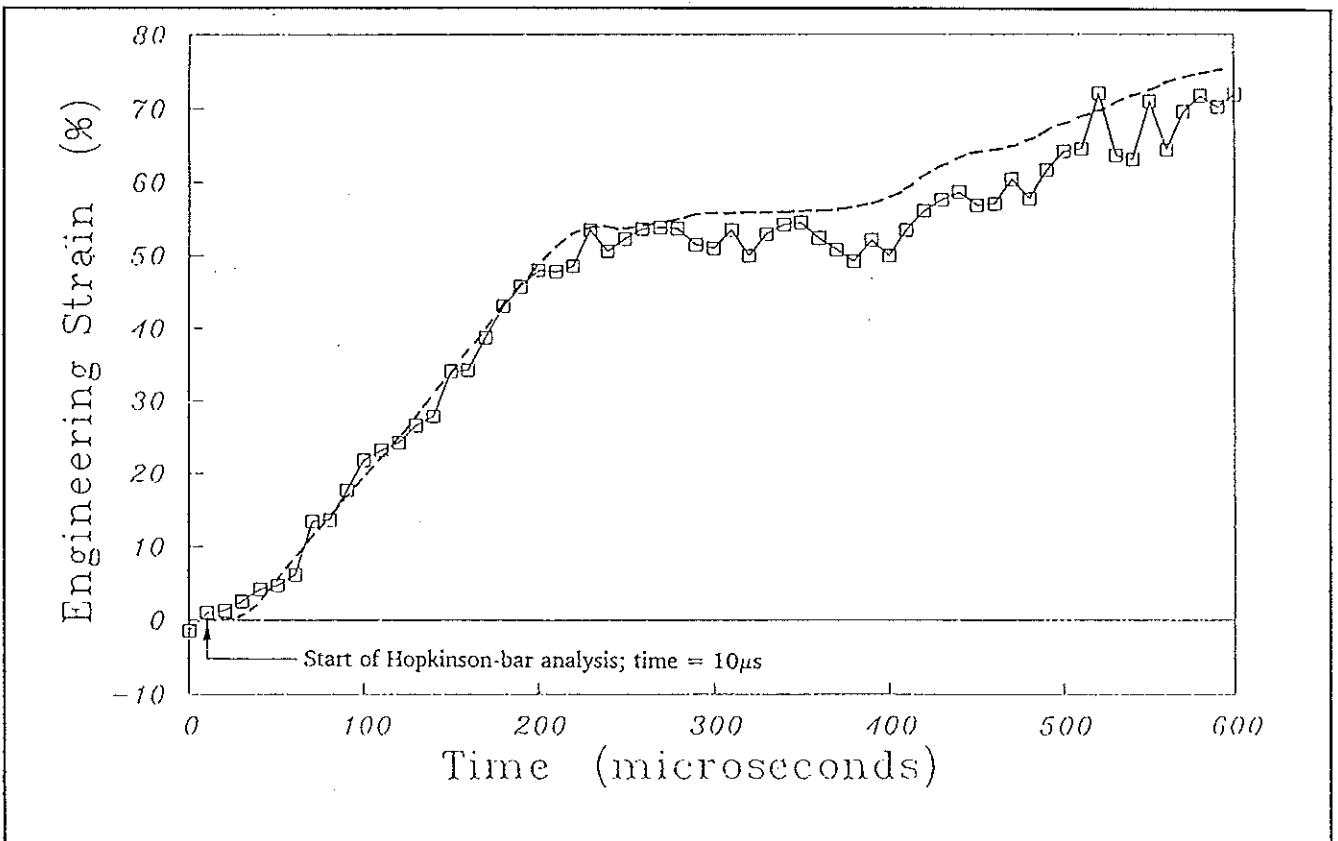
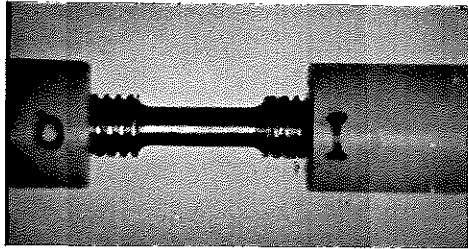
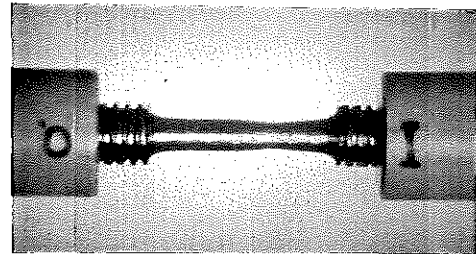


Fig. 7 Variation of Specimen Strain with Time for Impact Test on Specimen of Mean Grain Diameter 40µm
(Comparison between strains determined from Hopkinson-bar analysis and those determined using Cordin high-speed camera)

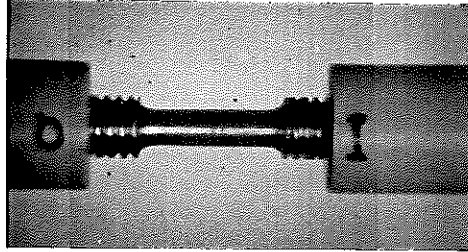
[Hopkinson-bar analysis: - - - - - ; High-speed photographs: —□— ;]



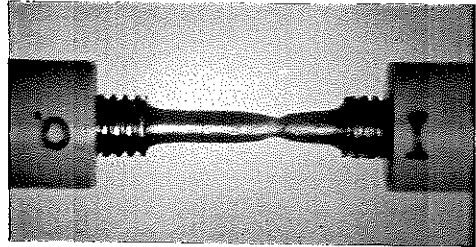
Frame 2



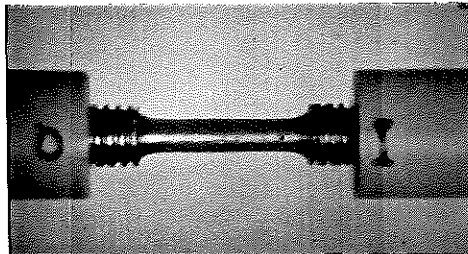
Frame 42



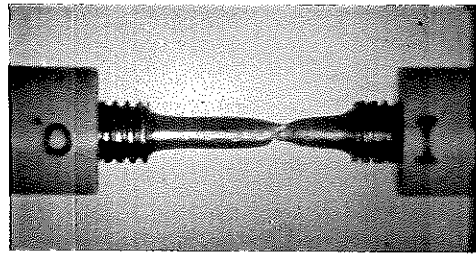
Frame 10



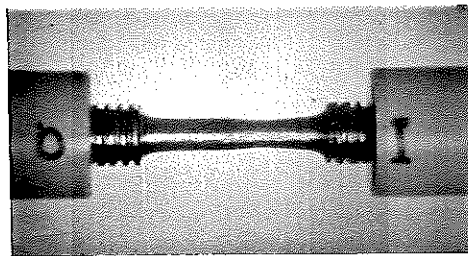
Frame 50



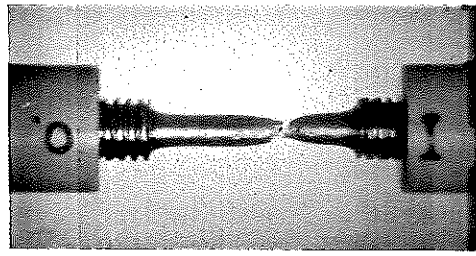
Frame 18



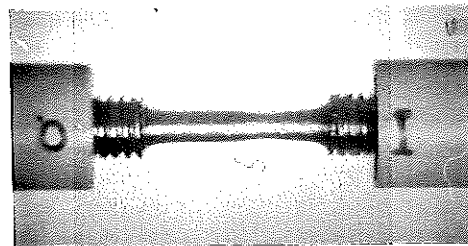
Frame 58



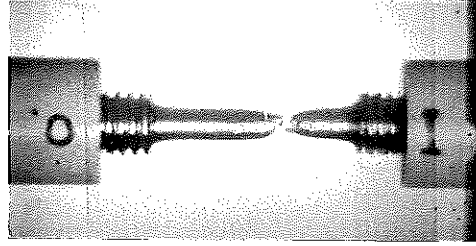
Frame 26



Frame 66



Frame 34



Frame 74

Fig. 6 High-Speed Photographs for Impact Test on Specimen of Mean Grain Diameter $40\mu\text{m}$
(Photographs at $80\mu\text{s}$ intervals)

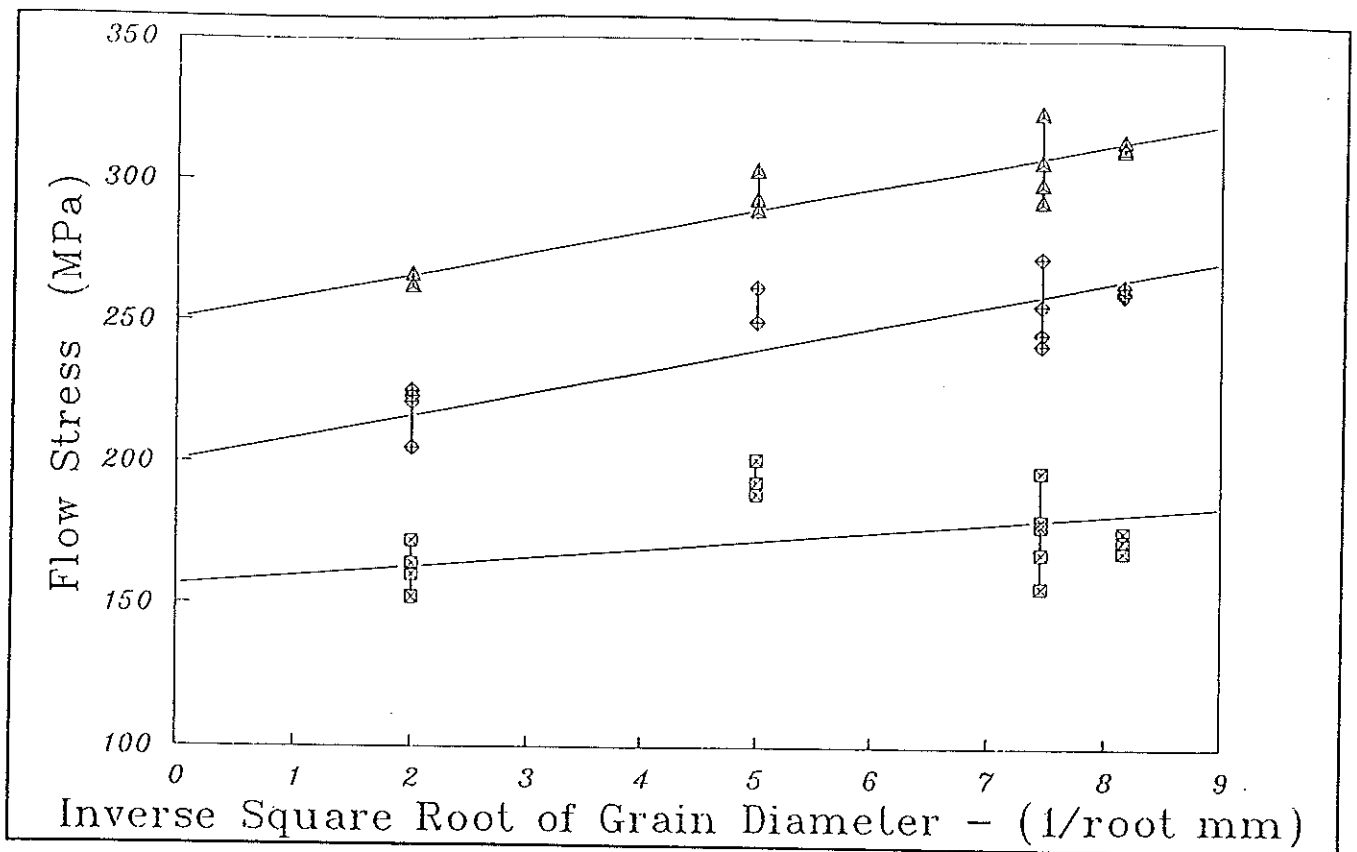


Fig. 8 Variation of Flow Stress with Inverse Square Root of Grain Diameter in Quasi-Static Tests (Flow stresses at plastic strains of: 5% —□— ; 15% —◇— ; 25% —△— ;)

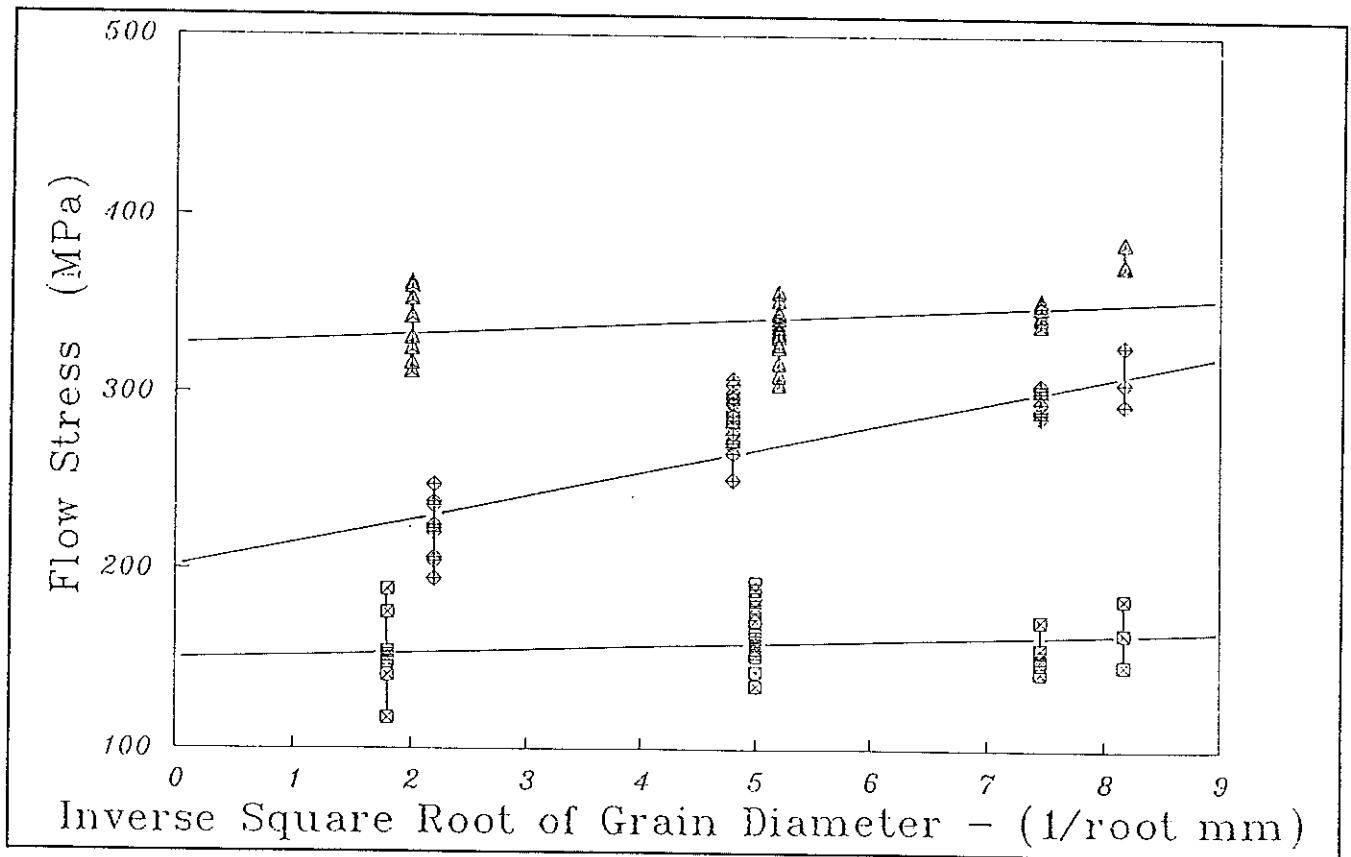


Fig. 9 Variation of Flow Stress with Inverse Square Root of Grain Diameter in Impact Tests (Flow stresses at plastic strains of: 5% —□— ; 15% —◇— ; 25% —△— ;)

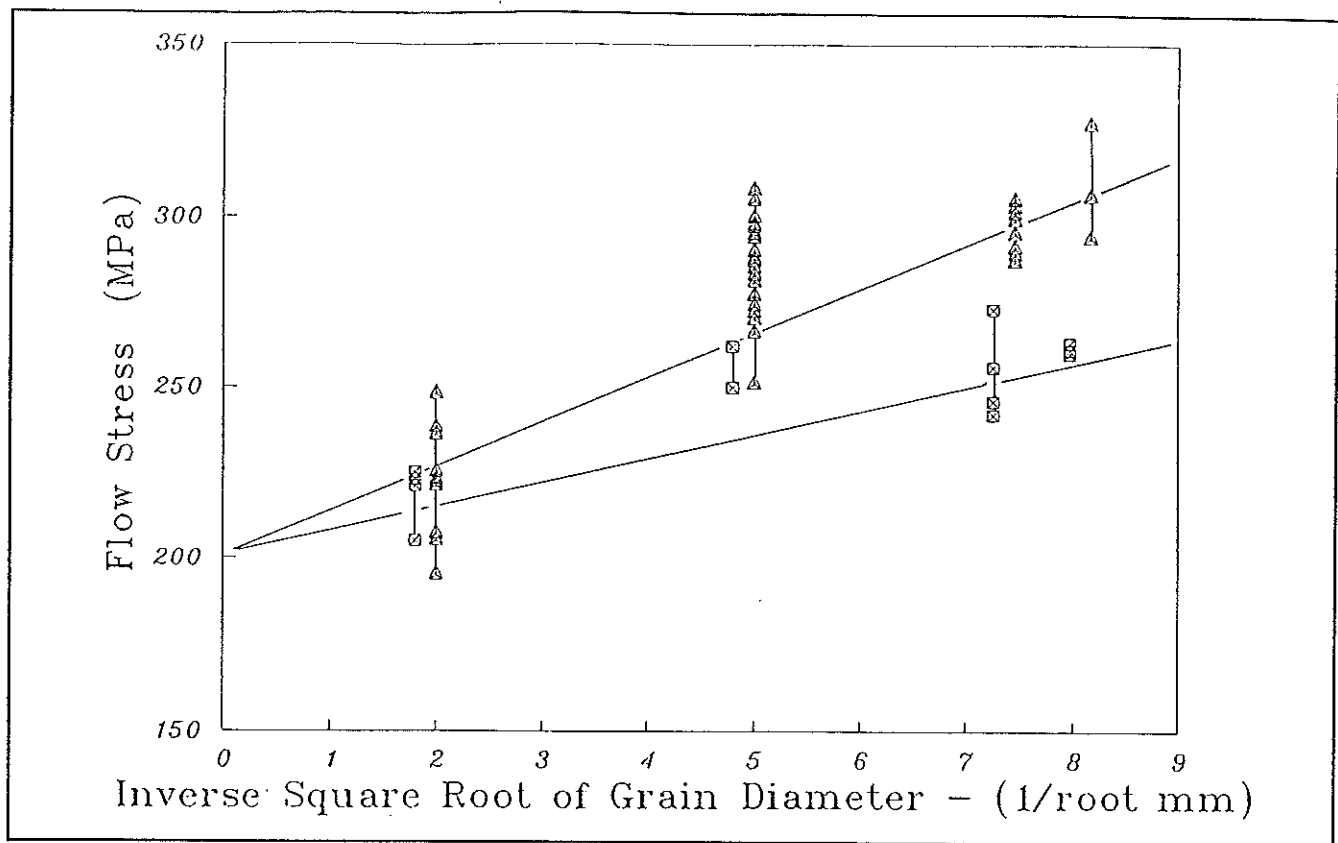


Fig. 10 Effect of Strain Rate on the Grain-Size Dependence of the Flow Stress at 15% Plastic Strain (Quasi-static tests: \square ; Impact tests: \triangle ;)

factor k at different plastic strains. Thus, while at 15% plastic strain k increases quite markedly with strain rate, see fig. 10, at both 5% and 25% plastic strain a significant decrease in k is apparent with increasing strain rate. This is in marked contrast to the results of [GOURDIN, 1991] who found k to have a constant value of $\sim 8.8 \text{Nmm}^{-3/2}$ over a wide range of both strain rate and plastic strain. It should be noted, however, that the maximum strain rate in these tests, i.e. the maximum strain rate at which Gourdin et al. established a rate-independence for k , was only $\sim 100/\text{s}$. This is an order of magnitude below that at which anomalous effects were observed in the present tests. Since, at 15% plastic strain, impact tests on the coarse-grained specimens ($d^{-1/2} = 2$) show the biggest reduction in flow stress over that for quasi-static tests (see fig. 3) whereas in tests on fine-grained specimens ($d^{-1/2} = 7.5$) this reduction no longer exists (see fig. 4), the much higher value of k at 15% plastic strain for the impact tests is clearly a direct result of the anomalous work-hardening behaviour.

At 5% plastic strain the reduction in flow stress associated with the anomalous work-hardening behaviour is similar in both coarse and fine-grained specimens while at 25% plastic strain we are beyond the region within which the anomalous behaviour is observed for specimens of all grain sizes. It is, perhaps, more significant, therefore, that at these plastic strains k is found to decrease with increasing strain rate. Thus while in the quasi-static tests the present results show some agreement with those of Gourdin and Lassila in

that here also a similar value for k , $\sim 8 \text{Nmm}^{-3/2}$, is obtained at plastic strains of both 15% and 25%, at impact rates of $\sim 2000/\text{s}$, well above the maximum at which Gourdin and Lassila measured k , the present results, at a plastic strain of 25% where the anomalous work hardening behaviour is no longer observed, show a reduction in k to $\sim 3 \text{Nmm}^{-3/2}$.

CONCLUSIONS

The anomalous work-hardening behaviour at plastic strains up to $\sim 20\%$ in high-purity copper under tensile impact loading has been observed in all such tests (a total of 42 tests) on specimens of four different grain sizes from $250 \mu\text{m}$ to $15 \mu\text{m}$. The effect is more marked in the coarser grain-sized specimens. A tentative explanation for this behaviour has been proposed in terms of a predisposition to localised yielding in copper at the highest rates of strain as a result of a state of quasi-static equilibrium not having been attained in the specimen gauge section by the start of the yielding process.

At both quasi-static and impact rates of strain the present results show an approximately linear dependence of the flow stress on the inverse square root of the grain diameter, as predicted by the Hall-Petch relationship. At both rates of strain the friction stress, σ_f , increases with plastic strain. In the quasi-static tests a grain-boundary

stress concentration factor, k , at 5% plastic strain of $\sim 3.2 \text{Nmm}^{-3/2}$ is obtained, rather lower than that reported elsewhere [GOURDIN, 1991]. At plastic strains of 15% and 25%, however, a constant value for k of $\sim 8 \text{Nmm}^{-3/2}$ is found, in much closer agreement with the earlier work. As a direct consequence of the anomalous work-hardening behaviour observed in the impact tests, no increase is found in the friction stress under impact loading at either 5% or 15% plastic strain. There is, however, the expected increase in friction stress with strain rate at 25% plastic strain, this being outside the region in which the anomalous behaviour was observed.

Similarly the measured values for k in the impact tests, $\sim 1.9 \text{Nmm}^{-3/2}$ at 5% plastic strain and $\sim 13.9 \text{Nmm}^{-3/2}$ at 15% plastic strain, are strongly affected by the anomalous work-hardening behaviour observed at this strain rate. Only at 25% plastic strain, where this is not the case, may a direct comparison be made with the quasi-static tests. In contrast with Gourdin and Lassila, who found a constant value of k at rates up to 100/s, the present results show a reduction in k from $\sim 8 \text{Nmm}^{-3/2}$ at the lower rate to $\sim 3 \text{Nmm}^{-3/2}$ at a rate of $\sim 2000/\text{s}$.

REFERENCES

DORMEVAL R., STELLY M. 1979 - *Influence of Grain Size and Strain Rate on the Mechanical Behaviour of High-Purity Polycrystalline Copper* - Institute of Physics Conf. Ser. No. 47 (Inst. of Physics, London and Bristol) pp. 154-165.

GOURDIN W.H., LASSILA D.H., 1991 - *The Flow Stress of OFE Copper at Strain Rates from 10^3 - 10^4 s^{-1} : Grain-Size Effects and Comparison to the Mechanical Threshold Stress Model* - Acta metall. mater. Vol. 39; pp. 2337-2348

HARDING J., WOOD E.O., CAMPBELL J.D., 1960 - *Tensile Testing of Materials at Impact Rates of Strain* - J. Mech. Eng'g. Sci., Vol. 2; pp. 88-96.

HARDING J. 1971 - *The Yield Behaviour of Pure Polycrystalline Copper under Repeated Tensile Impact Loading* - Acta Met. Vol. 19; pp. 1177-1188.

HARDING J., NOBLE J.P., 1993 - *Effect of Strain Rate on the Mechanical Properties of C103 OFHC Copper Annealed at 600°C* - Oxford University Engineering Department, Solid Mechanics Group Report No. JH/026/93.

LASSILA D.H. 1992 - (private communication)

LINDHOLM U. S. 1964 - *Some Experiments with the Split Hopkinson Pressure Bar* - J. Mech. Phys. Solids, Vol. 12: pp. 317-335.

NOBLE J.P., HARDING J., 1991 - *Effect of Strain Rate on the Mechanical Properties of Annealed OFHC Copper* - Oxford University Engineering Department, Solid Mechanics Group Report No. JH/008/91.

PARRY D.J., WALKER A.G., 1989 - *Effects of Grain Size and Temperature on the Mechanical Properties of OFHC Copper* - Institute of Physics Conf. Ser. No. 102 (Inst. of Physics, London and Bristol); pp.329-336.

RUIZ D.J., NOBLE J.P., HARDING J., 1991 - *Effect of Strain Rate on the Mechanical Properties of Annealed OFHC Copper* - Oxford University Engineering Dept., Solid Mechanics Group Report No. JH/005/91.

BEHAVIOUR OF Al 7017 T73 AT HIGH STRAIN RATES AND TEMPERATURE

J. Rodríguez, V. Sánchez-Gálvez
Department of Materials Science, Polytechnic University of Madrid, E.T.S.I. Caminos,
Ciudad Universitaria s/n , 28040 Madrid, Spain.

C. Navarro
Department of Engineering, Carlos III University, Avda. del Mediterráneo 20,
28913 Leganés, Madrid, Spain.

ABSTRACT

Temperature and strain rate provide a key link between microscopic aspects of plastic flow and macroscopic mechanical properties. In order to investigate the influence of both magnitudes on the behaviour of the aluminium alloy 7017 T73, several tensile tests have been carried out at different conditions of temperature and strain rate. For the quasi-static tests a conventional testing machine has been used, while the dynamic response has been determined employing a tensile version of the Hopkinson bar. At room temperature (25 °C) the material shows low strain rate sensitivity. As the temperature increases, this alloy suffers a continuous softening process although the influence of strain rate is kept low up to temperatures around 150 °C. However, the situation is notably different when the temperature reaches 300 °C, because the quasi-static properties are clearly lower than those of the dynamic values. Additionally, a study of the fracture surface has been undertaken by means of scanning electron microscopy, to identify the main mechanisms causing material failure.

INTRODUCTION.

The determination of stress-strain curves for different conditions of strain rate and temperature provides a direct means to establish relationships between macroscopic properties and microscopic mechanisms of plastic flow [Campbell, 1973]. The influence of these magnitudes in the mechanical properties of metallic materials has been widely studied in a separate manner. However, there are not many works considering the coupled effects of both variables [Steinberg,1980].

The 7XXX aluminium alloys (Al-Zn-Mg) are very useful materials in diverse industrial applications, due to their relatively high strength and low density. Aeronautic components and lightweight armours are examples of

these application possibilities in two fields where the strain rate response is a very significant variable. Generally, it is recognized that in metallic materials the yield strength shows a linear dependency with the logarithm of the strain rate [Zukas,1982]. This type of dependency indicates thermally activated mechanisms associated with plastic flow [Harding,1989]. These processes are controlled by equations of the following type:

$$\dot{\epsilon}_p = \dot{\epsilon}_0 \exp(-\Delta G/kT)$$

where $\dot{\epsilon}_p$ represents the plastic strain rate, T temperature, k the Boltzmann constant, $\dot{\epsilon}_0$ a material constant and ΔG is the free energy activation term. The ΔG form depends on the barrier impeding the flow, but generally, it is a function of the stress σ . This formulation leads to a linear dependency of the yield strength with the logarithm of the strain rate

It is also very well known that for aluminium alloys the rate sensitivity decreases when the alloy strength increases, because the athermal component of yield strength is more important [Burstow,1988]. In the particular case of the alloys belonging the 7XXX serie (Al-Zn-Mg) this dependency of the yield strength with the strain rate is very low, if any.

The Al 7017 T73 alloy, subject of this study, is a precipitation hardened material with the following composition: Zn 5.1%, Mg 2.4%, Fe 0.3%, Si 0.16%, Cu 0.12%, Mn 0.22%, Cr 0.16%, Zr 0.12%, Al bal. The heat treatment T73 is an overaging to improve the corrosion resistance and it is constituted by several steps: 1 hour at 430 °C + cold water + 2 days at room temperature + 8 hours at 150 °C (heating rate 20 °C/h). The manufacturing process is rolling and the final microstructure consists of very long grains with significant differences between longitudinal dimensions

(around 1 mm) and transverse dimensions(around 10 μm). The precipitates are semicoherent and incoherent with the matrix and there are also some Fe inclusions of several micrometers in size [Mondolfo, 1971 and Polmear,1981].

In this work, the influence of strain rate in the mechanical properties of this alloy is studied with the aim to determine if the low rate sensitivity shown at room conditions is also confirmed at higher temperatures. To this end, several tension tests have been carried out at different values of strain rate in the range $(10^{-4} - 10^3) \text{ s}^{-1}$ and changing the temperature from 25 $^{\circ}\text{C}$ to 300 $^{\circ}\text{C}$. Additionally, the fracture surface of the specimens has been analyzed to identify the rupture mechanisms acting in each condition.

EXPERIMENTAL PROGRAMME.

The quasi-static tests were carried out in a conventional testing machine at two different strain rates: 10^{-4} and 10^{-2} s^{-1} . For the dynamic conditions (10^3 s^{-1}) a tensile version of the Hopkinson bar was used. This experimental technique is very well known and is not detailed here [Davies, 1963; Harding, 1960; Elwood, 1982 and Rodríguez, 1993]. Basically, the ends of a rounded tensile specimen is threaded to two high strength steel bars. A tensile pulse is generated in the first bar by means of the impact of a tubular projectile, and it is partially transmitted to the second bar through the specimen. The bars behave elastically during the test and they are instrumented with strain gauges at different positions along them. The stress in the specimen is calculated as the force transmitted through the specimen divided by the specimen section. The apparent average strain is obtained as the relative displacement between the bars divided by the gage length. In all conditions the specimens had the same geometry (figure 1).

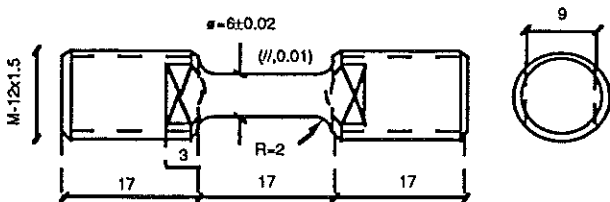


Figure 1. Tensile specimens geometry.

In the high temperature test, the specimens were placed in an electric resistance furnace. The specimen temperature was measured with chromel-alumel thermocouples (accuracy $\pm 1\%$), and the heating rate was approximately 12 $^{\circ}\text{C}$ per minute. Therefore the heating process last about 25 minutes This equipment is depicted in the figure 2.

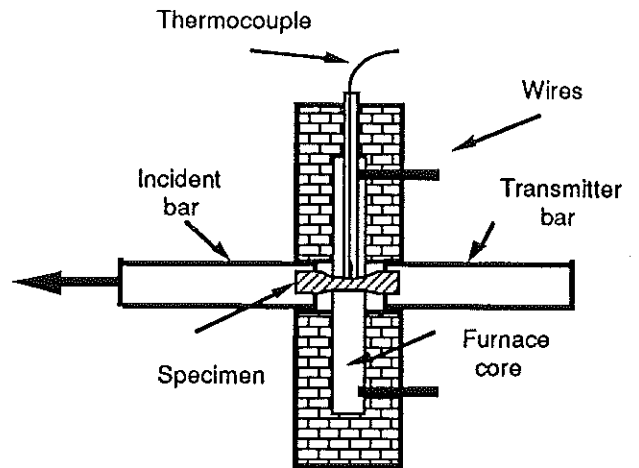


Figure 2. Electric resistance furnace.

RESULTS AND FRACTOGRAPHY.

The results obtained from the experimental programme are summarized in the figures 3 to 5, where stress-strain curves are represented for each condition. As it can be seen, the behaviour is almost rate independent at room temperature and this behaviour remains unchanged up to 150 $^{\circ}\text{C}$, the artificial overaging temperature. For higher temperatures the material experiences an increasing softening process and the strain rate sensitivity is higher from this point, as it is usual in soft aluminium. The influence of temperature in the yield strength and the tensile strength is shown in the figures 6 and 7 , and the comparison of this behaviour with another aluminium alloys at high strain rates (Al 6061 T6 [Rosenberg,1986] and 7075 T73 [Burstow,1988]) is illustrated in figure 8, showing similar results.

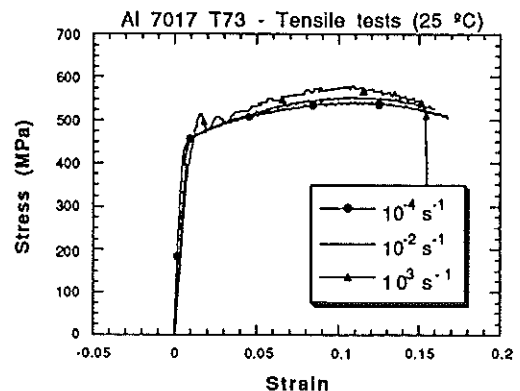


Figure 3. Stress-strain curves at room temperature.

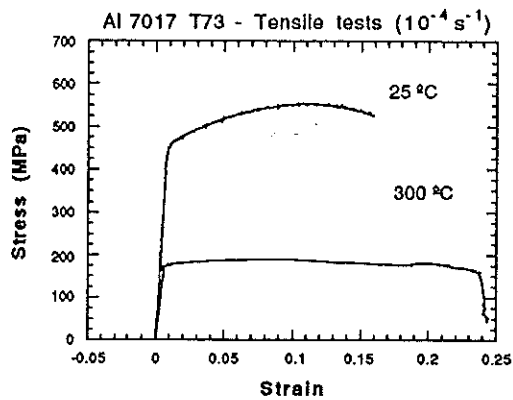


Figure 4. Stress-strain curves at low strain rate.

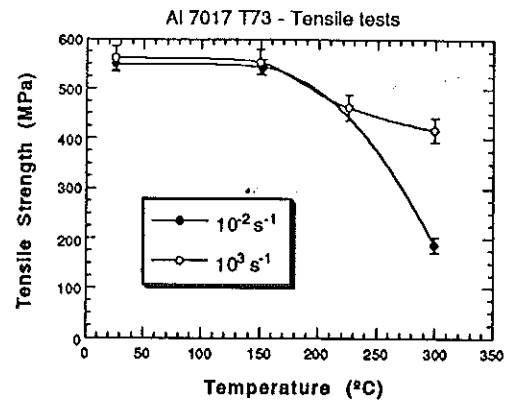


Figure 7. Tensile strength versus temperature.

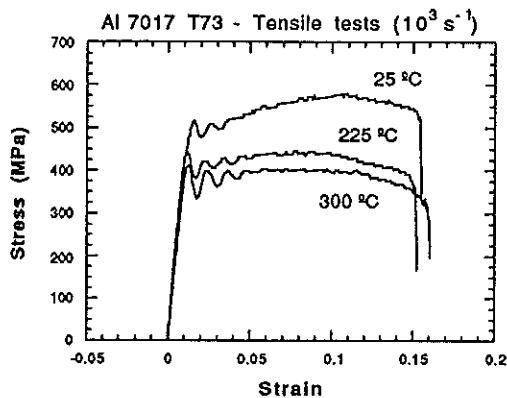


Figure 5. Stress-strain curves at high strain rate.

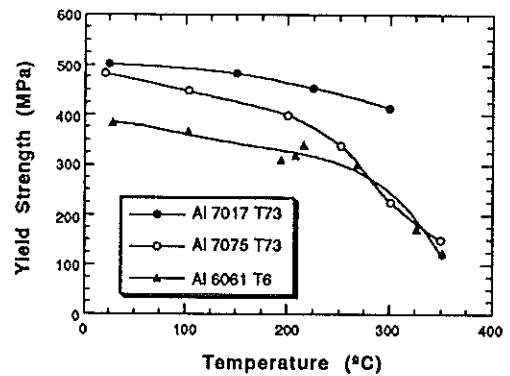


Figure 8. Comparison between several aluminium alloys.

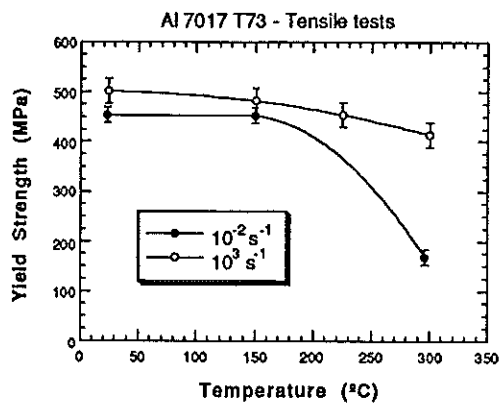


Figure 6. Yield strength versus temperature.

A fractographic study of the tested specimens has been made by means of scanning electron microscopy. The fracture surface observed in the tests carried out at high strain rate and room temperature is shown in figure 9. The rupture mechanism is ductile shear, as it can be appreciated from the marked direction observed in the photograph. The appearance of this surface is very similar to that of the slow strain rate in the same conditions of temperature. It is typical of highly textured alloys to show delaminations in the short transverse direction during the loading process [Venkateswara, 1989]. This mechanism is present in both the quasi-static and the dynamic tests.

On the other hand, the fracture surface corresponding to 300 °C of temperature shows clear differences: the rupture mechanism is by ductile nucleation, growth and coalescence of voids (figure 10). One of this voids generated around an inclusion can be seen in the figure 11.

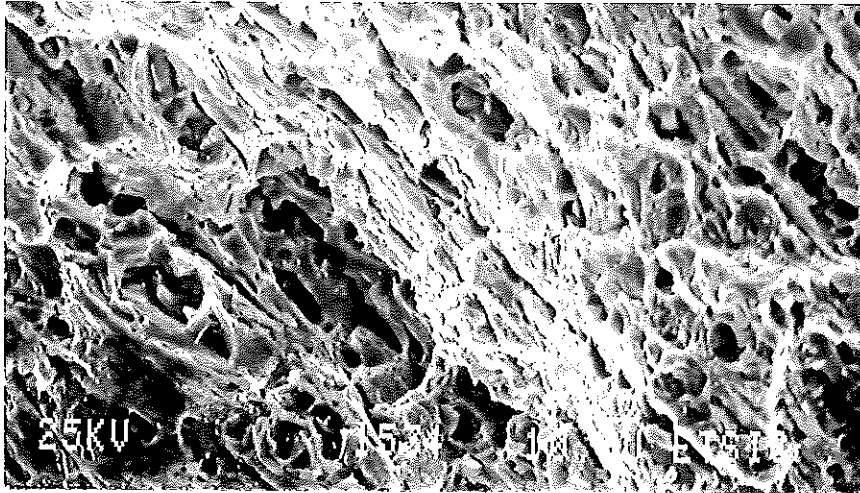


Figure 9. Fracture surface at 25 °C and 1000 s⁻¹.

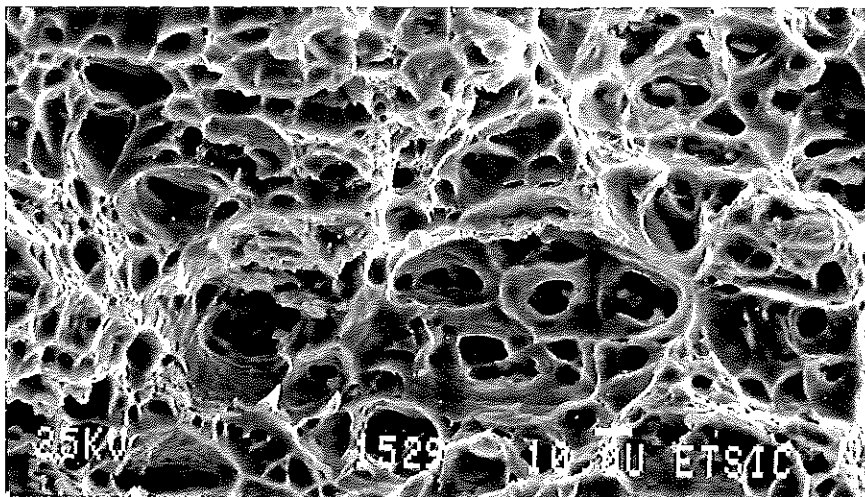


Figure 10. Fracture surface at 300 °C and 1000 s⁻¹.

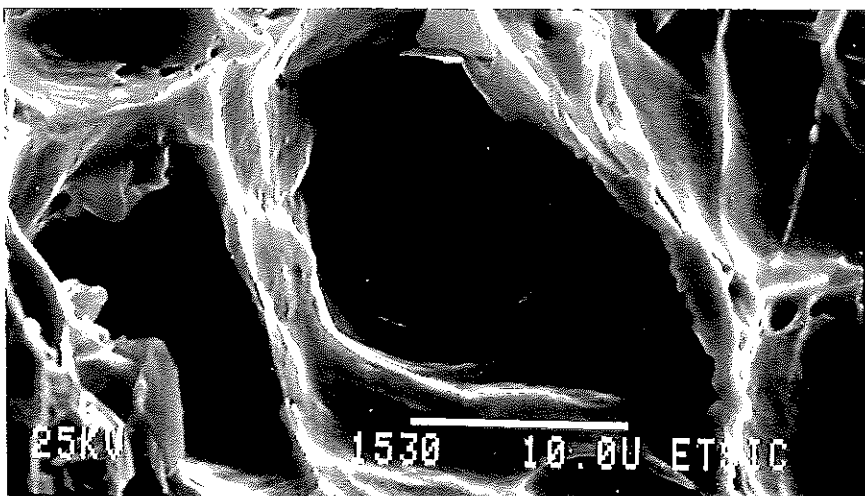


Figure 11. Detail of the fracture surface at 300 °C and 1000 s⁻¹.

DISCUSSION OF RESULTS

The main objective of this work was to investigate the strain rate sensitivity of the aluminium alloy 7017 T73 at different temperatures. From the experimental results it is confirmed that the low rate sensitivity of 7XXX aluminium alloys is valid up to 150 °C, approximately. Above this temperature, the differences between high and low strain rate behaviour become very important. However, there are not evidences of changes in the micromechanism causing the plastic flow. In fact, the heating of this alloy up to 300 °C is an additional overaging process and causes important structural changes: the precipitates growth with temperature and become incoherent with the matrix, losing their original role and making easier the dislocation movement and consequently, the yield strength decreases. In these conditions, we are treating with soft aluminium alloys which, as it is well known, are highly rate dependent. Probably these results would therefore be quite different if the heating process would be much faster as it might happen in dynamic conditions. This is an aspect deserves further research.

The material keeps its properties in a great extent up to the artificial overaging temperature, showing a very low strain rate sensitivity. In this range of strain rates and temperatures, it may be useful to describe the material behaviour through a phenomenological model of the Johnson-Cook type [Johnson, 1983] or similar.

The fractographic analysis has not shown evidences of changes in the rupture mechanisms with strain rate. On the contrary, the structural changes produced in the material as a consequence of temperature, are associated with two different rupture mechanisms: ductile shear at room temperature and nucleation, coalescence and growth of voids at 300 °C.

CONCLUSIONS

From the experimental results can be established the following outstanding conclusions:

- The aluminium alloy 7017 T73 has a markedly different rate sensitivity at room and elevated temperatures (above the artificial overaging temperature). This behaviour cannot be attributed to different micromechanisms of plastic flow, but to structural changes in the material.
- Under the overaging temperature, this material shows low rate sensitivity, and its behaviour may be represented through a Johnson-Cook type phenomenological model.
- There are not evidences of changes in the rupture mechanisms with the strain rate. On the contrary, temperature is a key factor: the material fails by ductile shear at room temperature, while at 300 °C the nucleation, coalescence and growth of voids is the controlling mechanism.

REFERENCES

- Burstow C.G. et al. 1988 - *The Response of 7075-T73 Aluminium Alloy at High Rates of Strain - Impact loading and Dynamic Behaviour of Materials* (Edited by C.Y. Chiem, H.D.Kunze y L.W. Meyer). DGM Informationsgesellschaft mbH Germany
- Campbell J.D. 1973 - *Dynamic Plasticity: Macroscopic and Microscopic Aspects - Materials Science and Engineering* 12, 3-21.
- Davies E.D.H. and Hunter S.C. 1963 - *The Dynamic Compression Testing of Solids by the Method of the Split Hopkinson Pressure Bar - J. Mech. Phys. Solids.*, Vol 11, p 155.
- Ellwood S.et al. 1982 - *A Tensile Technique for Materials Testing at High Strain Rates - J. Phys. E. Sci. Instrum.*, Vol. 15, 1982, pp 1169-1172.
- Harding J. et al. 1960 - *Tensile Testing of Materials at Impact Rates of Strain - J. Mech. Eng. Sci.*, Vol 2, p 88-96.
- Harding J. 1989 - *The development of constitutive relationships for material behaviour at high rates of strain.* - Int. Conf. Mech. Prop. Materials at High Strain Rates, Oxford , pp 189-203.
- Johnson G.R. and Cook W.H. 1983 - *A Constitutive Model and Data for Metals...*- Proc. Seventh Int. Symp.on Ballistics, La Haya, Holanda.
- Venkateswara K.T., Ritchie R.O. 1989 - *Mechanical Properties of Al-Li alloys - . Mat. Sci. and Tech.* , Vol 5, pp 882-895.
- Mondolfo L.F. 1971 - *Structure of the aluminium: magnesium: zinc alloys - Metals and materials*, Vol 5, pp 95-124.
- Polmear I.J. 1981 - *Light Alloys - Edward Arnold*, London.
- Rodríguez, J. 1993 - *PhD Thesis - Universidad Complutense de Madrid*.
- Rosenberg, Z. et al. 1986 - *A New Technique for Heating Specimens in Split Hopkinson Bar Experiments Using Induction Coil Heaters - Exp. Mech.* , pp 275-278.
- Steinberg, D.J. 1980 - *A Constitutive Model for Metals Applicable to High Strain Rate - J. App. Phys.* 51, p 1498.
- Zukas J.A. 1982 - *Impact Dynamics - John Wiley & Sons*, New York (U.S.A.).

**The stress-strain response of Al composite (2014/SiC15p-T6)
at strain rates between 10^{-2} and 400/s**

S.J. Savage, G. Thornell* and R. Gåhlin*

Division of Materials
National Defence Research Establishment
S-172 90 Sundbyberg, Sweden

*Dept. of Technology
University of Uppsala
S-751 21 Uppsala, Sweden

Abstract

Metal matrix composites are being seriously considered as a new generation of ballistic protection materials, and a number of recent reports indicate that the penetration depth of small calibre projectiles in aluminium-based composites is reduced, compared to the unreinforced alloy (even on a density normalised basis). The reasons for this improvement in protection are not clear, although Pageau et al ¹ relates it to the higher dynamic flow stress of the composite.

Very little data exists concerning the mechanical properties of metal matrix composites at higher strain rates, and it is the purpose of the present preliminary study (which describes work in progress) to increase our knowledge in this area.

The composite being studied is aluminium alloy 2014, reinforced with 15vol% silicon carbide particles. The composite was obtained from a commercial source, produced by spray deposition and subsequent extrusion and heat treated to the T6 condition. Tensile testing has been done in the longitudinal and long transverse directions, at strain rates of 10^{-2} /s and 10/s using a servo-hydraulic machine and at 400/s using an instrumented impact machine. Similar measurements of the matrix alloy without the reinforcement phase are on-going. Microstructural and fracture surface studies of the composite before and after tensile testing respectively have been made.

At all strain rates the transverse fracture stress and flow stress was lower than the equivalent longitudinal stresses, by about 30 MPa, confirming the anisotropy in the material which is seen in the microstructure. Both the fracture stress and the flow stress decreased slightly with increasing strain rate, the effect being somewhat greater for the flow stress than the fracture stress, as shown in the table below.

¹G. Pageau, R. Vaziri and A. Poursartip,, 23 Int. SAMPE TechConf Proc, Oct. 21-23, 1991, pp. 639-650.

Strain rate (s ⁻¹)	Longitudinal /Transverse	Fracture stress (MPa)	Flow stress 0,2% (MPa)	Fracture strain (%)
quasi-static*	-	380	440	7,0
0,01	L	550	500	5,5
0,01	T	515	480	3,4
10	L	540	n.a.	5,9
10	T	512	n.a.	3,1
400	L	530	468	4,5
400	T	502	455	2,3

literature value

Elongation to failure was in all cases lower for the transverse than for the longitudinal samples, and decreased with increase in strain rate for the T direction. A slight increase was noted for the L direction, when the strain rate was increased from 0,01 to 10/s, followed by a marked decrease on going to 400/s..

Post-test studies of the microstructure behind the fracture surface show extensive microcracking at 90° to the load direction, the cracks apparently initiating at particle/matrix interfaces.

Studies of the fracture surfaces are continuing, as are studies of crack initiation and propagation behind the plane of fracture, and will be reported fully later.

A COMBINED EXPERIMENTAL AND NUMERICAL TECHNIQUE TO DETERMINE THE DYNAMIC FLOW STRESS CONSTITUTIVE EQUATION FOR TYPE 304 STAINLESS STEEL

A.M. Hamouda and M.S.J. Hashmi

School of Mechanical & Manufacture Engineering, Dublin City University, Ireland

ABSTRACT

This paper presents a constitutive equation form and data for material subjected to high strain rates up to 10^5 S^{-1} and large strain. The experimental data are obtained from a ballistic test system over strain rates ranging from 10^3 to 10^5 s^{-1} . The basic technique involved firing of an elastic cylindrical projectile directly to a deformable cylindrical test specimen placed on an elastic anvil.

The cylindrical-impact test data was used to determine material constants in the proposed constitutive equation. This numerical technique taken into account inertia effect, strain hardening, elastic deformation of the projectile and anvil, and the effect of temperature rise during deformation and strain rate on strain hardening.

The temperature rise during deformation was investigated and found to alter the material constants and therefore affect the flow stress. However the effect of radial inertia was found to be less significant than temperature effect. Friction was investigated and its effect was minimised by using Polythene sheet lubricant, which proved to be adequate and effective.

DESCRIPTION OF FRACTURE MECHANISMS OF A DUCTILE STEEL AT HIGH LOADING RATES

H. Drar

Division of Solid Mechanics, Lund Institute of Technology
Box 118, S-221 00 Lund, Sweden

ABSTRACT

The fracture surfaces of precracked three point bend specimens of a ductile steel fractured at high loading rates are described. The specimens were fractured at initial impact velocities of 15, 29 and 43 m/s. All fracture surfaces showed three fracture modes, but with different proportions: intergranular dimple rupture, transgranular cleavage and transgranular shear-rupture dimple. The initial propagation of the main crack, for all cases, is caused by the same mechanism which yields a zone of intergranular dimple rupture. The extent of this rupture zone, as well as the fracture areas originate from the ductile fracture mechanism, decreases with increasing impact velocity.

INTRODUCTION

The most significant effect of increasing loading rate, ≥ 10 times, is to shift the quasi-static fracture toughness transition curve towards higher temperatures, i.e. to raise the temperatures at which cleavage may occur. The increase in loading rate may also result in two other effects: reducing the cleavage fracture toughness both on the lower shelf and in the temperature-dependent regime as well as increasing the crack growth resistance [Curry, 1984].

A study of a fracture surface can provide the following information relevant to the fracture process, [Boyer, 1974]: (a) an estimation of the force involved in breaking the piece, (b) an assessment of the degree of deformation that occurred during separation, and (c) the reason for material weakness in the path of that particular fracture.

This work studies the influence of the initial impact velocities 15, 29 and 43 m/s on the morphology of the fracture surface. The microscopic features of fracture surfaces revealed by scanning electron microscopy (SEM)

are discussed and illustrated, and the effects of high loading rates on fracture characteristics are described.

EXPERIMENT

The experimental material used in this investigation is characterized with respect to dynamic crack initiation and propagation, the procedural details and results being reported elsewhere, [Bergmark, 1991 and Drar, 1993]. The material was the Swedish microalloyed structural steel material SIS 142134 (similar to steel Grade E355, quality DD of ISO 4950/2) with carbon equivalent not exceeding 0.41%. The specimens of size 320 x 75 x 18 mm had a single notch and they were precracked by fatigue. The length of the notch plus the initial pre-fatigued crack was one quarter of the specimen height (about 19 mm). These specimens were supported at the mid sections and hit at the ends by a U-shaped hammer at impact velocities of 15, 29 and 43 m/s.

Fractographic studies were conducted by a JEOL 840A SEM operating in secondary electron imaging mode at an accelerating voltage of 10 kV. All SEM fractographs were taken with the incident electron beam oriented 90° to the fracture surface.

The areas covered by brittle flat surfaces were measured on enlarged photographs with the help of a planimeter. The percent ductile fracture appearance was then calculated according to ASTM E604-88, [ASTM, 1990].

RESULTS

All fracture surfaces were visually examined, Fig. 1. Three different regions marked A, B and C, were identified. Using the terms recommended by [Srawley, 1964], region A can be characterized as brittle flat fracture

while region B can be characterized as ductile flat fracture and C as ductile slant fracture.

The relative ductile fracture appearance was found to be 91.5, 64.5 and 46 for the fracture surfaces obtained at impact velocities of 15, 29 and 43 m/s, respectively.

SEM fractographs, for all impact velocities, showed that the initiation of the main crack in front of the pre-fatigued crack tip is a ductile flat fracture (B-type). This B-type fracture consists of dimple rupture, which may be characterized by the formation and coalescence of microvoids. The extent of the B-zone decreases with increasing impact velocities: about 5 mm for the 15 m/s impact velocity and about 100 μm , for the 29 and 43 m/s impact velocities.

The initiated cracks, by mechanisms involving void growth and coalescence, grew by different mechanisms depending on the actual loading rate. The successive positions of crack fronts obtained at 29 and 43 m/s impact velocities can be followed in the optical photographs shown in Fig. 1. In these specimens, the crack front is roughly parabolic with the most advanced point at the mid-thickness. In the specimen impacted by 15 m/s velocity, the fracture surface is asymmetric relative to the specimen mid-plane, with the exception of a triangular shaped flat fracture in the vicinity of the fatigue crack tip. Successive crack fronts cannot be identified for the 15 m/s experiment.

For regions marked A in Fig. 1, i.e. brittle flat fracture, the fracture is basically transgranular cleavage with some intergranular domains containing an amount of ductile tearing on the cleaved grain boundary facets, see Fig. 2a. Several microcracks can be seen at high magnification of this area, Fig. 2b.

Regions marked B, i.e. ductile flat fracture, display dimple rupture fracture mode. This is independent on whether the B-fracture zone occurs near the pre-fatigued crack tip, and therefore is classified as a crack initiation zone, or if the B-fracture takes place at other places, cf. Fig. 1. The mechanics of B-fracture is shown in Fig. 3, where the high magnification, Fig. 3b, reveals the process of microvoid coalescence as the mechanism which triggered this dimple fracture mode.

The C-type of fracture, i.e. ductile slant fracture, is shown in Fig. 4. Essentially all of the features seen in Fig. 4 are dimples, which prove that the region is a ductile zone. The large dark regions, in Fig. 4a, are either "valleys" of dimples or partially large voids with fragments of oxides seen as bright spots inside such dark zones. At high magnification, Fig. 4b, small visible dimples clustered around the hillside are shown in the central region of this fractograph.

DISCUSSION

The mechanism by which fracture propagates in the A-regions (flat cleavage fracture) is by crystal separation along certain crystallographic planes, cf. Fig. 1b. Cleavage therefore leads to a fracture surface composed of flat, shiny facets. The crack is essentially flat and lies approximately normal to the maximum principal tensile stress axis, but changes its orientation slightly when it crosses

a grain boundary due to the interaction of the different properties of adjacent grains. Fracture in metal is always preceded and accompanied by some plastic deformation. In all the examined specimens, this plastic deformation manifests itself in the cleavage A-regions in terms of ductile tearing on the exposed grain boundary, cf. Fig. 1a. Since two fracture mechanisms are active in the A-regions (creation of tear ridges and flat facets) the term *quasi-cleavage* fracture is conveniently used, [Mills, 1987].

The mechanisms by which fracture propagates in ductile fracture areas (being flat or slant) can be characterized by the formation and coalescence of internal microvoids. However, in ductile flat fracture areas, the resulted dimples have no directional preference and the path of fracture is intergranular. Therefore, such fracture areas are caused by tearing. In ductile slant fracture areas, moderately elongated dimples, often with directional preference, were observed. The fracture path is transgranular. The load causing this fracture type is a combination of at least two loading modes: tear and shear.

Different loading rates results in different proportions of these fracture types. The lowest loading rate studied (15 m/s impact velocity) results in relatively small areas of brittle and flat-ductile fracture type but a large area of slant ductile fracture type. With increasing loading rate, the amounts of slant-fracture decrease and those of brittle fracture type increase. The relative brittle fracture appearance in the examined specimens impacted by 15, 29 and 43 m/s, are 8.5, 35.5 and 54, respectively.

The initiation of the main crack at the fatigue crack tip seems to take place by the same fracture mode regardless of the loading rate, i.e. by dimple rupture mode, cf. Fig. 5. These fractographs reveal that the voids at the main crack initiation front may have nucleated from the large nonmetallic inclusions in the material.

From the distribution of the different fracture types, the sequence of the main crack propagation is believed to be flat ductile (initiation), brittle and slant fracture. This sequence is repeated a number of times depending on the loading rate; once for the 15 m/s impact velocity and twice for the 29 and 43 m/s impact velocities.

CONCLUSIONS

The investigation clearly demonstrates that different fracture mechanisms compete in a dynamic fracture test. Three different fractures could be identified.

- brittle flat fracture regions (A-type) where the transgranular cleavage fracture mode may be described as quasi-cleavage. This fracture type is a result of mainly a tear loading condition.
- ductile flat fracture (B-type) where a dimple rupture fracture mode is observed. The dimples have no directional preference and the path of this fracture is intergranular. Also this fracture type is mainly caused by tearing.
- ductile slant fracture (C-type) with moderately elongated dimples often having a directional pref-

erence. The fracture path is transgranular. The load causing this fracture type is a combination of at least two loading modes: tear and shear.

Different loading rates results in different proportions of these fracture types. The lowest loading rate studied (15 m/s impact velocity) results in relatively small areas of A- and B-fracture type but a large area of C-fracture type. With increasing loading rate, the amounts of C-fracture decrease and those of A-type increase.

The initiation of the main crack at the fatigue crack tip takes place by the same fracture mode (B-type) regardless of the loading rate.

From the distribution of the different fracture types, the sequence of the main crack propagation is believed to be B (initiation), A and C.

ACKNOWLEDGEMENTS

The work is sponsored in part by the Swedish Board for Technical Development (STUF).

REFERENCES

- ASTM E604-88. 1990 - *Standard Test Method for Dynamic Tear Testing of Metallic Materials* - Annual Book of ASTM Standards, Vol. 03.01; pp. 595-602, Philadelphia.
- BERGMARK A. and KAO H.R. 1991 - *Dynamic Crack Initiation in 3PB Ductile Steel Specimens* - Report LUTFD2/(TFHF-3041), Div. of Solid Mechanics, Lund Institute of Technology, Lund, Sweden.
- BERGMARK A. and CHO J.U. 1991 - *Dynamic Crack Propagation in 3PB Ductile Steel Specimens* - Report LUTFD2/(TFHF-3045), Div. of Solid Mechanics, Lund Institute of Technology, Lund, Sweden.
- BOYER H.E. Ed. 1974 - *Metals Handbook* - Vol. 9; ASM Metals Park, Ohio.
- CURRY D.Y., MILNE I. and GATES R.S. 1984 - *The Influence of a High Loading Rate on the Fracture Behaviour of a Pressure Vessel Steel*. Mater. Sci. Engng. Vol. 63; pp.101-109.
- DRAR H. and BERGMARK A. 1993 - *Load Rate Influence on the Fracture Morphology of a Ductile Steel*. Engng Fracture Mech.; in press.
- MILLS K. Ed. 1987 - *Metals Handbook* - Vol. 12; ASM Metals Park, Ohio. SRAWLEY J.E. and BROWN W.F. JR. 1964 - *Fracture Toughness Testing Methods*. ASTM STP 381, pp.133-196.

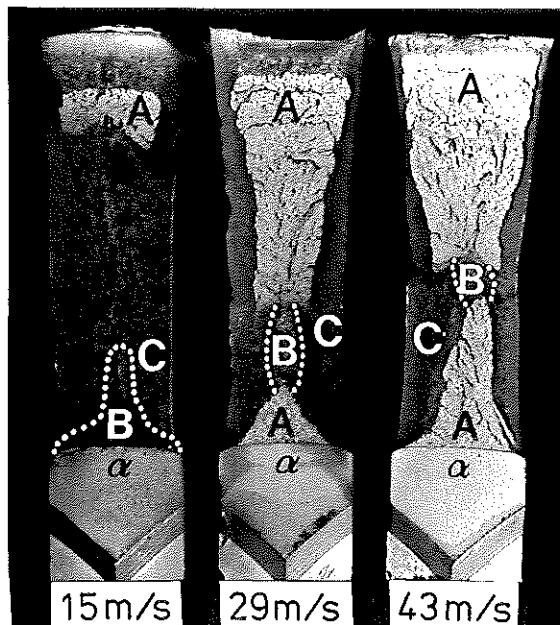


Figure 1: Optical fractograph showing fracture areas A, B and C. α marks the pre-fatigue crack.

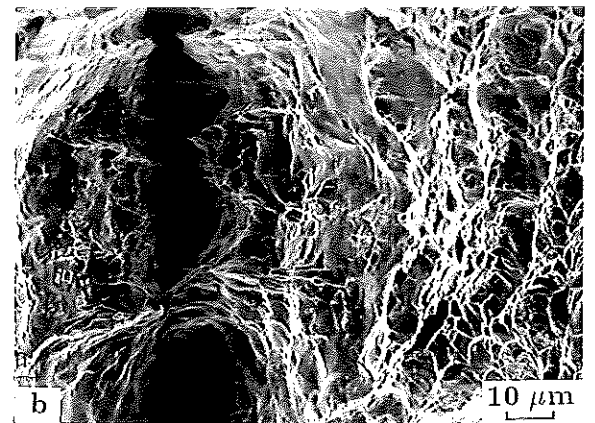
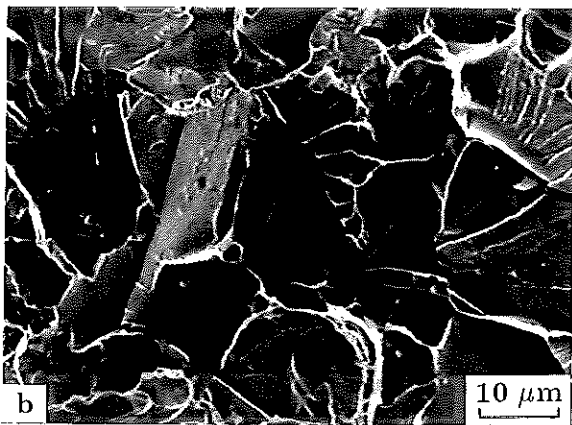
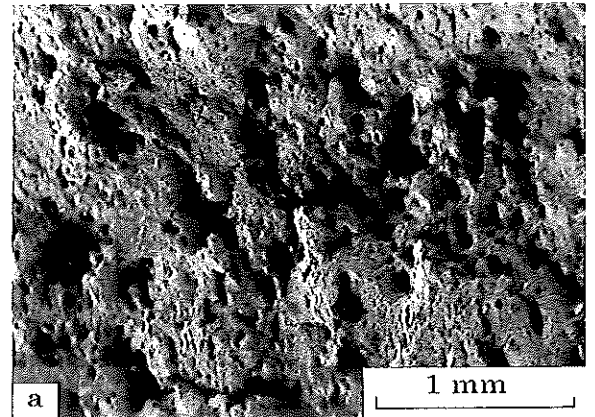
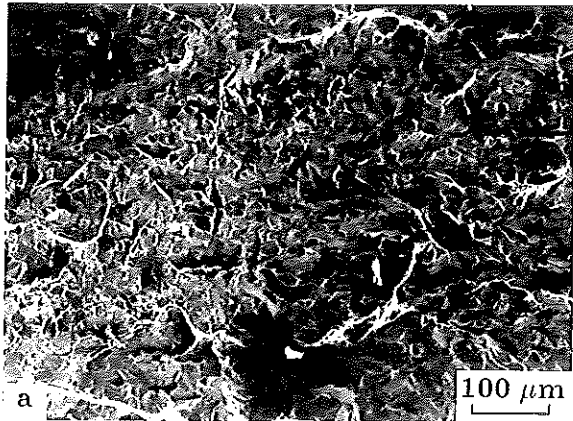


Figure 2: SEM fractographs of A-type fracture. (43 m/s)

Figure 3: SEM fractographs of B-type fracture. (29 m/s)

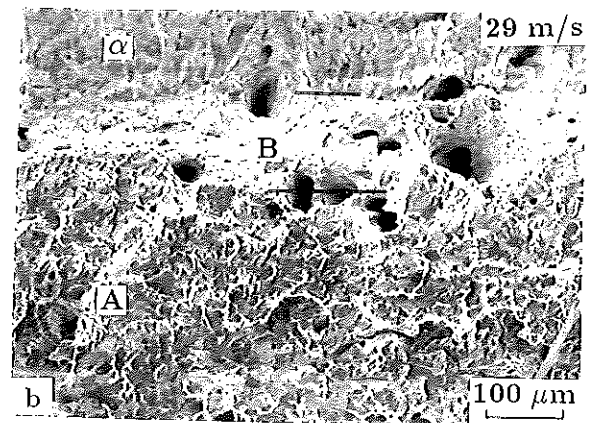
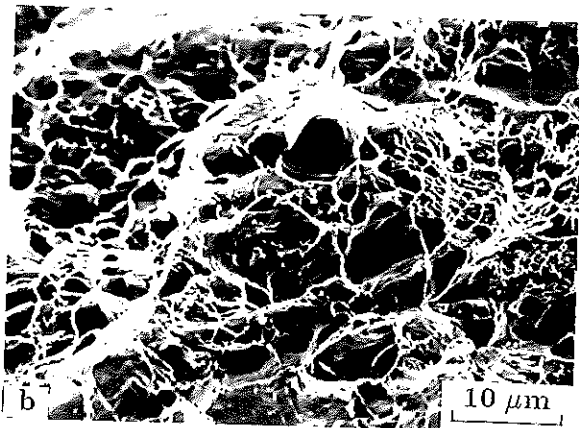
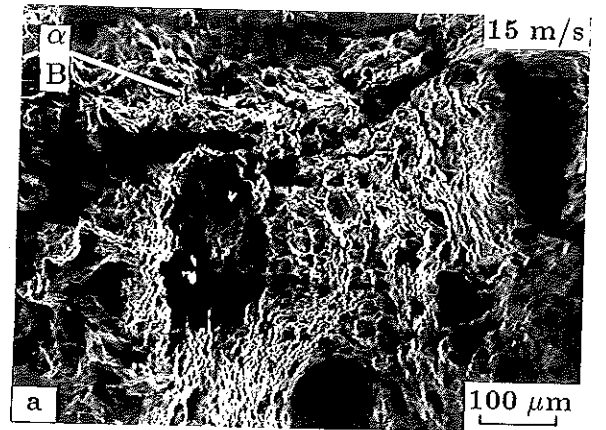
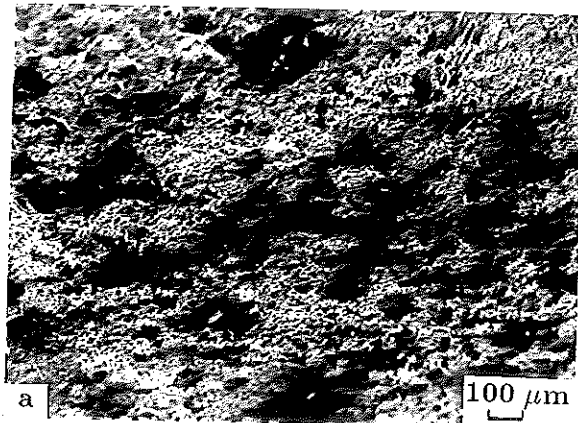


Figure 4: SEM fractographs of C-type fracture. (43 m/s)

Figure 5: Main crack propagation zone, cf. Fig. 1.

EFFECT OF MICROSTRUCTURE ON THE FRACTURE OF Al-2124/SiC_p COMPOSITES

Limin LUO, Zhong LING, Jian JIANG, and Bradley DODD
Department of Engineering, University of Reading
Reading, Berks, U.K. RG6 2AY

ABSTRACT

The aim of this study is to reveal the fracture modes of Al-2124/SiC_p and the role of microstructure on their fracture from the ductility point of view. The materials were tested under tension and compression quasi-statically and dynamically after heat treatment. Optical microscopy and SEM were used for micro-examination. Different fracture modes were found for the materials tested under different stress states. The accumulation of micro-damages nucleated at the sharp end and due to the break of reinforcing particles is responsible for tensile fracture. And the localised flow of the matrix and cracking from localised region is the governing mechanism for fracture under compression. Tests carried out on specimens after different heat treatments showed the strong influence of precipitates on compressive ductility but in tension the precipitates had less and reverse influence.

INTRODUCTION

Recently there has been much interest in aluminium alloys reinforced with SiC particles to provide lightweight, high performance (strength, stiffness, wear resistance etc) structural materials which are suitable for advanced engineering applications such as aerospace, automotive, and leisure industries. Particulate reinforced metal matrix composites (MMCs) are much cheaper than other types of MMCs and relatively isotropic. And one of their prime advantages is that most processing technologies developed for monolithic alloys can still be used.

The inclusion of a large number of reinforcing particles in aluminium alloys enhances their strength by mechanisms such as transferring load, restricting the movement of dislocations, influencing matrix grain size, and/or causing residual stress, but at the same time reduces

their ductility. The low ductility is one of their main drawbacks since this makes them very difficult to process. One of the purposes of this study is trying to find some possible ways to improve their ductility.

Previously published studies on particulate MMCs have been concerned with their fatigue, fracture toughness, residual stress etc. Few results were found on fracture from the ductility point of view. Harding et al (1987) reported the increase of tensile ductility of SiC whiskers reinforced Al-2124 with increasing strain rate. Higashi et al (1992) studied high temperature superplastic behaviour of mechanically alloyed IN 9021 reinforced with SiC particles which showed an increase in elongation with strain rate at high temperature (823K). Humphreys et al (1990) studied the microstructural development during thermo-mechanical processing of particulate MMCs. Liu et al (1989) studied the tensile ductility of a 2xxx aluminium alloy reinforced with 15% vol SiC particulate under superimposed hydrostatic pressure and showed that voids are formed in association with cracked SiC particles and the pressure acts to suppress the voids, thus increasing ductility. In an in situ study Da Silva et al (1988) found for Al-2124 reinforced with 25% vol SiC particles that fracture initiates from the opening of precracked particles and decohesion at particle poles. Schueller et al (1990) showed the growth of precipitates with increasing cooling time from the solution temperature of 510°C down to 150°C.

The main microstructure of Al-2124/SiC_p is grains, SiC particles, precipitates, subgrain structures, dislocations. In this work we confine ourselves to the effect of SiC, precipitates, grains and their interfaces and boundaries on fracture initiation and propagation, emphasising their influence on the ductility of the materials.

EXPERIMENTAL PROCEDURE

The materials under study are Al-2124 alloy reinforced with 20% by weight of $3\mu\text{m}$ and $13\mu\text{m}$ SiC particles respectively. As a comparison Al-2124 alloy was also tested. All specimens were machined from 12mm thick rolled plates. All specimens were taken with the specimen axis in-plane. Tensile tests were carried out at a strain rate of about $1 \times 10^{-3} \text{ s}^{-1}$ using an Instron testing machine. The specimen sizes are 18mm (gauge length) by 4mm (diameter). Quasi-static compression tests were performed on an Avery universal testing machine with specimen dimensions of 11mm (height) by 11mm (diameter) while dynamic compression tests were carried out at a strain rate of 3000 s^{-1} using a SHPB system with a specimen size of 5mm (height) by 5mm (diameter).

Two heat treatments were applied to study the influence of precipitates on fracture and ductility. The first is solution heat treatment at 530°C for 55min followed by water quenching and the second is over-aging at 250°C for 1.5 hrs.

RESULTS

The basic microstructure of Al-2124/SiC are shown in figure 1. The matrix grains were layered and in-plane isotropic. It is found that the main precipitates are intermetallic particles Al_2Cu , AlCu_2Mn , and Al_2CuMg of needle and sphere shapes [Sellier and Le Petitcorps, 1993]. The density of Al_2Cu is very high and well distributed in the matrix. Their size is up to $3\text{-}4\mu\text{m}$ depending on their heat treatment condition [Schueller et al, 1990].

Tensile tests were carried out for Al-2124 and Al-2124/SiC_p($3\mu\text{m}$) after solution heat treatment and over aging respectively. Four tests were carried out for each condition. Typical stress-strain curves are shown in figure 2. Solution treated specimens have a much higher strength as well as larger elongations than over aged ones. An interesting phenomenon was found that though solution treated Al-2124/SiC_p has larger elongation than the over aged material, the macroscopic fracture mode is a brittle one with little necking before fracture while the over-aged one had more necking prior to fracture. Both had fracture surfaces 45° to the loading axis. Reflected on stress-strain curves the solution treated specimens fracture at peak loads while the over-aged ones fracture after the load has dropped from the peak.

Al-2124 solution treated specimens fracture at 45° degree to loading axis after necking while over-aged ones had more severe necking before fractured ductilely without a macroscopically smooth fracture surface.

Micro-examination revealed a large degree of micro-damage initiated at the particle poles and due to the opening of broken particles near the fracture surface in Al-2124/SiC_p ($3\mu\text{m}$), see figure 3(a) (SEM). This is in agreement with previous results obtained by other researchers. But almost no micro-damage considerably larger than $3\mu\text{m}$ was found, this means that the growth of micro-damage is very limited. Fractography of Al-

2124/SiC_p($3\mu\text{m}$), figure 3(c) (SEM), shows that major dimples are about 3 microns surrounded by some smaller ones. Figure 3(b) (SEM) shows the damage in Al-2124 associated with broken and elongated precipitate particles near the fracture surface. These indicate that the accumulation of micro-damage associated with big particles (both SiC and precipitated ones) leading to a sudden break is the fracture mechanism for Al-2124/SiC_p($3\mu\text{m}$) in tension. The basic features of the above described microstructure are the same for both solution treated and over-aged specimens.

The main microstructural difference induced by the two heat treatments is that after solution treatment there are a large amount of copper solution, small dispersoids and precipitates but very few big precipitates in the matrix while over-aging makes the matrix almost pure aluminium with a lot of well distributed precipitates many of them of the same size as SiC particles ($3\mu\text{m}$) which can easily be identified under optical microscopy. The difference in strength caused by the two heat treatments can be explained by the hardening mechanism of copper atoms and small particles in the matrix through their reaction with dislocations the same as alloy hardening. The smaller elongation of the over-aged specimens is due to the existence of more and larger precipitates which accelerated the fracture process overcoming the ductile effect of softer matrix. The softer matrix of over-aged Al-2124/SiC_p contributes to the more severe necking.

Al-2124, Al-2124/SiC_p ($3\mu\text{m}$) and Al-2124/SiC_p ($13\mu\text{m}$) were tested quasi-statically (strain-rate about $1.5 \times 10^{-3} \text{ s}^{-1}$) and dynamically (strain-rate about 3000 s^{-1}) after the two heat treatments.

Macroscopically all specimens started to fracture with surface cracks 45° to the loading axis except that quasi-statically loaded over-aged Al-2124 specimens did not fracture after 80% height reduction. The anisotropy caused by rolling or microstructurally layered grains makes specimens deforming from cylinders to roughly elliptical shapes. The larger deformation direction is through thickness direction and the surface cracks always appear first at surfaces where the normal directions are close to the short elliptic axis, indicating the effect of the layered grains. Solution treated specimens had much higher strength than over-aged ones as expected, but they had much lower ductility than over-aged ones, contrary to the case in tension, see figure 4. The stress-strain curves of Al-2124/SiC_p ($13\mu\text{m}$) are similar to those of Al-2124/SiC_p ($3\mu\text{m}$) with slightly larger ductility. There is not much hardening effect of strain-rate on these materials. However their ductility is much higher at high strain-rates except that of over-aged Al-2124. This is in agreement with the result obtained by Harding et al (1987) on Al-2124/SiC_w and Higashi et al (1992) on IN 9021/SiC_p but contrary to conventional materials.

Micro-examination showed that localized deformation bands were formed before surface cracks. It was found that bands formed in solution treated specimens under dynamic loading are narrow shear bands while those under quasi-static loading are broader, see figure 5(a)-(d).

While particles in Al-2124/SiC_p (3μm) were flowing and rotating with matrix in localised deformation region figure 5(a)(b), big particles in Al-2124/SiC_p (13μm) seemed standing still and matrix flew between big particles, figure 5(c)(d). Cracks initiated and propagated in the bands, figure 5(b)(d). Some small voids were found in the bands and near the main crack, but most of them are not associated with reinforcing particles, see figure 6(a)(b). Also found were broken particles which did not open, see figure 6(a). The growth of cracks are through the matrix and in some cases links separated interfaces between the particles and the matrix, see figure 6(b)(c).

The fracture mechanism for the materials in compression can be described as localization of deformation into bands and initiation and growth of cracks in the bands which leads to the final fracture. The formation of bands is matrix controlled not particularly associated with reinforcing particles or big precipitates. The higher strength of solution treated materials is due to the same hardening mechanism as in tension. The substantially larger ductility of over-aged materials is caused by the softened and ductile matrix since the big hydrostatic pressure in compression tests suppressed the possible damage associated with big particles. It is worth noting here that the much improved ductility induced by over-aging has significant implication in the processing of these materials, e.g. forming. The exact mechanism of better ductility at higher strain-rates of these materials is not clear.

CONCLUSION

Tensile and compressive tests were carried out for Al-2124/SiC_p (3μm) and Al-2124/SiC_p (13μm) as well as Al-2124 under quasi-static and dynamic loading. Fracture mechanisms and effect of micro-structure were studied. It was found that

(1) a large degree of micro-damage initiated at particle poles and due to the opening of broken particles, the accumulation of micro-damage lead to the final fracture of the materials under tension.

(2) the existence of more and larger precipitates induced by over-aging accelerated the tensile fracture process, overcoming the ductile influence of the softer matrix.

(3) localization of deformation into bands and crack initiation and growth in the bands is the governing fracture mechanism for the materials under compression

(4) narrow shear bands were formed in the solution treated MMC materials under dynamic compression.

(5) the formation and cracking is not particularly associated with big particles in the materials.

(6) the layered grains caused by rolling contributed to the anisotropic deformation.

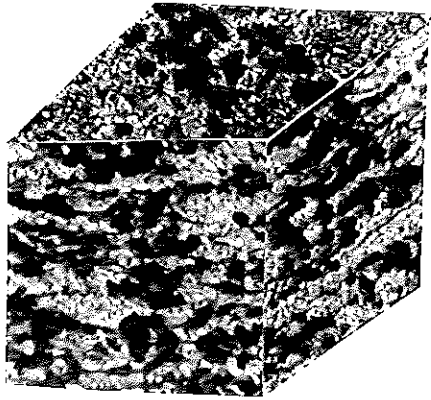
(7) at higher strain-rate the materials have better ductility.

This work is partly supported by a BRITE-EURAM project No. BE-4500-90 (Brite-Euram-CT91-0398). Ling ZHONG would like to express her gratitude for the support from The Chinese Academy of Sciences and The Royal Society.

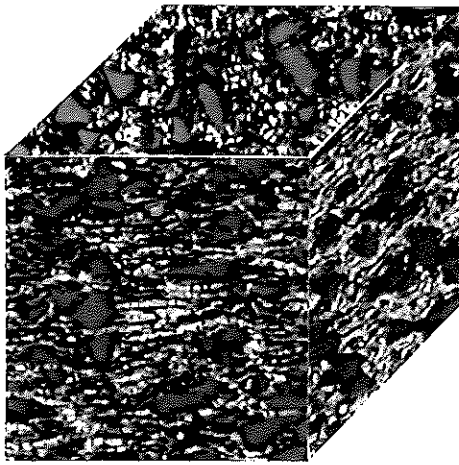
REFERENCES

- DA SILVA R., CALDEMAISON D., and BRETHEAU T. 1988 - *Micromechanical behaviour of Al/SiC composite materials subjected to plastic deformation: an in situ study*, in *Mechanical and Physical Behaviour of Metallic and Ceramic Composites* (ANDERSEN S.I., LILHOLT H., PEDERSEN O.B., eds) - RISO National Laboratory, Roskilde, Denmark. pp. 333-338.
- HARDING J., TAYA M., DERBY B., and PICKARD S. 1987 - *An investigation of the high strain rate deformation of SiC_w/2124 Al composites*. in *ICCM-6/ECCM-2* (MATHEWS F.L., BUSKELL N.C.R., HODGKINSON J.M., and MORTON J., eds). Elsevier Applied Science, London. Vol. 2; pp. 224-233.
- HIGASHI K., OKADA T., MUKAI T., TANIMURA S., NIEH T.G., and WADSWORTH J. 1992 - Superplastic behaviour in a mechanically alloyed aluminium composite reinforced with sic particles. *Scripta Metall. et Mater.* Vol. 26; pp. 185-190.
- HUMPHREYS F.J., MILLER W.S., and DJAZEB M.R. 1990 - *Microstructural development during thermo-mechanical processing of particulate metal-matrix composites*. *Mater. Sci. Tech.* Vol. 6; pp. 1157-1166.
- LIU D.S., MANOHARAN M., and LEWANDOWSKI J.J. 1989 - Effects of microstructure on the behaviour of an aluminium alloy and an aluminium matrix composite tested under low levels of superimposed hydrostatic pressure. *Metall. Tran. A.* Vol. 20A; pp. 2409-2417.
- SCHUELLER R.D., and WAWNER F.E. 1990 - The effects of hot rolling on AA2124 15 v/o SiC whisker composites. *J. Composite Mater.* Vol. 24; pp. 1060-1076.
- SELLIER E., and LE PETITCORPS J. 1993 - in Annual report on project BE-4500-90(Brite-Euram - CT91 - 0398) "*Workability of Metal and Metal Matrix Composites, in particular Al-Li Alloys and Al based Composites*" June 1993.

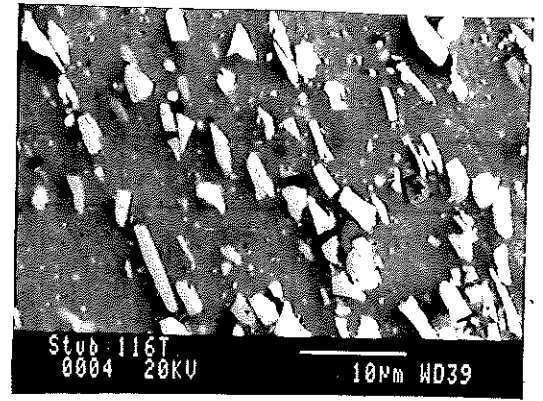
ACKNOWLEDGEMENTS



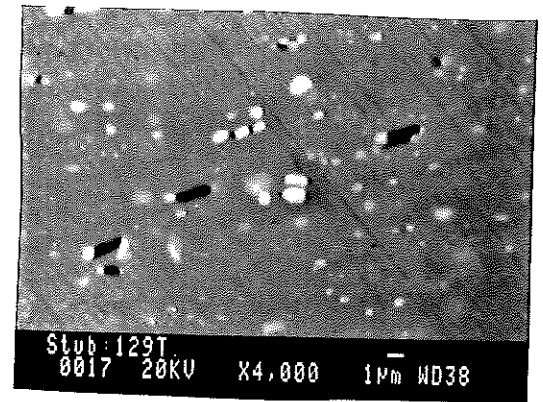
(a) x500



(b) x300



(a)



(b)

Figure 1 Basic microstructure of Al-2124/SiC
(a) 3μm particles (b) 13μm particles

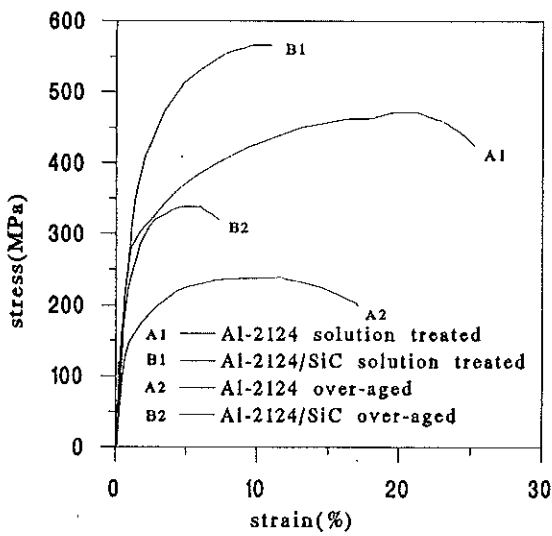
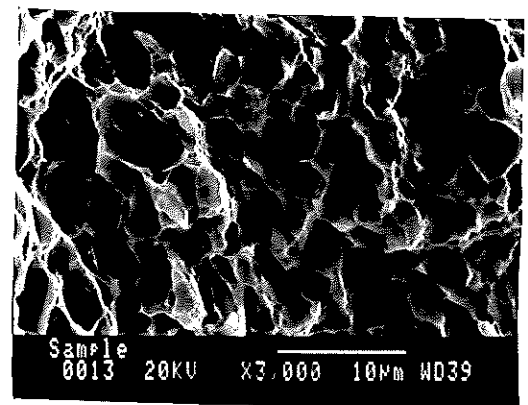


Figure 2 Tensile stress-strain curves of Al-2124 and Al-2124/SiC_p(3μm) after different test treatments



(c)

Figure 3 Tensile micro-damage and fractography (a) Al-2124/SiC_p (3μm) broken particles and decohesion at particle poles (b) Al-2124 broken and elongated precipitates (c) fracture surface of Al-2124/SiC_p(3μm)

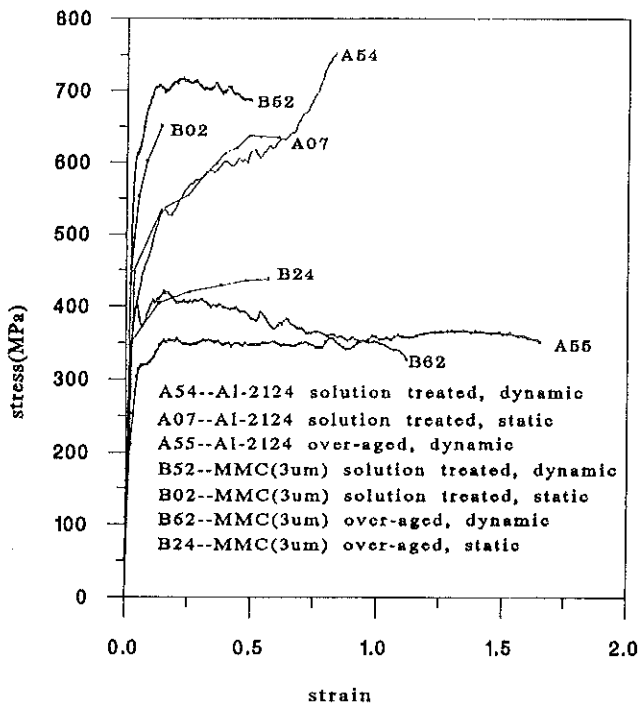
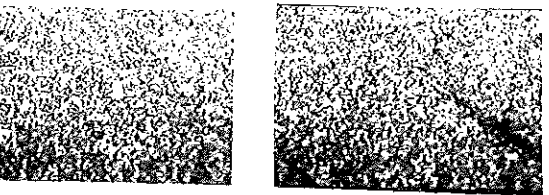
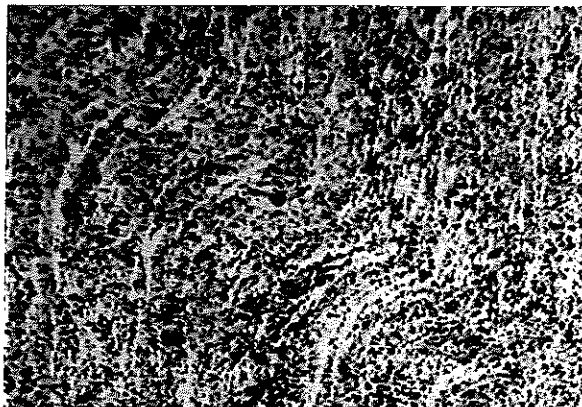
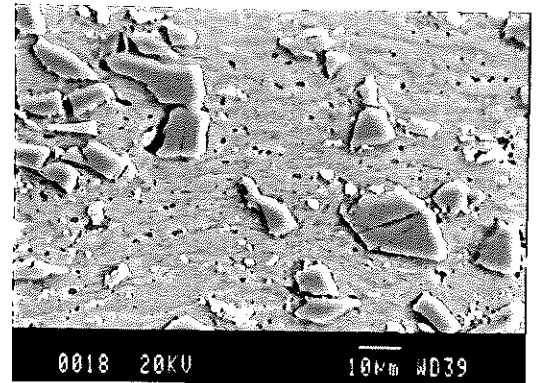


Figure 4 Compressive stress-strain curves of Al-2124 and Al-2124/SiC (3um)

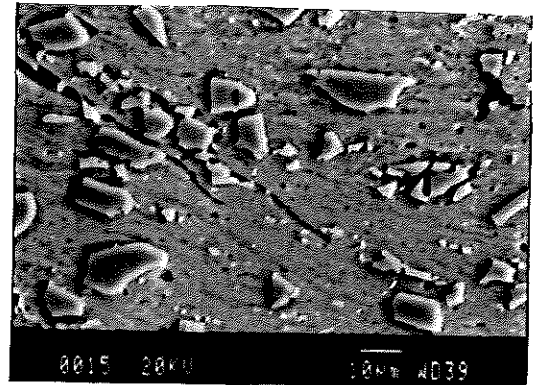


(d) dynamic

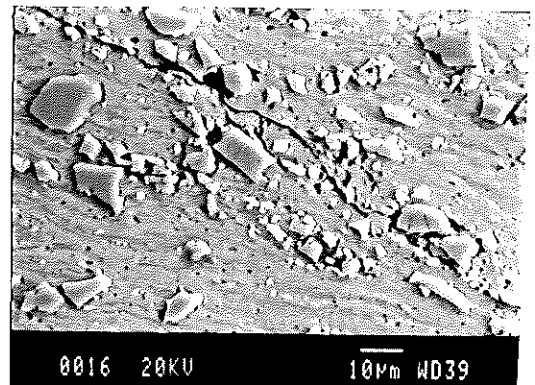
Figure 5 Localised flow in compression (a) Al-2124/SiC (3um) particles flow and rotate with the matrix (b) Al-2124/SiC (3um) shear band and crack in the band (c) Al-2124/SiC (13um) matrix folw between big particles (d) Al-2124/SiC (13um) shear band and crack in the band



(a) small voids and broken particles



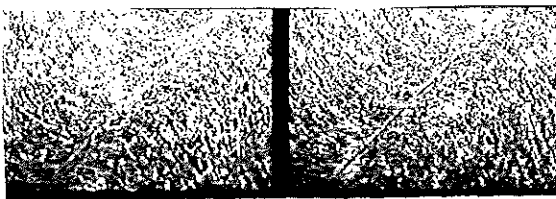
(b) main crack and small voids



(c) crack and link with debonded particles

Figure 6 Al-2124/SiC (13um) under dynamic compression

(a) Quasi-static x100



(b) dynamic



(c) Quasi-static x380

DUCTILE FRACTURE DURING TENSILE HOPKINSON BAR AND PLATE IMPACT TESTING

M.J. Worswick* H. Nahme** J. Clarke* J. Fowler*

*Department of Mechanical and Aerospace Engineering
Carleton University
Ottawa, Ontario, Canada K1S 5B6

**Ernst-Mach-Institut
Eckerstraße 4, 7800 Freiburg, Germany

ABSTRACT

The process of ductile fracture through void nucleation, growth and coalescence under strain rates in the range $10^3 - 10^4 \text{ s}^{-1}$ is studied. The material considered is UNS C36000 free cutting brass containing spheroidal lead particles which serve as void nucleation sites. Tensile Split Hopkinson Bar and Plate Impact tests have been performed to examine stress-strain and fracture behaviour under high rate loading conditions.

This paper presents results from the mechanical testing and metallographic observations of damage within tested samples. Measured damage and spall strengths are compared with predictions using LS-DYNA2D calculations employing a Gurson-based constitutive model. The model is shown to provide good predictions of spall strength but is thought to over-predict void growth rates.

INTRODUCTION

Ductile fracture is a mechanism of failure operative under the high strain rate conditions associated with impact [Curran, 1987; Worswick, 1991b] and explosive loading of metals [Worswick, 1990; Tang, 1991]. Numerous experimental and analytical investigations have considered the component stages of ductile fracture, namely void nucleation, growth and coalescence, under quasi-static loading. Considerably less attention, however, has been devoted to the effects of material rate sensitivity and inertia on the ductile fracture process during high strain rate loading.

This paper presents initial results from a study of ductile fracture under high strain rate loading conditions. The experimental part of this work has been carried out using the Tensile Split Hopkinson Bar at Carleton University and the Plate Impact Facility at Ernst-Mach-Institut. The objectives of these experiments are to obtain measurements of constitutive softening due to porosity and growth of voids at high strain rates. The use of these different facilities has permitted measurements under a variety of strain or stress

states and strain rates in the range $10^3 - 10^4 \text{ s}^{-1}$.

The material under study is UNS C36000 free-cutting brass. While of little interest in high strain rate technological applications, this material is of interest in the current study as a "model material" since it contains a dispersion of spheroidal lead particles which tear or debond during tensile deformation to nucleate voids. This material has also been utilized in previous symmetric Taylor cylinder experiments [Worswick, 1991b].

Supporting numerical studies have been performed using the LS-DYNA2D [Hallquist, 1988] finite element code modified to incorporate the Gurson [1975] constitutive model. This model accounts for the destabilizing influence of voids or porosity within a plastically deforming material and predicts the growth of voids during tensile plastic deformation. Of interest in the current study is the applicability of the Gurson constitutive model, which is formulated for quasi-static conditions, to dynamic loading.

Metallographic results concerning the mode and nature of the fracture will be presented. Comparison between predicted and measured free surface velocities from the plate impact experiments is also given.

MATERIAL

Figure 1 is an optical micrograph showing the material prior to testing. The as-received material is annealed at $840 - 850^\circ\text{C}$ for two hours. The effect of the anneal is to promote spheroidization of the lead phase as seen in the micrograph. The brass matrix is predominantly alpha phase with small regions of beta phase. The grain size is typically $50 - 55 \mu\text{m}$ while the average lead particle size is roughly $5 \mu\text{m}$. The in-plane mean "nearest-neighbour" lead particle spacing is approximately $15 \mu\text{m}$ and the volume fraction of lead particles is 0.025.

Some TSHB specimens were tested in the as-received (non-annealed) condition to examine the effect of hardening rate and particle size on ductility. All of the plate impact

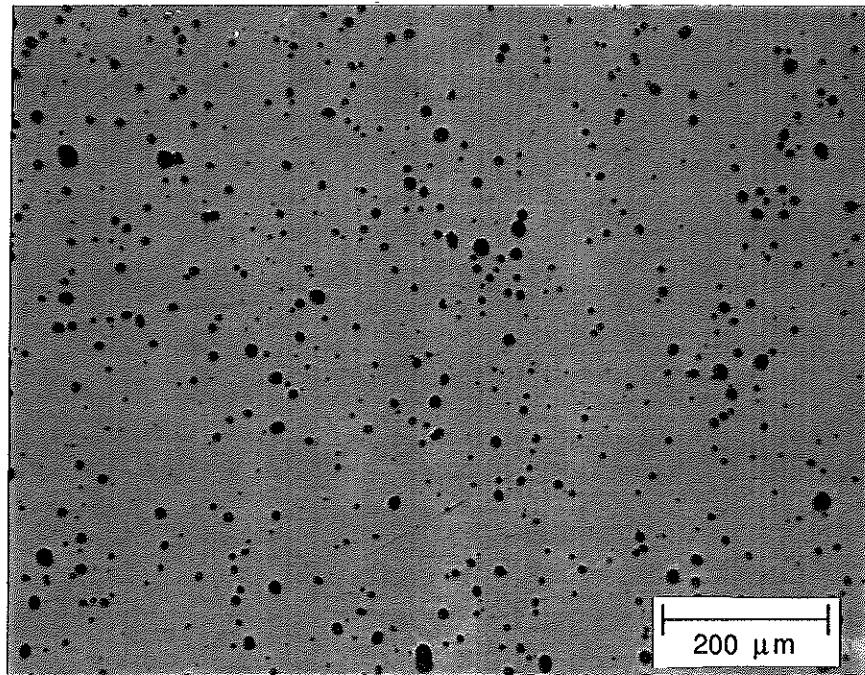


Figure 1: Optical micrograph of UNS C36000 free-cutting brass annealed at 850°C for 2 hours. Polished only.

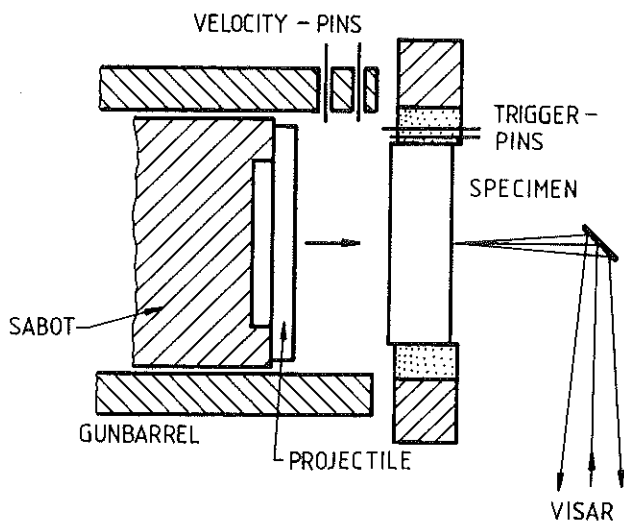


Figure 2: Schematic showing planar plate impact configuration.

specimens were annealed.

EXPERIMENTS

Plate Impact Experiments

The dynamic properties of the brass samples including the spallation behaviour has been investigated by means of

the planar plate impact technique in combination with a laser velocity interferometer VISAR [Barker, 1972] and soft sample recovery techniques (Figure 2).

The plane parallel brass plates of 50 mm diameter and 8 mm thickness have been mounted in a precisely adjustable sample holder. They have been impacted by projectile plates of 58 mm diameter and 3 mm thickness, accelerated to impact velocities of $78 \text{ m/s} < v_{\text{imp}} < 175 \text{ m/s}$ by means of a compressed air gun. Impact velocities have been measured using self-shorting triggerpins inside the gun barrel and near the target surface.

The sabot technique has been used to provide planar impact. The angular deviation from exact planar impact has been determined separately to be less than 1 mrad. The sabot contains a void behind the central part of the projectile plate to provide a free rear projectile surface.

The impact of the projectile plate on to the target front surface generates pressure waves propagating into both plates. These pressure waves are reflected at the rear free surfaces of both the target and the projectile and propagate back into the material as pressure release waves. The superposition of these release waves inside the target plate causes spallation, if the generated tensile stress exceeds the dynamic material tensile strength.

All waves reaching the target rear surface cause changes of the surface velocity. The velocity of the target rear surface has been recorded using the VISAR. The interference data are digitized and stored with a time resolution of two ns by means of a Tektronics DSA602 transient recorder and converted to a velocity time history

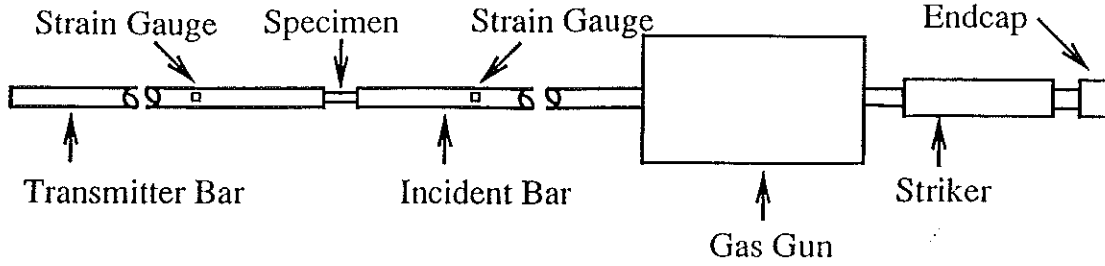


Figure 3: Schematic showing TSHB configuration. Striker cylinder is fired from gas gun and impacts end cap to generate tensile stress wave in incident bar.

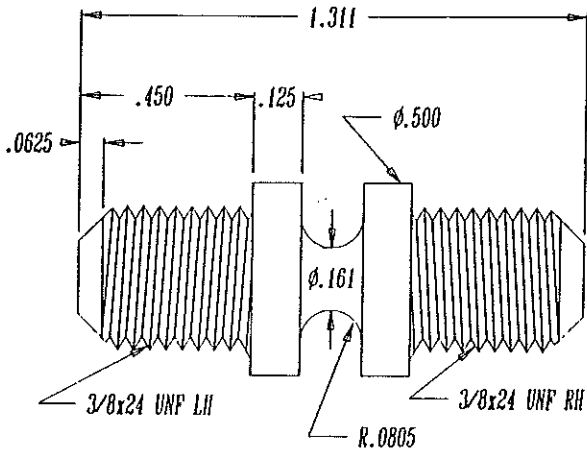


Figure 4: TSHB specimen with $R_{spec}/R_{notch} = 1.0$

using a computer program.

From the velocity time profiles the dynamic properties have been derived. From the velocity caused by the elastic precursor, u_{HEL} , the Hugoniot elastic limit, σ_{HEL} , has been calculated using

$$\sigma_{HEL} = \rho c_l u_{HEL} / 2 \quad (1)$$

The spall strength has been calculated using

$$\sigma_{sp} = \rho c_l \Delta u_{sp} / 2 \quad (2)$$

with ρ the material density, c_l the longitudinal sound speed and the velocity decrease due to spallation, Δu_{sp} .

All samples have been softly recovered for post loading microscopic and metallographic examination.

Tensile Split Hopkinson Bar Experiments

The configuration of the TSHB apparatus used in this work is shown schematically in Figure 3. The incident and transmitter bars are high strength steel with 15.9 mm diameter and lengths of 2.04 m and 1.9 m, respectively. The striker is a hollow cylinder, running concentrically along the incident bar, with linear mass equal to that of the bars and length equal to 406 mm. A tensile stress wave is generated in the incident bar by propelling the striker from the gas gun to impact with the incident bar end cap.

Notched or grooved tensile specimens are used as shown in Figure 4. The effect of the notch radius is (i) to focus deformation within the notch and (ii) to elevate the triaxiality at the specimen centre. Two specimen geometries were considered, one with a ratio of specimen minimum radius to notch radius, R_{spec}/R_{notch} , of 1.0 and the other with a ratio of 1.29 (not shown). Using this specimen design, striker impact velocities up to 20 m/s were used to produce gauge length strain rates of the order of 1000 s^{-1} and strain rates within the notch of 2000 s^{-1} .

NUMERICAL MODEL

The constitutive model employed is based on Gurson's [1975] model for porous continuum plastic materials as modified by Tvergaard and Needleman [1984]. Central to this model is the use of the Gurson yield function to determine the macroscopic stresses, Σ_{ij} , required to initiate or sustain plastic flow within a plastically dilating porous solid:

$$\phi = \left(\frac{\Sigma_{eq}}{\bar{\sigma}} \right)^2 + 2f^* q_1 \cosh \left(q_2 \frac{3\Sigma_{hyd}}{2\bar{\sigma}} \right) - 1 - q_3 f^{*2} = 0 \quad (3)$$

in which Σ_{eq} is the equivalent stress, defined by $\Sigma_{eq}^2 = 3/2 \Sigma'_{ij} \Sigma'_{ij}$, with Σ'_{ij} being the deviatoric components of Σ_{ij} , Σ_{hyd} is the hydrostatic component of stress, given by $\Sigma_{hyd} = 1/3 \Sigma_{kk}$, and $\bar{\sigma}$ is the matrix flow stress. The coefficients q_1 , q_2 and q_3 are "calibration" coefficients introduced by Tvergaard [1981] to better represent the effects of porosity in plastically deforming materials. The values adopted were $q_1 = 1.25$, $q_2 = 0.95$ and $q_3 = q_1^2$, given by Worswick and Pick [1990].

f^* is initially equal to the void volume fraction, f , but is modified to account for the onset of void coalescence according to the following function proposed by Tvergaard and Needleman [1984]:

$$f^* = \begin{cases} f & \text{if } f \leq f_c \\ f_c + \frac{f_u - f_c}{f_f - f_c} (f - f_c) & \text{if } f \geq f_c \end{cases} \quad (4)$$

Following Tvergaard and Needleman [1984], f_c is the critical

value of porosity at which void coalescence commences. To simulate the effect of void coalescence and the resultant loss of material strength, void growth is accelerated once the porosity exceeds this level according to Eq. (4). Coalescence is assumed to be complete once f reaches a final critical value, f_p and the material strength vanishes according to Eqs. (3) and (4) with $f_u^* = 1/q_1$.

Using Eq. (3) as a flow potential, one can derive constitutive equations relating the macroscopic stress and strain rates;

$$\dot{\Sigma}_{ij} = C_{ijkl} \dot{\epsilon}_{kl}^{\text{ps}}, \quad (5)$$

the details of which are given by Gurson [1975]. The components of strain $\dot{\epsilon}_{kl}^{\text{ps}}$, refer to the macroscopic strains rather than the detailed distribution near individual voids.

The rate of increase in porosity will be due to the growth of existing voids and the nucleation of new voids,

$$\dot{f} = \dot{f}_{\text{growth}} + \dot{f}_{\text{nucleation}} \quad (6)$$

The growth of existing voids is given by

$$\dot{f}_{\text{growth}} = (1 - f) \dot{\epsilon}_{kk}^{\text{ps}}, \quad (7)$$

since the matrix material is assumed to be incompressible and $\dot{\epsilon}_{kk}^{\text{ps}}$, the hydrostatic component of plastic strain rate, is due purely to void expansion.

Void nucleation is modelled as plastic strain-controlled. It is assumed that voids nucleate at second phase particles and that there will be a statistical variation in the nucleation strain for individual particles. Assuming that the nucleation strain for the total population of particles follows a normal distribution, one can use the following equation adopted by Gurson [1975]:

$$\dot{f}_{\text{nucleation}} = A h \dot{\epsilon}^p \quad (8)$$

where

$$A = \frac{1}{h} \frac{f_N}{S_N \sqrt{2\pi}} \exp \left[-\frac{1}{2} \left(\frac{\epsilon^p - \epsilon_N}{S_N} \right)^2 \right] \quad (9)$$

The term f_N represents the volume fraction of void nucleating particles while ϵ_N and S_N are the average and standard deviation of the strains at which the particles nucleate voids, respectively. In free cutting brass, the globular lead phase would constitute the void nucleating particles. The parameter ϵ^p is the effective plastic strain in the matrix and h is the slope of the material flow stress versus plastic strain curve. Based on work by Worswick [1991a], values of $f_N = 0.025$, $\epsilon_N = 0.13$ and $S_N = 0.05$ were adopted.

Equations (3) through (9) combine to describe a constitutive model for the evolution of porosity during plastic deformation and the reduction in material loading-carrying capacity due to porosity, referred to as constitutive softening. These constitutive equations have been implemented within

LS-DYNA2D. Details of this implementation and the numerical integration scheme are given by Worswick [1993].

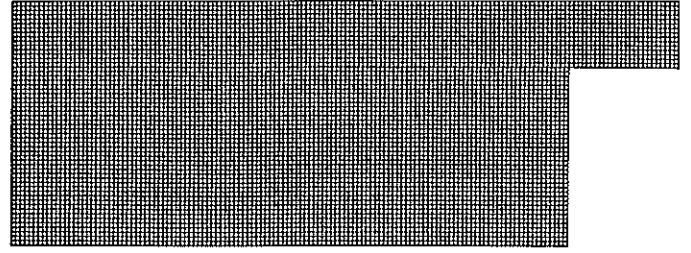


Figure 5(a): Finite element mesh used to model the plate impact experiments.

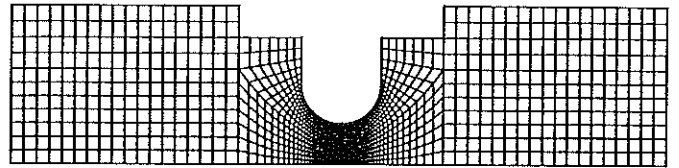


Figure 5(b): Finite element mesh used to model the TSHB experiments.

Finite Element Models

Figures 5 plots the finite element meshes used to model the plate impact and TSHB specimens. Both models are axisymmetric. For the plate impact, the flyer plate was assigned an initial velocity equal to that in the experiments. Contact interfaces known as slide lines were used to enforce the intermittent contact condition between the flyer and target plates.

The model of the TSHB did not consider the entire apparatus. Instead, velocity-time histories were specified for the nodes at the ends of the short section that were consistent with those experienced during the experiments.

RESULTS

Mechanical Parameters

Tables 1 and 2 summarize the test conditions and various measured mechanical parameters from the plate impact and TSHB experiments, respectively. In the impact tests, spallation did not occur for impact velocities below 86 m/s but did occur above 127 m/s. Additional experiments are planned to determine the threshold velocity to cause spallation. The spall strength, determined from the free surface velocities, was in the range 800 - 1000 MPa and appears to decrease with impact velocity. The dynamic strength of the lower velocity specimens that did not spall was also much higher than the spall strength. This behaviour was interesting and possibly related to the nature of damage accumulation at the different impact velocities.

Table 2 summarizes the strain rates and measured ductilities from the TSHB experiments. Shown are results

for specimens which failed on the first incident wave loading. A number of specimens, not reported in Table 2, were tested at lower rates but fractured during subsequent reflections of the incident pulse as determined from the strain

Table 1: Plate Impact Results

Plate No.	Input Velocity (m/s)	HEL (MPa)	Spall Strength (MPa)	Spallation
1	175	170	821	Yes
2	86	222	1210	No
3	78	222	1150	No
4	127	-	1000	Yes
5	134	-	-	Yes

Table 2: TSHB Results

Specimen Geometry (R_{spec}/R_{notch})	Gauge Strain	Failure Strain
1.0	970	0.57
1.0	1100	0.58
1.0	1195	0.53
1.0	1210	0.54
1.0	1430	0.53
1.29	1000	0.54
1.29	1050	0.53
1.29	1110	0.52
1.29	1110	0.55
1.29	1130	0.55
1.29	1195	0.48

gauge signals. There was a slight decrease in ductility with increased notch severity as expected. The ductilities reported here for dynamic loading were also greater than those reported by Worswick and Pick [1991a] for quasi-static loading. For example, they report a ductility of 0.39 for $R_{spec}/R_{notch} = 1.0$ compared to a range 0.53 - 0.58 in Table 1. This increase in ductility with dynamic loading suggests that inertia contributes to stabilize the plastic flow field and delays the onset of void coalescence.

Effect of Annealing

The effect of the annealing process on the mechanical response and ductility was examined by testing a number of specimens with $R_{spec}/R_{notch} = 1.29$ in the as-received condition. These specimens exhibited a higher initial yield strength and lower strain hardening than the annealed material. The lead particle populations were also significantly different since the lead diffuses and agglomerates during annealing to form fewer, larger particles. These two factors promoted lower ductilities in the non-annealed specimens with failure strains in the range 0.4 - 0.5.

Metallography

The higher numbers of particles in the as-received brass and associated smaller nearest-neighbour distance resulted in a markedly different fracture surface appearance. Figure 6 serves to compare the fracture surfaces in non-annealed and annealed specimens. There is a much smaller dimple size for the non-annealed specimens since the lead particles are more closely spaced. The annealed material also exhibits two distinct dimple sizes; the larger dimples formed at lead particles and regions of smaller dimples (arrow) are thought to have formed late in the coalescence process within ligaments located between widely-spaced particles.

The as-received material often displayed secondary fractures below the main fracture surface as shown in Figure 7. Linkage of voids appears to have occurred within a shear band to form a crack. This secondary crack and the primary fracture must have formed almost simultaneously. The determination as to which crack propagates to form the final fracture will depend upon the availability of voids ahead of each crack tip to support continued crack propagation. Such secondary fractures were not observed in the annealed brass due to its higher work hardening and larger particle spacing.

Finite Element Predictions

Figures 8 and 9 show finite element predictions for the 86 m/s and 175 m/s plate impacts. Plotted in Figure 8 are predicted contours of porosity for the lower impact velocity which shows the development of a well-defined damage layer roughly 3 mm from the rear or free surface of the target plate. Preliminary quantitative metallographic measurements have confirmed the existence of this damage layer and work-in-progress will address detailed comparisons between predicted and measured porosities.

Figure 9 shows the predicted finite element mesh after impact at 175 m/s. Formation of a spall layer is predicted through void coalescence within the elements located along the damage layer according to Eq. (4). Spallation was also predicted to occur for the 127 and 134 m/s impact velocities, in agreement with the experiments.

Figure 10 plots free surface velocity measurements and predictions for the plate impact experiments. In general, the agreement between the predictions and measured values is quite good. For example, the measured decrease in free surface velocity associated with formation of the spall layer is roughly 45 m/s. The decrease in the corresponding model prediction is approximately 40 m/s. These velocities correspond to measured and predicted spall strengths of 821 and 730 MPa, respectively. This level of agreement is encouraging since the predicted spall strength is based on the yield surface limitation of stress and on the void coalescence criterion.

DISCUSSION

Detailed measurements of porosity are underway to determine void growth rates and local conditions at void coalescence within the plate impact and TSHB specimens.

Concern exists, however, that the predicted rates of void growth are too high as noted by Worswick and Pick [1992] based on measurements from recovered Taylor cylinder specimens. There is also concern over the appropriateness

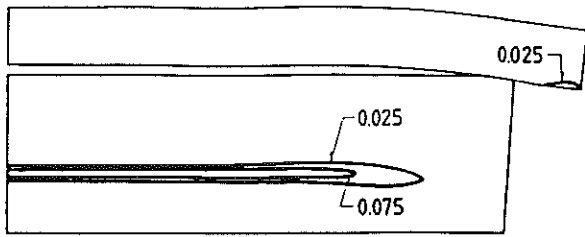


Figure 8: Contours of void volume fraction predicted for a plate impact of 86 m/s.

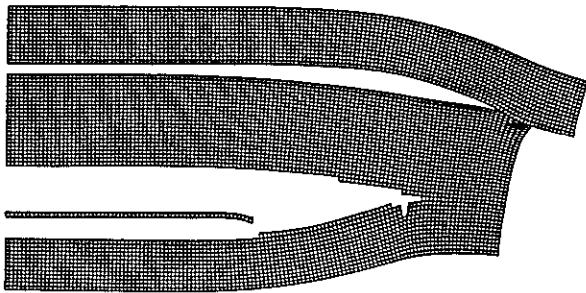


Figure 9: Deformed finite element mesh showing spallation after a plate impact of 175 m/s.

of the void coalescence criterion (Eq. 4) adopted here. The values for $f_c = 0.15$ and $f_f = 0.25$ are thought to be too large since void coalescence likely occurs within this material at porosity levels of 0.06 - 0.08. These uncertainties and the sensitivity of the spall predictions to the various model parameters are being addressed in current work.

In spite of these concerns, the model has been shown to capture the qualitative behaviour of the material rather well. It is concluded that Gurson-based constitutive models can be useful in engineering design and optimization of structures subject to impact loading.

ACKNOWLEDGEMENTS

Financial support for this work was provided by the Natural Science and Engineering Research Council of Canada. The authors thank Ms. Christie Egbert for her skilful preparation of this manuscript.

REFERENCES

- BARKER L.M., HOLLENBACH R.E. 1972 - *Laser Interferometer for Measuring High Velocities of any Reflecting Surface* - J. Appl. Phys., Vol. 43, p. 4669.
 CURRAN D.R., SEAMAN L., SCHOCKEY D.A. 1987 - *Dynamic Failure of Solids*, Phys. Rep., Vol. 147, pp. 253-388.
 GURSON A.L. 1975 - *Plastic Flow and Fracture of Ductile Materials Incorporating Void Nucleation, Growth and Interaction*, Ph.D. Thesis, Brown University.

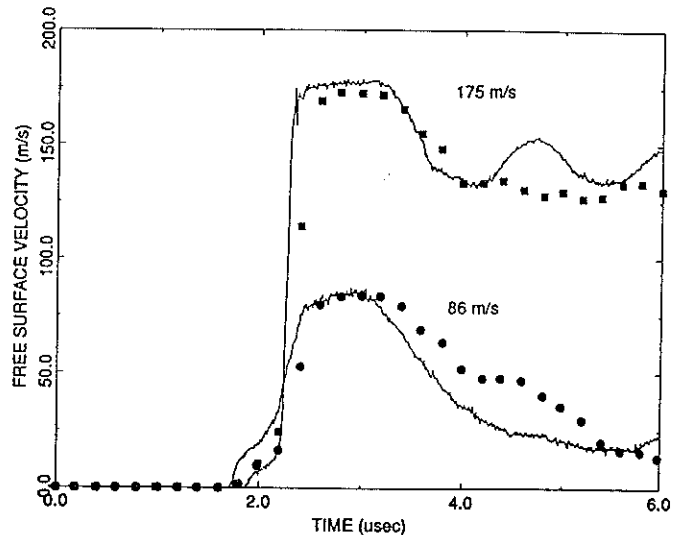


Figure 10: Free surface velocities from the plate impact experiments. (Lines - experiment, symbols - finite element)

HALLQUIST J.O. 1988 - *User's Manual for DYNA2D - An Explicit Two-Dimensional Hydrodynamic Finite Element Code with Interactive Rezoning and Graphical Display*, LLNL UCID - 18756, Rev. 3.

TANG N.Y., NIESSEN P., PICK R.J., WORSWICK M.J. 1991 - *An Investigation of Shock-Induced Damage in Oxygen-free High Conductivity Copper*, Mat. Science & Engineering, A131, pp. 153-160.

TVERGAARD V. 1981 - *Influence of Voids on Shear Band Instabilities Under Plane Strain Conditions*, Int. J. Frac., Vol. 17, pp 389-407.

TVERGAARD V., NEEDLEMAN A. 1984 - *Analysis of the Cup Cone Fracture in a Round Tensile Bar*, Acta Met., Vol. 32, pp. 157-169.

WORSWICK M.J., PICK R.J. 1990 - *Void Growth and Constitutive Softening in a Periodically Voided Solid*, J.Mech. Phys. Solids, Vol. 38, pp. 601-625.

WORSWICK M.J., QIANG N., NIESSEN P., PICK R.J. 1990 - *Microstructure and Fracture During High-Rate Forming of Iron and Tantalum*, proc. EXPOMET 90, ed. Meyers, Murr, Standhammer, University of California, San Diego.

WORSWICK M.J., PICK R.J. 1991a - *Void Growth in Plastically-Deformed Free-Cutting Brass*, J.Appl. Mech., Vol. 58, pp. 631-638.

WORSWICK M.J., WONG B., PICK R.J. 1991b - *Void Growth During High Velocity Impact*, J. de Physique IV, Vol. 1, pp. C3-605-612.

WORSWICK M.J., PICK R.J. 1992 - *Void Growth and Coalescence during High Velocity Impact*, submitted to Mech. Mat.

WORSWICK M.J. 1993 - *Ductile Fracture During High Strain Rate Deformation*, Manuscript in preparation.

NOMENCLATURE

A	- void nucleation constant	1/MPa
C_{ijkl}	- constitutive moduli	MPa
c_l	- longitudinal wave velocity	m/s
f	- void volume fraction	unitless
f^*	- void volume fraction corrected for coalescence	unitless
f_c	- critical value of porosity to initiate void coalescence	unitless
f_f	- porosity at which final fracture occurs	unitless
\dot{f}_{growth}	- growth rate of existing voids	unitless
f_N	- volume fraction of void nucleating particles	unitless
$\dot{f}_{nucleation}$	- void growth due to void nucleation	unitless
f_u^*	- $1/q_1$	unitless
h	- slope of uniaxial stress versus effective plastic strain curve	MPa
q_1, q_2, q_3	- yield function coefficient	unitless
u_{HEL}	- Hugoniot elastic limit (particle velocity)	m/s
R_{spec}	- specimen minimum radius	mm
R_{notch}	- radius of notch or groove	mm
S_N	- standard deviation of particle nucleation strains	unitless
Δu_{sp}	- spall velocity	m/s
V_{imp}	- plate impact velocity	m/s
ϵ_{ij}^{∞}	- macroscopic total strain tensor	unitless
$\epsilon_{ij}^{p\infty}$	- macroscopic plastic strain tensor	unitless
ϵ_N	- average particle nucleation strain	unitless
ϵ^p	- effective plastic strain	unitless
ρ	- density	kg/m ³
ϕ	- yield function	unitless
$\bar{\sigma}$	- matrix flow stress	MPa
σ_{HEL}	- Hugoniot elastic limit	MPa
σ_{sp}	- spall strength	MPa
Σ_{ij}	- macroscopic stress tensor	MPa
Σ_{eq}	- macroscopic equivalent stress	MPa
Σ_{hyd}	- macroscopic hydrostatic stress	MPa

ON DYNAMIC ANALYSIS OF HYBRID (STEEL-CONCRETE) STRUCTURES SUBJECTED TO EXPLOSION

K.Cichocki*, G.Maier and U. Perego

Department of Structural Engineering, - Politecnico of Milan, P.zza L. da Vinci, 32 - 20133 Milan (Italy)

ABSTRACT

This communication is intended to outline the results of a research project concerning structural and material modelling and analysis strategies for the assessment of the residual deformations due to impulsive loading (primarily underwater explosions) in steel and hybrid (concrete-steel) structures.

The proposed topical list is as follows:

- a) Constitutive features of steel and concrete in the present, high strain-rate context are pointed out and merits and drawbacks of few material models are comparatively assessed. Open questions concerning description of material behaviour like the definition of ductility limits for multiaxial stress states and mesh dependence of softening branches are addressed and critically discussed.
- b) With reference to an explosion hitting a submerged thin cylindrical shell, peculiar aspects of elastic-plastic, explicit dynamic finite element analyses, with special reference to load and geometry modelling, are highlighted.

The computational experience achieved leads to an assessment of diverse procedures from the cost-effectiveness and accuracy standpoints for the specific engineering situation considered.

MICROSTRUCTURAL EVOLUTION INDUCED BY AN EXPLOSIVE LOADING

L. Paillé, M. Gerland

Laboratoire de Mécanique et Physique des Matériaux, URA CNRS 863, ENSMA, 86960 Futuroscope, France

H.N. Presles

Laboratoire d'Energétique et Détonique, URA CNRS 193, ENSMA, 86960 Futuroscope, France

ABSTRACT

Two materials, a pure copper and an austenitic stainless steel have been treated by means of primary explosives whose effects have been characterized by microhardness measurements and transmission electron microscopy. In all cases, an important hardening is observed with a maximum located at or near the surface and a profuse twinning whose density decreases when depth increases, after a maximum located close to the treated surface. In some cases, a microrecrystallization is observed at the surface due to thermal effects generated by detonation gases. Although the induced pressure by the explosive treatment is markedly lower than the critical twinning pressure according to the literature, numerous twins and even α' embryos in the stainless steel have been observed as a consequence of multiaxial deformation.

INTRODUCTION

The idea of using shock waves to treat the surface of materials is not new since treatment with secondary explosives or laser induced shock waves have been performed for several years. These techniques induce an important hardening in the material, but the surface quality after treatment is generally very poor. However, we have shown that using a primary explosive which produces relatively low pressures in comparison with those obtained by secondary explosives or by laser induced shock waves, a marked surface and subsurface hardening can be achieved, preserving a good surface quality /Gerland 1991a, 1992, 1993a, Dufour 1991/. In this case, the primary explosive is deposited in thin layer on the surface to be treated and the detonation of the explosive substance is initiated by a laser pulse at the periphery of the area to be treated ; the detonation then spreads over the whole surface. In this kind of treatment, the two important parameters are the maximum pressure induced in the material and the pulse duration /Murr 1981, Wright 1981/. In this study, these two parameters have been varied by acting on the composition of the explosive mixture and

on the explosive layer thickness and we have studied the dependence of these parameters on the microstructure of two materials : an austenitic stainless steel and a pure copper.

EXPERIMENTAL PROCEDURE

Materials

The first studied material was a polycrystalline pure copper after an annealing of 3 hours at 460°C under a vacuum of 5×10^{-4} Pa. The mean grain diameter was then about 25 μm . The second material was an austenitic stainless steel (f.c.c. structure) type AISI 316L (AFNOR Z3 CND17-12) whose composition is given in Table I, and it was used after heat treating for 1 hour at 1050°C in vacuum (about 5×10^{-4} Pa) and water cooling. The mean grain size was about 50 μm .

All the samples used for this study were first polished before the thermal treatment and polished again up to 1 μm diamond to remove the oxide layer.

Surface treatment technique

The explosive substance used for surface treatment was prepared in one of the authors' laboratory (URA CNRS 193) by mixing a primary explosive and a liquid inert binder. The explosive substance was applied like a paint with a brush on the whole surface chosen to be treated. Different thicknesses of the explosive layer varying from 0.3 mm up to 1.2 mm have been tested. The pulse duration of the explosion is estimated to 1 μs for the thinnest layer and to 2 μs to the thickest one /Presles 1990/. To modify the pressure level at the material surface, two explosive compositions were performed. The first one, described above, composed of Pb-N₆ and nitrocellulose gives a maximum pressure of about 1 GPa /Presles 1990/. The second composition was obtained by adding 40 % of octogene to the previous one. With the second composition, the maximum pressure reaches 4 GPa.

Table I Chemical composition (wt %) of the stainless steel

Element	C	Mn	Si	S	P	Ni	Cr	Mo	Cu	B	N	Co	As
Amount (wt %)	0.022	1.69	0.31	0.002	0.023	11.90	17.45	2.25	0.110	0.009	0.069	0.190	0.004

Characterization of the effects induced by the treatment

The effects induced in the materials by the surface treatment were investigated by microhardness measurements with a load of 10 g for the copper samples and with a load of 25 g for the stainless steel samples. In the two cases, microhardness profile measurements were made in two different ways : on a section normal to the treated surface, or on the surface and parallel planes by removing layers by mechanical polishing.

Then thin foils were taken from the treated layers and observations were made at different depths by transmission electron microscopy at 100 kV or 200 kV.

RESULTS

Microhardness profiles

The microhardness profiles obtained by the two different methods are very similar for the two materials. Therefore only one type obtained on a normal section will be given. Every point of the curves corresponds to the average value of about 25 measurements of microhardness.

Copper. The evolution of the microhardness as a function of depth is given in Figure 1 for the first composition of explosive ($P = 1$ GPa) and for the explosive thicknesses of 0.3 mm and 0.6 mm. Figure 1 shows that for copper, the maximum of hardening induced by treatment for both thicknesses of explosive is reached at the sample surface ; for the 0.6 mm explosive thickness, the surface hardening is more than 100 %. The hardness decreases from the surface, first quickly then more slowly after 100 μm ; however even at 400 μm in depth it still remains higher than in the untreated material.

Stainless steel. The evolution of the microhardness as a function of depth for the stainless steel is given in Fig. 2 for the first composition of explosive ($P = 1$ GPa) and for explosive thicknesses of 0.5 mm, 0.8 mm and 1.2 mm. Figure 2 shows that for stainless steel the maximum of hardening induced by the treatment is obtained under the surface at a depth of about 20 μm . Although the hardness at the surface is already important, it still increases significantly in depth over the following 20 μm , then, as for copper, the microhardness decreases quickly during about 100 μm , then more slowly up to 400 μm for an explosive thickness of 0.5 mm and several millimetres for the explosive thickness of 1.2 mm. The dependence of the pressure level is shown in Fig. 3 for the explosive thickness of 0.5 mm. The higher pressure (4 GPa) induces a more important hardening on a deeper distance from the treated surface, since the hardening reaches 800 μm instead 400 μm for the 1 GPa pressure. The profile is however similar to the

one obtained for the lower pressure except around 20 μm in depth where a slight minimum occurs in the middle of the highest microhardness values.

Microstructural study by Transmission Electron Microscopy

Microstructural studies by TEM were performed on samples at different depths beneath the treated surface. The thinning method allows an estimation of the depth at which the TEM observations are performed better than 5 μm . The process used to realize thin foils is the well-known double jet technique ; however, to obtain thin areas at the surface, a plastic film is put on the surface so that only the rear face of the foil is thinned. To obtain thin areas at a depth different of that of the foil faces or the mean depth, one face is protected during a part of the thinning process by the plastic film which is withdrawn before the final hole.

Copper. The microstructural observations on copper have been performed only after the treatment with the lower pressure 1 GPa but for three explosive thicknesses : 0.3 mm, 0.6 mm, 1 mm. In the three cases, at the surface and up to a depth not exceeding 5 μm , it appears a localized and heterogeneous development of a micrograin structure with a mean diameter of about 50 nm (Fig. 4). At a depth of about 10 μm , the microstructure is characterized by a relatively homogeneous twinning (Fig. 5a-b) whose density slightly increases with the explosive thickness. The twin density progressively decreases when depth increases up to disappear at a depth which depends on the explosive thickness : about 50 μm for the 0.3 mm thickness, 80 μm for 0.6 mm and 120 μm for 1 mm. Beneath the twin layer, a dislocation structure in cells whose density decreases when depth increases, appears with some residual twins.

Stainless steel. For the lower pressure (1 GPa), and for an explosive thickness of 0.5 mm, the microstructure of the stainless steel is characterized, at the surface, by a twinning whose density is not very high in 65 % of the grains and only by dislocations distributed into walls aligned along usual glide directions inside the other grains. At 20 μm in depth, the proportion of grains with twins is markedly higher since it reaches 93 % (Table II). At a depth of 45 μm , the proportion of twinned grains decreases (only 71 %) and the mean twin density inside a grain is lower (Fig. 6). However some rare traces of α' -phase embryos (body centred cubic structure) have been observed at twin crossings. The twinned area ends a bit after 70 μm since, at this depth, a low twin density was observed in 25 % of the grains, 75 % of the grains having a microstructure only composed of dislocations.

For the higher pressure (4 GPa), the microstructure is composed, on the most part of the surface, by a

Table II Residual microstructure as a function of the depth.

Depth (μm)	Surface	20	45	70	100	230
Treatment						
1 GPa	35 % D 50 % 1 TS 15 % 2 TS —	7 % D 33 % 1 TS 47 % 2 TS 13 % 3 TS —	29 % D 47 % 1 TS 17 % 2 TS 7 % 3 TS α' (traces)	75 % D 25 % 1 TS — —		
4 GPa	Micrograins 7 % D 45 % 1 TS 45 % 2 TS 3 % 3 TS —	— 10 % 1 TS 47 % 2 TS 43 % 3 TS α' (traces)	— 9 % D 26 % 1 TS 43 % 2 TS 22 % 3 TS α' (27 %)	— 10 % 1 TS 55 % 2 TS 35 % 3 TS α' (28 %)	— 3 % 1 TS 49 % 2 TS 48 % 3 TS α' (80 %)	— 3 % D 50 % 1 TS 38 % 2 TS 9 % 3 TS α' (8 %)

Percentages of grains including only dislocations (D), 1 twin set (1 TS), 2 twin sets (2 TS), and 3 twin sets (3 TS). Global percentage of grains (α' %) containing α' -phase embryos in addition to twins.

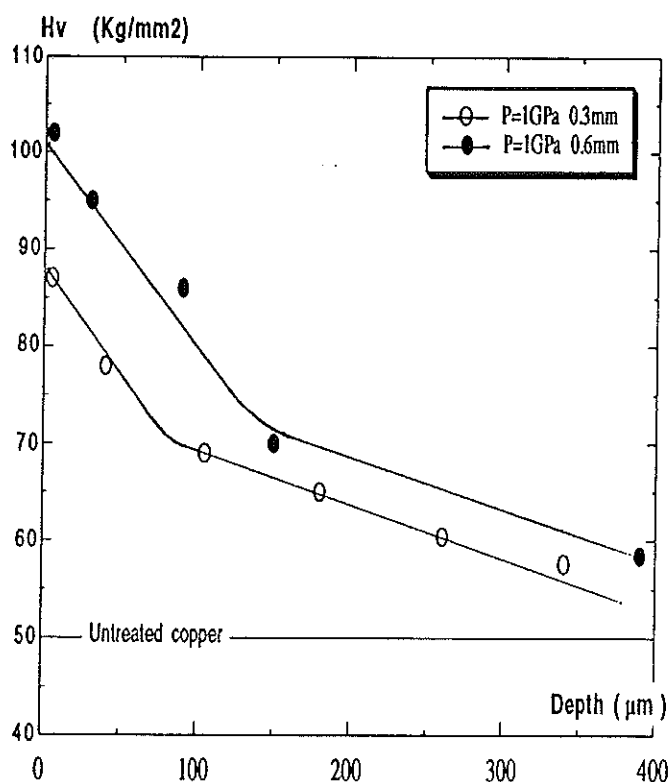


Fig. 1 - Microhardness vs depth from impacted surface in copper for two explosive thicknesses.

microrecrystallization in grains with a diameter between 10 and 50 nm (Fig. 7), on a depth of about 1 μm , and moreover very locally by a microrecrystallization of lead on a depth of about 0.1 μm . Immediately beneath the recrystallized layer, that is to say at a depth of 1 to 2 μm , a high density of thin twins was observed. From 20 μm up to 100 μm (Fig. 8-9), the twin density increases as well as the number of activated twin systems (Table II). In the same time, the α' -embryo rate formed at the twin crossings continuously increases. At a depth of 100 μm , these embryos are present in 80 % of the observed grains ; however their density remains low. At a great depth (230 μm), numerous twins are still visible, but the activated twin systems are less numerous and the

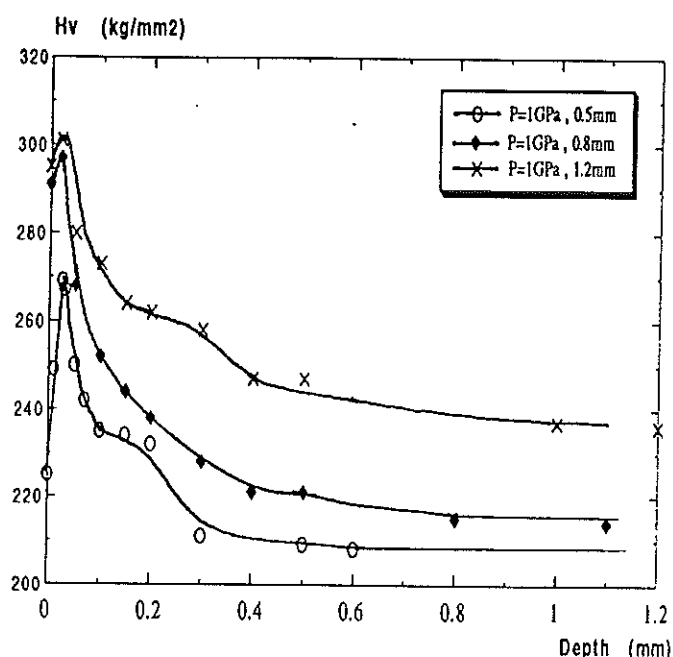


Fig. 2 - Microhardness vs depth from impacted surface in stainless steel for three explosive thicknesses.

α' -embryos rather rare (Table II). For a higher thickness of explosive layer (> 0.5 mm) and for the lower pressure ($P = 1$ GPa) the first microstructural observations seem to indicate that contrarily to what was expected, the twin density decreases when the explosive thickness increases.

DISCUSSION

The analysis of the microstructure observed by TEM allows to explain the evolution of the microhardness. In the case of the lower pressure (1 GPa), the low value of the microhardness at the surface of the stainless steel is associated with a low twin density, while the microhardness maximum, located at about 20 μm in depth corresponds to the maximum of the twin density with two or three twin systems in the major part of the grains. The progressive decrease of the microhardness in depth is related to the decrease of the twin and dislocation density. In the same way,

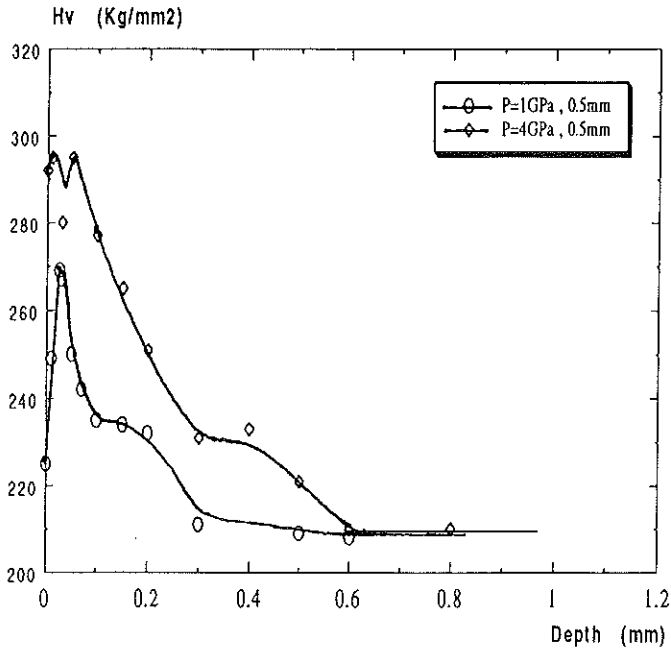


Fig. 3 - Microhardness vs depth from impacted surface in stainless steel for two pressures.

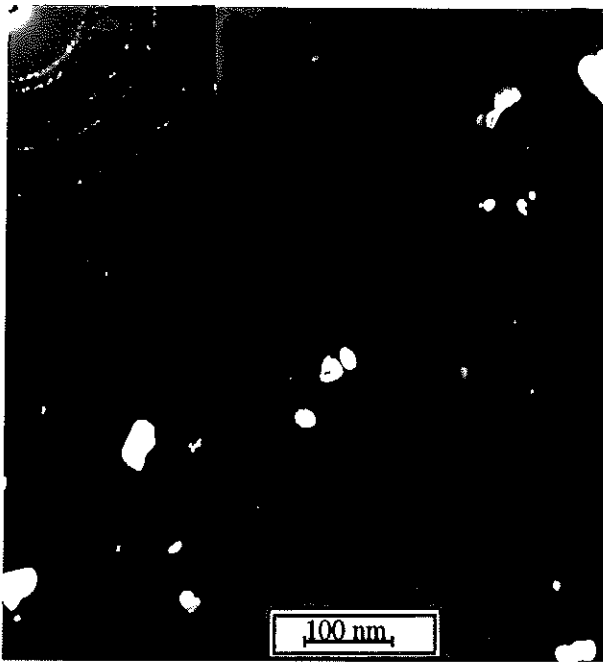


Fig. 4 - Transmission electron micrograph at the surface of a copper sample treated at 1 GPa. Dark field and selected area diffraction pattern.

in copper, the microhardness decrease is associated with the twin and dislocation density decrease when the depth increases, the intensity and the extend of the hardening being more important for high explosive thicknesses. However for the surface layer in copper, the high values of microhardness are due to the microrecrystallization in very fine grains. In the same way, for the stainless steel treated with the

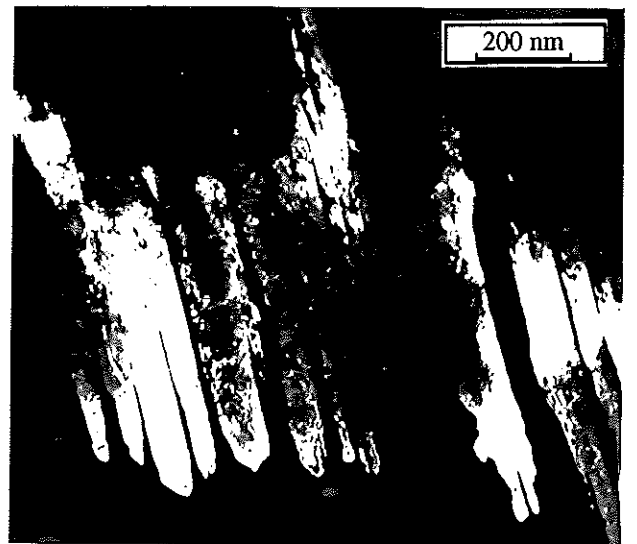
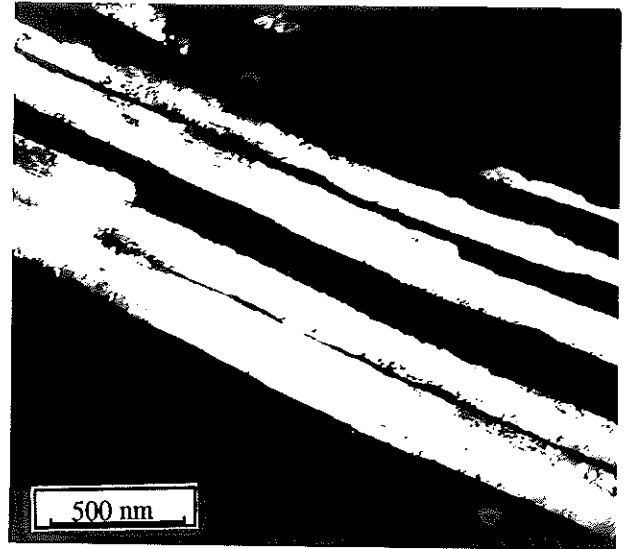


Fig. 5 - Transmission electron micrograph at a depth of 10 μm in a copper sample treated at 1 GPa. Dark field.

explosive inducing the higher pressure (4 GPa), the high values of microhardness at the surface is related to the microrecrystallization. Probably, the fact that the microhardness is not very high at the surface is due to the fact that the recrystallization is not completely uniform in this case. In both cases, copper and stainless steel, the recrystallization at the surface is associated with a thermal effect due to the high temperature of the detonation product estimated to be close to 4000 K /Presles 1990/. In the case of the stainless steel at the lower pressure, the recrystallization is not reached because the strengthening, induced by the compressive waves and the thermal effect are not sufficient. For the stainless steel treated with the explosive inducing the higher pressure, between 20 and 10 μm in depth, the higher values of microhardness than the maximum value in the case of the lower pressure are explained by the higher twin density in all this area (with



Fig. 6 - Transmission electron micrograph at a depth of 45 μm in a stainless steel sample treated at 1 GPa. Bright field.

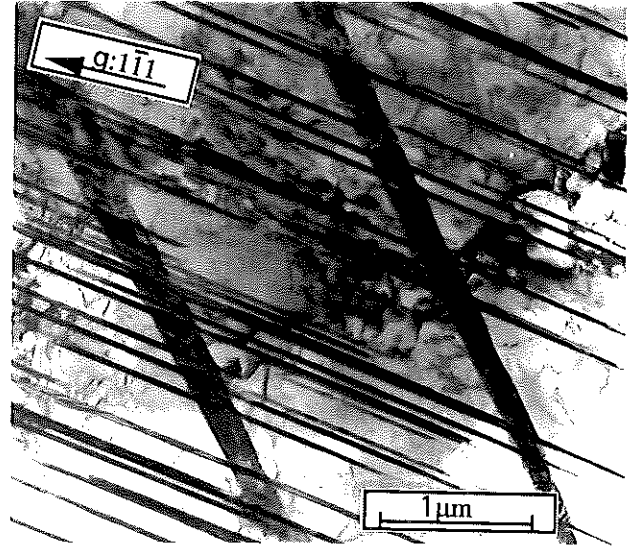


Fig. 8 - Transmission electron micrograph at a depth of 20 μm in a stainless steel sample treated at 4 GPa. Bright field.

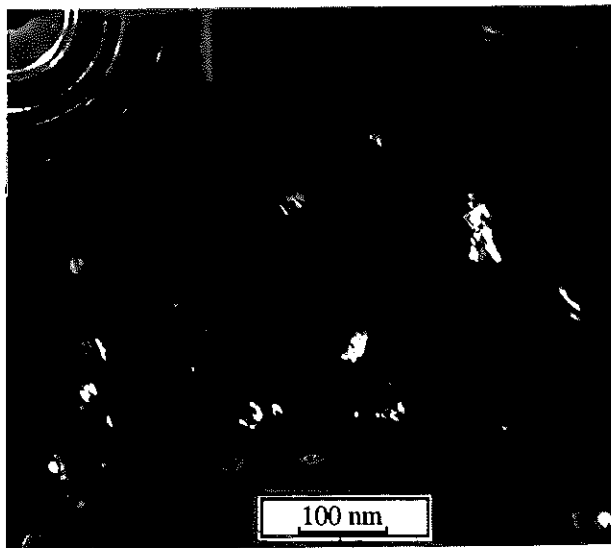


Fig. 7 - Transmission electron micrograph at the surface of a stainless steel sample treated at 4 GPa. Dark field and selected area diffraction pattern.

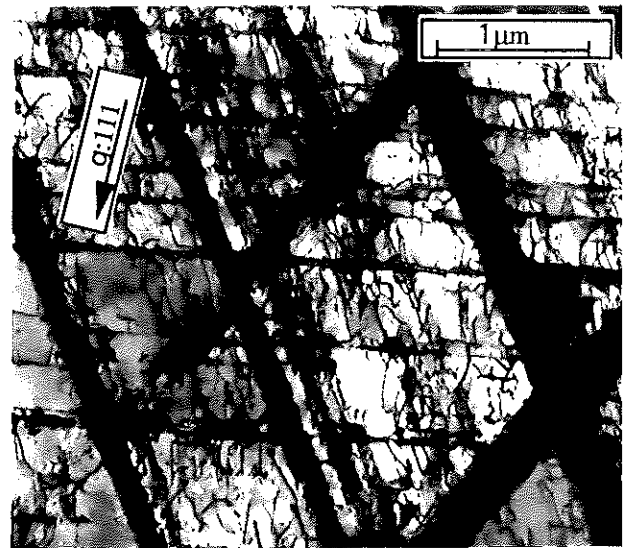


Fig. 9 - Transmission electron micrograph at a depth of 100 μm in a stainless steel treated at 4 GPa. Bright field.

$P = 4$ GPa) than at 20 μm in depth in the second case ($P = 1$ GPa). However the maximum of microhardness is located at about 50 μm in depth while the maximum of the twin density and of α' -embryos is observed at 100 μm. The high twin density still observed at 230 μm in depth (Table II) after the 4 GPa-treatment is associated with a microhardness value of 245 Hv while after the 1 GPa-treatment, the same microhardness value corresponds to a depth of 70 μm for which there are few twins superimposed to a high dislocation density.

Contrary to what has been observed in similar investigations on the stainless steel treated with laser induced

shock waves /Hallouin 1988, Gerland 1991b, 1993b/ no marked difference in the twin density with the explosive thickness was noted, as could be expected from the difference in the microhardness peak values (see Fig. 2). However the hardness increase is similar to that obtained by laser shock waves /Gerland 1992, 1993b/ in spite of very different shock characteristics in the two techniques : pulse duration and pressure of about 1 μs and 1 GPa for the explosive process against 1 ns and more than 10 GPa for the laser shock. In fact, the last remark is even surprising concerning twinning : according to the literature, the pressure threshold to obtain twins in the stainless steel (resp. copper) is about 12 GPa (resp. 20 GPa) /Murr 1987/. The response is probably that

the explosive treatment does not induce plane shock, but complex compressive waves with shear and that twins and α' -embryos are due to shearing and not to a pressure effect.

CONCLUSION

Two materials, a pure copper and an austenitic stainless steel have been treated by a primary explosive prepared according two compositions inducing a pressure level of 1 GPa or 4 GPa.

The general characteristics of the microhardness and the microstructure are similar in all cases : a strong hardening close to the surface and a profuse twinning, both decreasing when depth increases. Moreover these characteristics are more intense when the explosive thickness is more important or the pressure is higher. However for copper and at the higher pressure for the stainless steel, the maximum of microhardness is located at the surface instead of about 20 μm in depth and it is associated with a micro-recrystallization in very fine grains on a thin layer due to thermal effects. Although the induced pressure is markedly lower than the critical twinning pressure or the threshold pressure for phase transformation, as in laser induced plane shock waves, twins (in both materials) and α' -embryos (in the stainless steel) are well visible and are supposed to be due to an important shearing generated by the multiaxial compressive waves of the explosive treatment.

REFERENCES

- DUFOUR J.P., GERLAND M., MENDEZ J., PRESLES H.N., ROMAIN J.P. 1991 - Surface Modification Technologies IV, ed. by T.S. Sudarshan, D.G. Bhat, M. Jeandin, The Minerals, Metals and Materials Society, pp. 915-921.
- GERLAND M., DUFOUR J.P., PRESLES H.N., VIOLAN P., MENDEZ J. 1991a - Journ. de Phys. III, 1, 10, pp. 1647-1655.
- GERLAND M., HALLOUIN M. 1991b - Surface Modification Technologies IV, ed by T.S. Sudarshan, D.G. Bhat, M. Jeandin, The Minerals, Metals and Materials Society, pp. 895-902.
- GERLAND M., PRESLES H.N., HALLOUIN M. 1992 - Mater. Sci. Eng. A156, pp. 175-182.
- GERLAND M., PRESLES H.N., MENDEZ J., DUFOUR J.P. 1993a - Journ. Mater. Sci 28, pp. 1551-1556.
- GERLAND M., HALLOUIN M. 1993b - Journ. Mater. Sci. in the press.
- HALLOUIN M., GERLAND M., ROMAIN J.P., MARTY L., COTTET F. 1988 - Journ. Phys. C3, 19, 49, pp. 413-418.
- MURR L.E. 1987 - Materials at high strain rates, ed. T.Z. Blazinski, Els Appl. Sci., p. 17.
- MURR L.E. 1981 - Shock waves and high strain rate phenomena in metals, ed by M.A. Meyers and L.E. Murr, New-York, p. 753-777.
- PRESLES H.N. 1990 - Unpublished results.
- WRIGHT R.N., MIKKOLA D.E., LAROUCHE S. 1981, Shock waves and high strain rate phenomena in metals, ed by M.A. Meyers and L.E. Murr, New-York, p. 703-716.

SHOCK REACTION SYNTHESIS OF NiAl

J.P PONSONNAILLE , T. THOMAS

Etablissement Technique Central de l'Armement
Arcueil , France

ABSTRACT :

The purpose of this study is to determine optimal shock conditions (pressure , pulse duration) and optimal metallurgical parameters (size and composition of the powder) in order to synthesise NiAl intermetallic compound by shock-induced reaction . Experiments have been performed on mixtures of Ni and Al powders . Two powders sizes were tested . The coarse Ni and Al particles were , respectively , 32 μm and 93 μm , and small ones were 5 μm and 15 μm in diameter . NiAl and Ni₃Al stoichiometry of the mixture have been studied . NiAl pre-alloyed powder was also shock consolidated . A fully NiAl reacted sample was achieved by a liquid state reaction . For the fine powder , the reaction was complete at a shock pressure lower than for the coarser one . Thermal analysis on unreacted shocked mixture revealed that solid state reaction could be obtained on fine powders whatever the mixture stoichiometry may be .

INTRODUCTION

The conventional process to synthesise refractory materials such as ceramics , ceramic composites and intermetallic compounds are expensive in energy and time because high-temperature and long processing times are required . Two energy and cost saving techniques , named self-propagating high-temperature synthesis (S.H.S.) and Shock-induced reaction synthesis (S.R.S.) has been developed .

In the S.H.S. process , the ignition of the compressed powder mixture leads to a fully reacted product due to the exothermic heat of the chemical reaction [YI 1990 , SUBRAHMANYAM 1992] . The reaction can be initiated either by uniformly heating the green compact of the powder mixture in a furnace like in the thermal explosion mode or by locally igniting the green compact using an electric match or a laser pulse like in the combustion mode [PHILPOT 1987 , MUNIR 1988] .

A dynamic processing technique , as shock-induced reaction synthesis (S.R.S.) can also be used to initiate the reaction by shock compression of powder mixture [YU 1991, MUNIR 1992]. The passage of shock waves induced plastic deformation that leads to densify and generate intimate contacts between cleaned surfaces of powder

particles . The energy deposits in the mixture by the shock can initiate the reaction . But , the process that control shock-induced reaction synthesis which is the ignition stage are not completely understood . In high pressure processing, high temperature and high quenching rate leads to form metastable materials . High concentrations of defects can promote metastability and can lead to small crystallite sizes . This fine microstructure allows to improve the ductility at room temperature and the tensile properties at high temperature of the intermetallic compounds like nickel aluminides [ARKENS 1989 , SHANG 1991 , SONG 1992 , THADANI 1993 , HORIE 1985] .

NiAl is an attractive material for a wide range of engineering applications including advanced semiconductor, surface catalysts and high temperature applications in aerospace structures and propulsion systems. NiAl is also a popular compound for the study of scientific phenomena in ordered alloys [WANG 1988 , MIRACLE 1993] .

This paper reports the results of an investigation concerning the ignition stage of the reaction synthesis of nickel aluminides from shock consolidation . The objective of this study is to determine the optimised shock conditions in relation with metallurgical parameters such as powder granulometry and stoichiometry of the mixture .

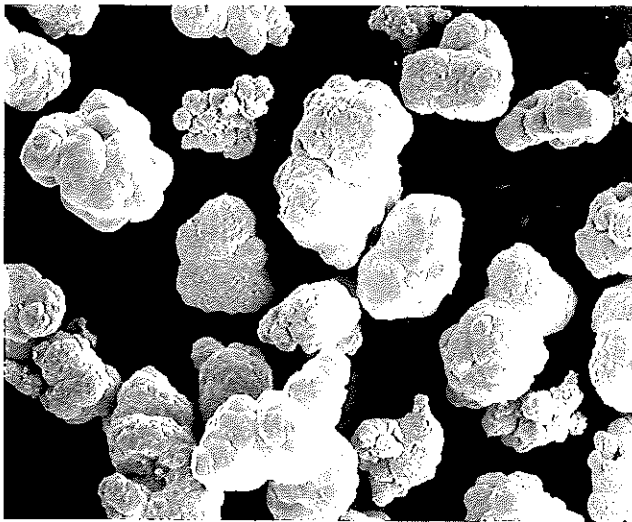
EXPERIMENTAL PROCEDURE

Experiments were conducted on mixtures of Ni and Al powders . Two sizes of powders have been tested . The coarse Ni and Al particles (figure 1(a)-(b)) were , respectively , 32 μm and 93 μm and the small (figure 1c-1d) are 5 μm and 15 μm in diameter . Three mixtures have been tested . The stoichiometry of the mixture with the coarser powders was Ni-Al 50-50 atomic percent . This mixture was name mixture(1) . The stoichiometry of the first mixture made with the smaller powders was Ni-Al , 50-50 atomic percent and the stoichiometry of the second one was Ni-Al , 75-25 atomic percent . They were respectively name mixture(2) and mixture(3) . NiAl pre-alloyed powder was also shock consolidated (figure 2) . The characteristics of the powders and the mixtures are listed in Table 1 .

	POWDERS			MIXTURES	
	Average size (μm)	Shape	Purity (%)	Mix. n ^o	Stoichiometry Ni-Al (at. %)
Ni	32	rounded	99.9	(1)	50-50
Al	93	rounded	99.97		
Ni	5	irregular	99.9	(2)	50-50
Al	15	rounded	99.97	(3)	75-25
NiAl	70	irregular	99.5		

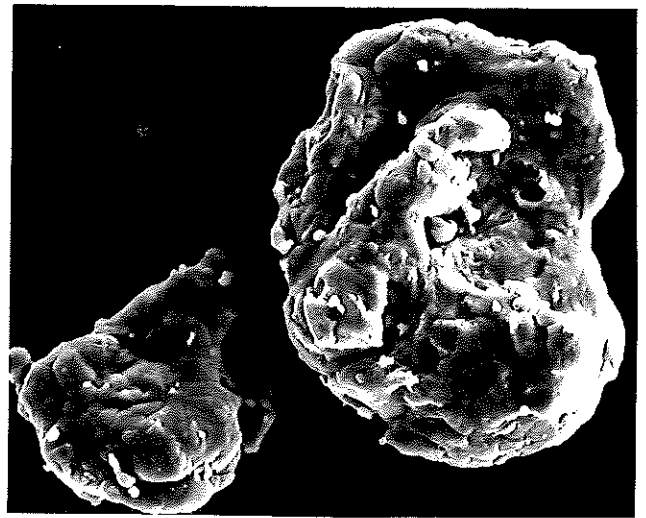
Powder source CERAC :Al (93 μm),A-1001;Al(15 μm),A-1189;Ni (32 μm),N-1023;Ni (5 μm),N-1089;NiAl,N-1024

Table 1 : Characteristics of nickel-aluminum powder mixtures



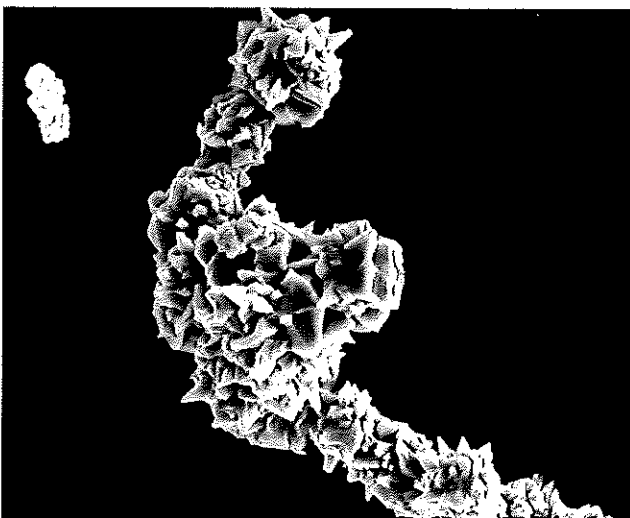
(a) Ni powder

20 μm



(b) Al powder

20 μm



(c) Ni powder

1 μm



(d) Al powder

10 μm

Figure 1 : Ni and Al powders particles

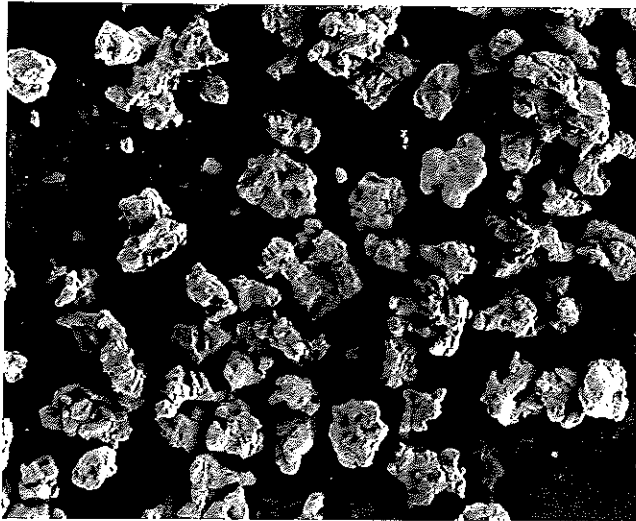


Figure 2 : NiAl pre-alloyed powder .

The dynamic compaction tests have been performed using a 90 mm explosive launcher . Explosive accelerated , a projectile supporting the flyer plate shocks a target enclosing the mixture . This set-up ensured safe recovery of materials for post-shock analysis .

The powder was packed under vacuum at 60% of the theoretical density . The set-up of the target [THOMAS 1991] is schematically represented in figure 3 .

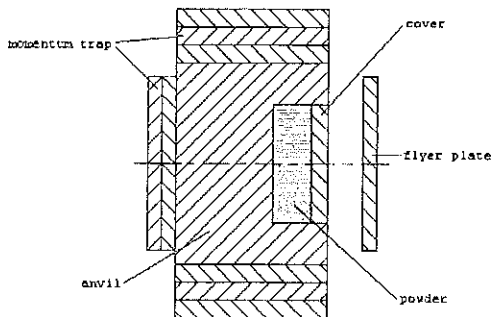


Figure 3 : plate impact recovery fixture .

Two dimensional numerical simulations (EFHYD-2D code from Engineering Systems International) were used to optimise the geometry of the target and to calculate the pressure and the pulse duration in the powder .

RESULTS:

Shock experiment parameters are listed in table 2 . The equation of state used to determine pressure and pulse duration in the mixture has been calculated from the Hugoniot theory of B.R. KRUEGER and T. VREELAND Jr.

[KRUEGER 1991] . In this model the Hugoniot of solid an porous two-component mixture is calculated using static thermodynamic properties of the components and assuming average properties for the mixture . As the present model did not take into account the reaction between the two components , the calculate Hugoniot could be valid only during the first microseconds of the shock when the reaction is still not initiate . So , this assumption could led to significant differences between the experimental and the calculated shock conditions (pressure and pulse duration)

Pressure influence :

In order to determine the pressure in the powder at which bulk chemical reaction occur , shock experiments have been conducted on mixture (1) . Pressure in the range 8 to 12GPa have been tested . The pulse duration is 1.8 μ s . Two thresholds related with pressure have been identified for chemical reaction initiation .

For pressure less than 8 GPa (test 1) , no reaction occurred (figure 4a) . The powder is well densified but some porosity could be seen . The densification is only obtained by the plastic deformation of the aluminum powder .

At a 9 GPa pressure (test 2) , some chemical reaction is observed at the contact between the Ni and the Al particles (figure 4b) . The Ni_3Al and Ni_2Al_3 intermetallic compounds are identified by X-rays diffraction and microprobe analysis . The shock propagation induced the plastic deformation of the nickel and of the aluminum powders as well as formation of interparticle jetting . The jetting phenomenon is a solid flow of particles . In this zone, evidence of reaction is observed . The observation of dendritic $NiAl_3$ and spherical porosity revealed also the melting of a part of the product during the reaction (figure 4c) . In both case , the synthesis is initiated but it did not propagate .

Shock consolidation at pressure of 12 GPa (test 3) lead to a fully reacted sample (figure 4d) . The synthesised intermetallic is NiAl . The product exhibited an eutectic microstructure which is typical of a melting and solidification process .

Pulse duration influence :

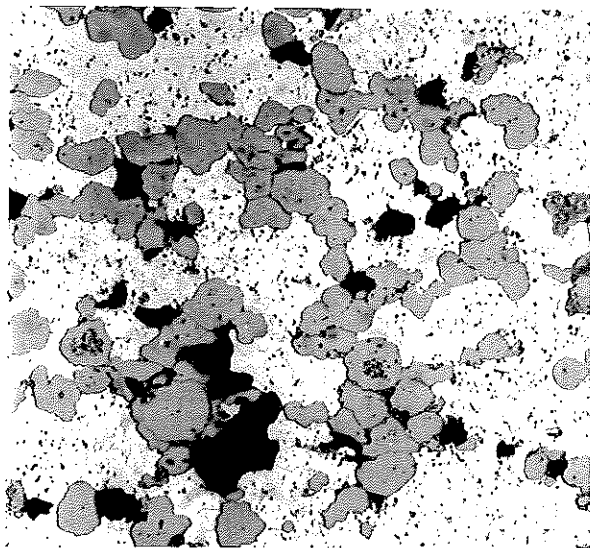
The influence of the increase of the pulse duration from 1.8 μ s (test 2) to 3.6 μ s (test 4) has been also studied . Two shock experiments have been conducted on mixture 1 at a pressure of 9GPa . In both cases , the reaction is not complete . The $NiAl_3$ and Ni_2Al_3 compounds have been synthesised and the amount of products is the same for the two tests . The particles plastic deformations are the same in both cases and are equivalent to that showed on figure 4b .

Granulometry influence :

To study the effect of particle size on the reaction propagation , shock consolidation has been performed on mixture (2) (test 5) . The shock conditions were a 9 GPa pressure level and a 1.8 μ s pulse duration . The reaction was complete (figure 5) . The grain size is smaller at the sample circumference where the quenching rate is higher .In the center , the grains are columnar . This microstructure is typical of melting and rapid solidification process .

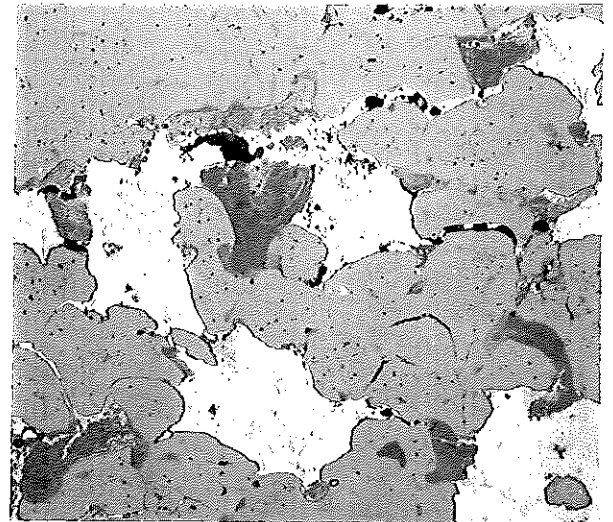
	MIXTURE	IMPACTOR			CALCULATED SHOCK CONDITIONS	
		Material	thickness (mm)	Velocity (m/s)	Pressure (GPa)	Pulse duration (μ s)
Test 1	(1)	Al	10	1200	8	1.8
Test 2	(1)	Cu	7	1000	9	1.8
Test 3	(1)	Cu	7	1190	12	1.8
Test 4	(1)	Cu	14	950	9	3.6
Test 5	(2)	Cu	7	1000	9	1.8
Test 6	(3)	Al	7	1400	9.5	1.8
Test 7	NiAl powders	Cu	7	1000	9	1.8
Test 8	(2)	Al	7	1400	8	1.8

table 2 :Experimental conditions



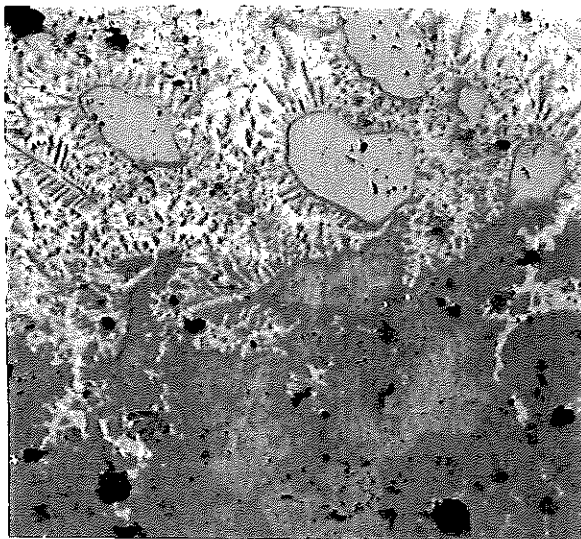
(a)

50 μ m



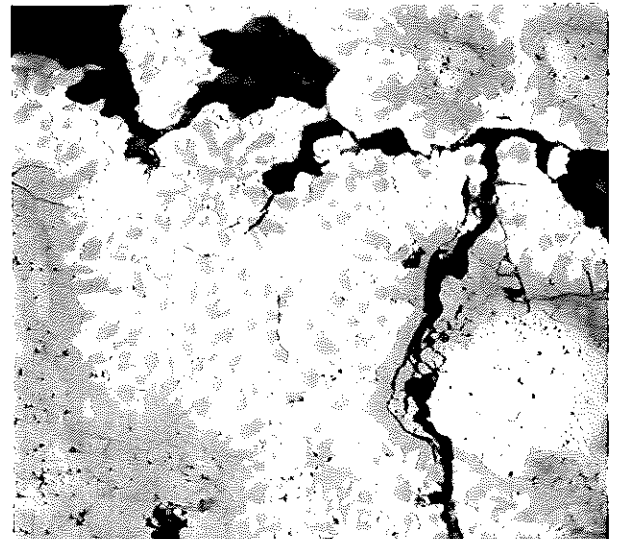
(b)

20 μ m



(c)

20 μ m



(d)

20 μ m

figure 4 : Optical micrographs showing , for mixture (1) , unreacted microstructure (a) , well densified and local reaction (b) (c) , and liquid phase reaction (d)

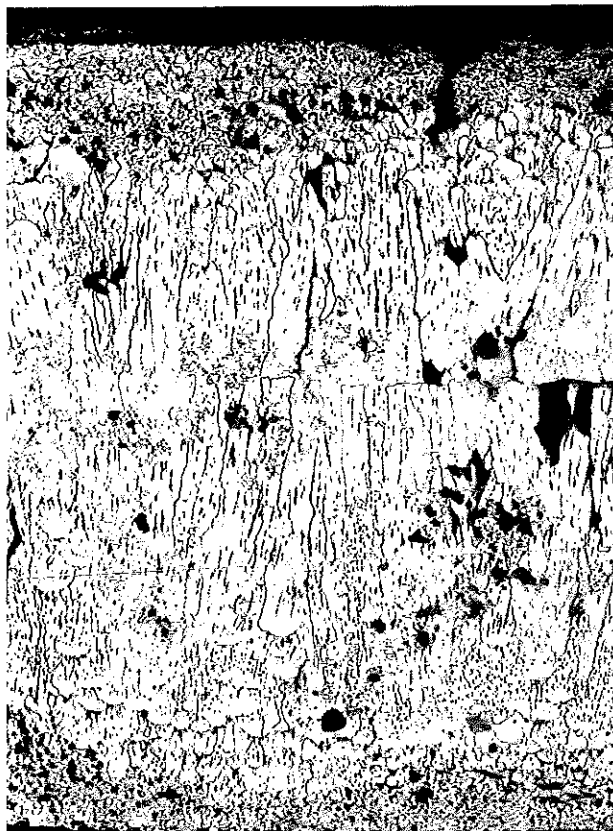


figure 5 : complete reaction in mixture (2)

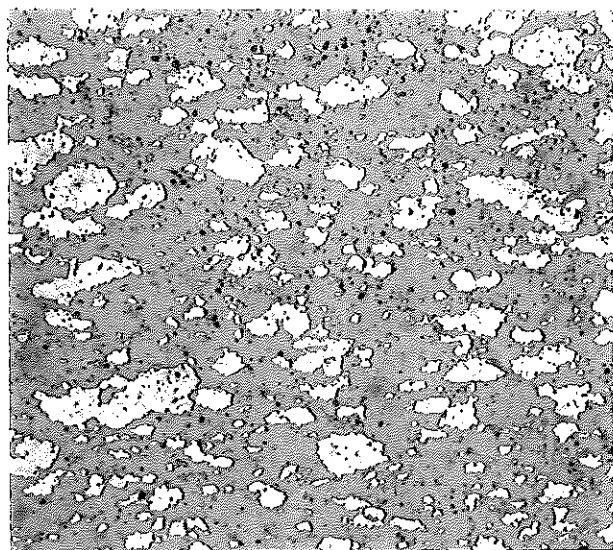


figure 6 : unreacted mixture (3)

Fully reacted samples has been obtained at 12 GPa and 9 GPa respectively for the mixture (1) (testy 3) and the mixture (2) (test 5) . So, decreasing the powder sizes from (Ni-32 μm , Al-93 μm) to (Ni-5 μm , Al-15 μm) improved the reactivity of the mixture .

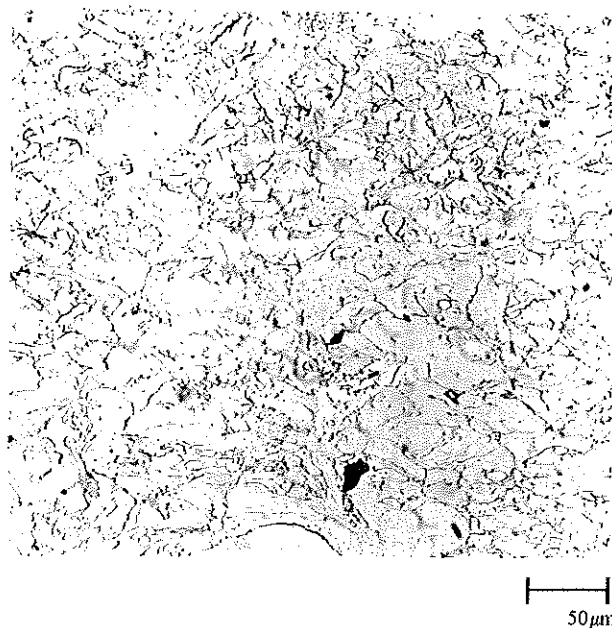


Figure 7 : Shock consolidated NiAl pre-alloyed powder

Stoichiometry influence :

In the tests 3 and 5 , a complete reaction was obtained when the heat release during shock consolidation was sufficient to melt the NiAl compound . In order to control the melting of the intermetallic compounds , fine Ni-Al powders mixed in a Ni₃Al stoichiometry (Mixture(3)) have been consolidated (test 6) . The nickel percentage has been increased in order to test if it could absorb heat excess . Shock pressure was 9.5 GPa and the pulse duration was 1.8 μs (figure 6) . No chemical reaction occurred . The plastic deformation of the nickel powder was weak . The heat generated by the shock wave was not enough to initiate the synthesis because the amount of energy absorbed by the mixture was too large .

NiAl pre-alloyed powder :

NiAl powder was also shock consolidated at 9 GPa for a pulse duration of 1.8 μs (test 7) . The figure 7 shows the important plastic deformation of the NiAl powders . Despite of its intrinsic brittleness , NiAl powder has been shock consolidated to a density close to the theoretical one .

DISCUSSION :

From the experimental results , the reaction mechanism have been studied .

In the initiation stage , the shock waves propagation densified the mixture . The energy deposition at contacts between particles can initiate the synthesis . If the shock energy is not sufficient , the reaction stops . The intermetallic identified in the reaction zone are NiAl₃ and Ni₂Al₃ .

Elsewhere the reaction propagates if the heat generated by the shock wave and the heat released by the reaction between Ni and Al powders are dissipated at a rate slower than the release rate . Then , the reaction became self-sustained and the reaction product is NiAl . The solidification microstructure of the product reveals that the reaction temperature exceeds the NiAl melting temperature ($T_{\text{melt}}=1638^{\circ}\text{C}$) .

The experimental results showed that it is necessary to increase the shock pressure to a threshold value to obtain a complete reaction. For this pressure, the shock energy have to be equal to the activation energy of the synthesis.

For the fine powders mixture, the shock energy necessary to initiate the reaction is less than for the coarser powders mixture. The threshold pressure is lower. Schwarz theory could be used to explain this phenomenon [SCHWARZ 1984]. This model predicts, for a given powder density, the regime of shock pressure and shock duration needed to fully densified products of near optimum strength. The shock energy is assumed to be deposited at interfaces between powder particles as they slide over one to each other during densification leading to partial melting. The powder is assumed to be ideal spherical particle. The model gives an upper bound to the amount of melt which had to exceed a critical thickness to achieve complete densification [WILLIAMSON 1989, RAYBOULD 1980, GOURDIN 1984]. For shock reactive sintering, experimental observations revealed that synthesis is also initiated at powder interfaces. Thus, it was possible to define a critical reaction spot size that lead to complete reaction [JOHNSON 1988]. The pressure needs for mixture (2) is lower than those need for Mixture (1) because of the more intimate contact between Ni and Al powders due to the finest granulometry. The Ni irregular shape can also improve the reactivity of mixture(2).

But that theory didn't take into account the granulometry and the stoichiometry effects on the reaction initiation when the experimental results shows that they are essential parameters.

In order to understand the dependence with granulometry and stoichiometry, reaction initiation has been studied on unreacted shock consolidated mixture. The reactive synthesis has been initiated by heating the sample in a Differential Scanning Calorimeter (DSC). This method allowed to determine the temperature at which the reaction starts.

Specimen from test 1, 6 and 8 have been heated under argon from 40°C to 720°C at 30°C/min.

For the test 1 specimen, the temperature reaction, T_r , is 642°C corresponding to an exothermic peak due to the melting of Al (figure 8a). So, the reaction is only initiated when the aluminum is melted.

On the other hand, the reaction temperature is 575 °C and 625 °C respectively for test 8 and test 6 specimen. On figure 8b-c, the exothermic peak is induced by the heat release from the synthesis of intermetallic compound. The next endothermic and exothermic peaks on this curve corresponded to the melting of Al and to the liquid phase reaction like on figure 8a.

That thermal study showed that the pressure had no effect on the reaction initiation but the reaction temperature decreases with the granulometry.

The larger amount of nickel in mixture (3) than in mixture (2) increased the reaction temperature.

CONCLUSION:

NiAl compound have been fabricated using shock reactive synthesis.

Some relationship between metallurgical parameters and shock conditions have been established.

For the Ni-Al stoichiometry mixture, a fully reacted sample has been synthesised by a liquid state reaction. The optimal shock pressure is lower for the fine powders mixture than for the coarser one.

Increasing the amount of nickel in the mixture reduced the reactivity but didn't permit to control the liquid phase formation.

In the tested range (1.8 to 3.6 μ s), the pulse duration has no effect on the amount of product synthesised.

Thermal analysis on unreacted shocked mixture showed that improve reactivity in the fine powder was due to the increase of the specific area and not to a shock pressure effect. Calorimetry measurements also revealed that solid state reaction could be obtained on fine powders mixtures whatever the mixture stoichiometry may be.

NiAl pre-alloyed powders have been shock densified close to the theoretical density despite of their intrinsic brittleness.

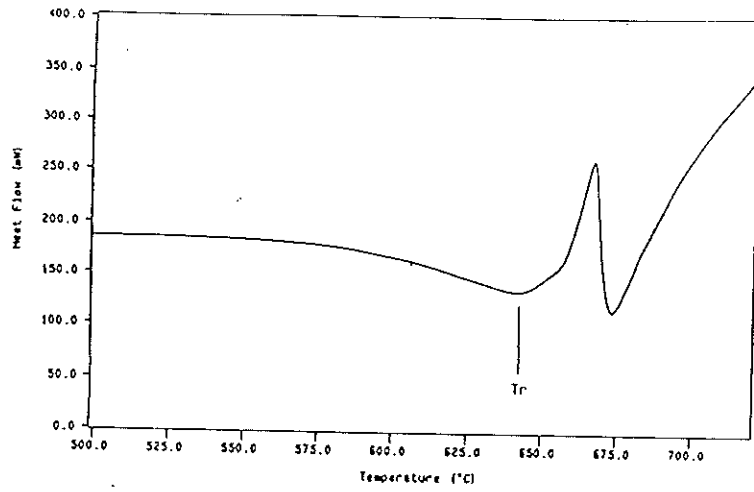
ACKNOWLEDGEMENTS :

The authors gratefully acknowledge Y. Bienvenu and J.L. Koutny of Ecole des Mines de Paris for helpful conversations and experimental support.

The authors would also like to thank P. ELIAS, J.PERRAUD and co-workers of "CEA-DAM Centre d'étude de Vaujours" and Mr CAU of the "Centre d'Etude de Gramat" for their fruitful supports for the realisation of the shock experiments.

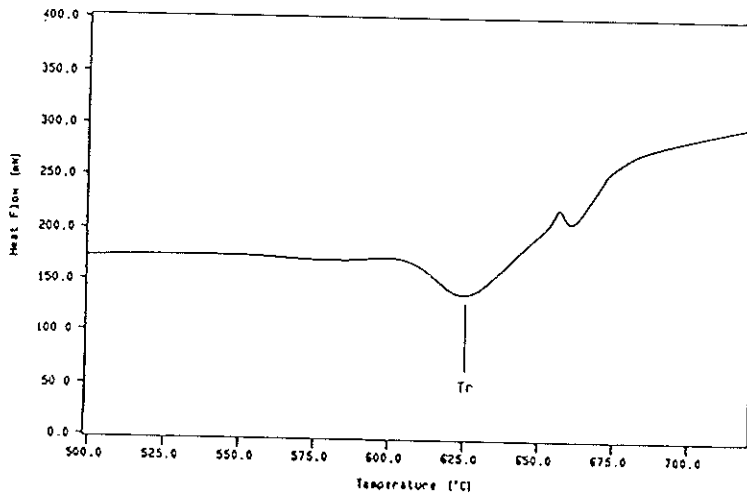
REFERENCES :

- ARKENS O., DELAEY L., DE TAVERNIER J., HUYBRECHTS B., BUEKENHOUT L., LIBOUTON J.C. 1989 - *Dynamic compaction and hot-isostatic-pressing of nickelaluminides* - Mat. Res. Soc. Symp. Proc. Vol. 133;pp. 493-498.
- GOURDIN W.H. 1983 - *Energy deposition and microstructural modification in dynamically consolidated metal powders* - J. Appl. Phys. Vol. 55(1);pp. 172-181.
- HORIE Y., GRAHAM R.A., SIMONSEN I.K. 1985 - *Synthesis of nickel aluminides under high-pressure shock loading* - Mat. Lett. Vol. 3;pp. 354-359.
- JOHNSON J.N. 1987 - *Hot-spot reaction in unsustained shocks* - Shock Waves in Condensed Matter., S.C. Schmidt, N.C. Holmes editors;pp. 527-530.
- KRUEGER B.R., VREELAND Jr. T. 1991 - *A Hugoniot theory for solid and powder mixtures* - J. Appl. Phys. Vol. 69(2);pp. 710-716.
- MIRACLE D.B. 1993 - *The physical and mechanical properties of NiAl* - Acta. metall. mater. Vol. 41(3);pp. 649-684.
- MUNIR Z.A. 1988 - *Synthesis of high temperature materials by self-propagating combustion methods* - Ceramic bulletin Vol. 67(2);pp. 342-349.
- MUNIR Z.A. 1992 - *Reaction synthesis processes:mechanisms and characteristics* - Met. Trans. Vol. 23A;pp. 7-13.
- PHILPOT K.A., MUNIR Z.A., HOLT J.B. . 1987 - *An investigation of the synthesis of nickel aluminides through gasless combustion* - J. Mater. Sci. Vol. 22;pp. 159-169.
- RAYBOULD D. 1980 - *The cold welding of powders by dynamic compaction* - Int. J. Powd. Met. & Powd. Tech. Vol. 16(1);pp. 9-19.



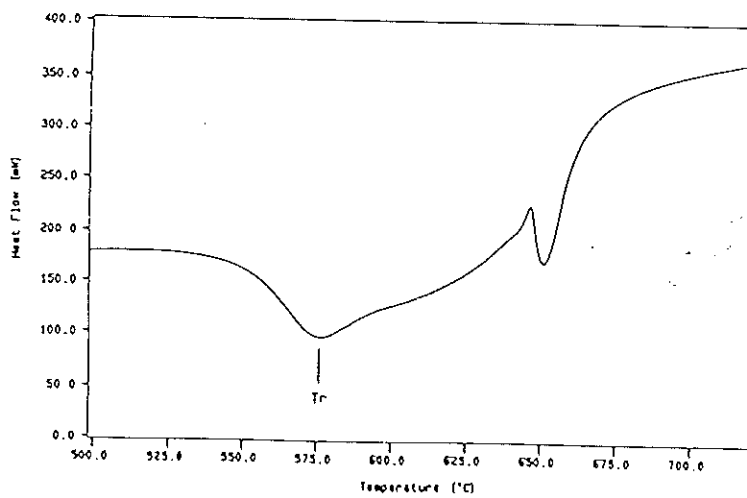
↑ endothermic
 ↓ exothermic

(a) test 1



↑ endothermic
 ↓ exothermic

(b) test 6



↑ endothermic
 ↓ exothermic

(c) test 8

Figure 8 : D.S.C. curves

- SCHWARZ R.B. , KASIRAJ P. , VREELAND Jr T. , AHRENS T.J. 1984 - *A theory for the shock-wave consolidation of powders* - Acta. metall. Vol. 32(8);pp. 1243-1252.
- SONG I. , THADHANI N.N. 1992 - *Shock-induced chemical reactions and synthesis of nickel aluminides* - Met. Trans. Vol. 23A;pp. 41-48.
- SHANG S-S , MEYERS M.A. 1991 - *Shock densification/Hot isostatic pressing of titanium aluminide* - Met. Trans. Vol. 22A;pp. 2667-2676.
- SUBRAHMANYAM J. , VIJAYAKUMAR M. 1992 - *Review Self-propagating high-temperature synthesis* - J. Mater. Sci. Vol. 27;pp. 6249-6273.
- THADHANI N.N. 1993 - *Shock-induced chemical reactions and synthesis of materials* - Progress in Materials Science Vol. 37(2);pp. 118-226.
- THOMAS T. , BENSUSSAN P. , CHARTAGNAC P. 1991 - *Consolidation dynamique de poudre de cuivre* - J. de Physique IV colloque C3 Vol. 1;pp. 131-138.
- YI H.C. , MOORE J.J. 1990 - *Review Self-propagating high-temperature (combustion) synthesis (SHS) of powder-compacted materials* - J. Mater. Sci. Vol. 25;pp. 1159-1168.
- YU L.H. MEYERS M.A. 1991 - *Shock synthesis and synthesis-assisted shock consolidation of silicides* - J. Mater. Sci. Vol. 26;pp. 601-611.
- WANG J.S.C. , DONNELLY S.G. , GODAVARTI P. , KOCH C.C. 1988 - *Microstructures and mechanical behavior of mechanically alloyed nickel aluminide* - Int. J. Powd. Met. Vol. 24(4);pp. 315-325.
- WILLIAMSON R.L. , WRIGHT R.N. 1989 - *A particle-level numerical simulation of the dynamic consolidation of a metal matrix composite material* - APS 1989, Topical conference on shock compression of condensed matter., Albuquerque, New Mexico, August 14-17, 1989, FGG-M--89144.

SHOCK-WAVE FRACTURE OF COMPOSITES WITH STRUCTURE-UNSTABLE BINDING

S.N.Kulkov, S.F.Gnusov

The study of influence phase transformation in binder of composite material on their shock fracture was evaluated experimentally.

It has been shown that if the binding phase has a structural instability (NiTi, Ni-Al, manganese steel, etc.), there was formed the ultra-fine structure with typical size of crystallites less of 100 Å having high plasticity and high capacity to hardening.

During the high-speed interaction, in the composite local stresses of tension are forming, what causes the formation of microcracking either on boundaries of binding-carbide or inside binding. It is typical that the given local zones regularly distribute in the material volume, in form of "tracks" which are distributing along the whole length of a sample. Furthermore, "tracks" are forming on the initial stage of impact front coming what tells about definite role in their formation of structure transformation in binding phase under impact wave.

The material fragmentation on the fracture surface is founded, and the presence of instability leads to amorphization of the fracture surface. The changing of the fracture mechanism is carried out: from one main crack to much cracking of plastic deformed hard particles with safety of the material compactibility and, in the end, to high value of the fracture toughness.

So, there are observed the decreasing of scale of the fracture structure level: from macrocracks to forming much microcracks in materials and its size is modulated by carbides distribution according to the size approximately normal ones.

INFLUENCE OF STRAIN RATE, BIAxIAL LOADING AND DEFORMATION MODE ON FRACTURE CRITERIA OF DUCTILE STEELS

C. Albertini, M. Montagnani, A. Rodis
Commission of the European Communities, Joint Research Centre
Institute of Safety Technology, 21020 Ispra (Varese), Italy

P. Mariotti, A. Paluffi, G. Paziienza
OTO Melara
La Spezia, Italy

ABSTRACT

For the assessment of the resistance of steel containment barriers against impulsive loading, the need to develop ductile-material fracture criteria based on a biaxial testing programme at high strain rate covering many straining directions in the principal stress plane (case of AISI 316H stainless steel) is discussed.

INTRODUCTION

Recent progress in the calculation of the dynamic loads following gas explosions (Maresca, 1991; Eibl, 1991) allows the assessment of the resistance of steel containment shells if fracture criteria of ductile steels are established, because the application of the concepts of classical fracture mechanics for fracture prediction of ductile steels is questionable because of the considerable plasticity occurring before fracture.

The method for evaluating the integrity of containment shells in the case of severe accidents commonly consists of comparing the equivalent stress and the equivalent strain in the shell, determined by F.E. code calculations, with the stress and strain limits of the fracture criteria (Fig. 1). The F.E. code calculations of the equivalent stress and strain in the shell will be correct and reliable if the dynamic loads acting on the shell are realistically known, as already mentioned, but also if the dynamic mechanical properties of the shell steel are known and are used for the calibration of the constitutive material model implemented in the F.E. code.

The constitutive material model and the ductile fracture criterion are therefore indispensable tools for the assessment of the resistance of containment shells against explosive accidents.

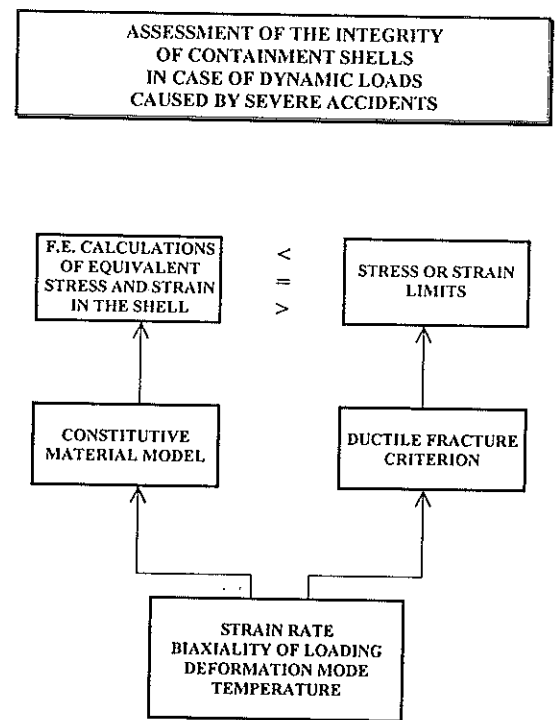


Fig. 1 - Structure evaluation method.

From the literature (Duffey, 1988; Manjoine, 1982) and from our research (Albertini, 1991; Albertini, 1990) it has been ascertained that both the constitutive material model and the ductile fracture criterion mainly depend on the following parameters:

- loading biaxiality;
- strain rate;
- deformation mode;
- size;
- temperature.

The main dynamic deformation modes leading to failure of containment shells are biaxial tension and shear in correspondence to rigid fixtures of the shell (Duffey, 1988), at strain rates ranging up to 10^3 s^{-1} .

From the literature (Duffey, 1988) and from our research (Albertini, 1991) it is found that, under dynamic biaxial tension fracture in a thin steel sheet, representing the elementary shell material unit, occurs by material separation after strain localization in one part of the thin sheet due to instabilities; the occurrence of such instabilities in the case of biaxial loading is dependent on the ratio of principal stresses σ_1/σ_2 , on the ratio of principal strains ϵ_1/ϵ_2 and on equivalent plastic strain rate (Duffey, 1988).

It is known from the literature (Hecker, 1981; Jonas, 1981) that the deformation modes in tension and shear generate at large strains different microscopic textures which give rise to different flow curves and different fracture mechanisms; therefore the fracture criteria in tension and shear of ductile steels must be determined by testing specimens reproducing the two deformation modes.

In the next sections the experimental methods for the study of fracture criteria of ductile steels for containment barriers in the case of dynamic biaxial tension and shear is discussed.

THE CRUCIFORM PLATE SPECIMEN FOR BIAxIAL TENSION DEFORMATION MODE

In the choice of the specimen geometry we must remember that:

- Biaxial tension plane stress is the deformation mode induced by explosive accidents in containment shells and that the stress-strain curves depend on the deformation mode (Hecker, 1981; Jonas, 1981).
- Strain-hardening characteristics of the stress-strain curves depend to a certain extent on the specimen geometry (Nadai, 1950).
- The instabilities giving rise to strain localization leading to fracture by material separation are also dependent on the specimen geometry (Nadai, 1950). In fact the instabilities of a plate specimen and of a tubular specimen have a completely different physical nature.

Such considerations led us to choose a cruciform plate specimen as the most appropriate to study the constitutive model and ductile fracture criterion of containment shell steels because it has the same deformation mode as and great geometrical similarity with an elementary portion of the containment shell.

Also the tubular specimen allows the creation of a biaxial tension plane stress field but the stress-strain curves and the onset of the instability will be different from those characterizing the deformation of a plane sheet; therefore the constitutive model and the ductile fracture criteria calibrated using data from specimens having a geometry different from a plate specimen will not be the most suitable to describe the deformation and fracture of the material of containment shells.

The tubular specimen allows a biaxial tension-torsion deformation mode but in this case also, as already mentioned, the equivalent flow curve obtained from torsional data does not coincide with the equivalent flow curve obtained from direct tension tests because the concept of classical plasticity theory of the unique equivalent stress-strain curve whatever the deformation mode fails at large strains (Hecker, 1981; Jonas, 1981).

These are the reasons why we chose the cruciform plate specimens, sketched in Fig. 2, where the central gauge part is subjected to independent loads along two orthogonal axes, creating a uniform state of biaxial plane stress.

In the far past (Mönch, 1963) showed by the photoelastic technique that a cruciform plate specimen of uniform thickness, subjected to biaxial tensile loading, gave a uniformly stressed area approximately equal to 2/3 of the test plate area, but with more highly stressed regions around the load connection points.

More recently (Hayhurst, 1973) solved the problem of the higher stresses at the loading points, relative to the uniformly stressed central region, by uniformly thinning the central region (gauge part) to such an extent that the uniform central stress exceeded the largest stress at the loading points.

Looking at the geometry of the cruciform specimens we observe that the loads along the two orthogonal directions (Fig. 2) are applied to the central gauge part by means of long flexible arms separated by cuts.

The function of the cuts is of key importance because they allow a uniform deformation of the central gauge part by weakening the surrounding strong frame which must deform by the same amount as the central gauge part.

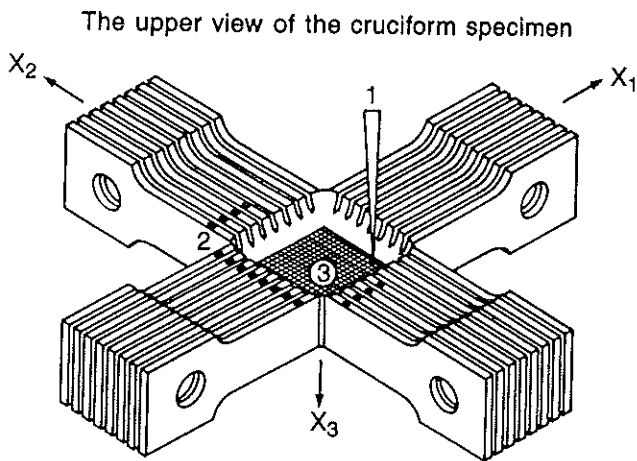
Calculations by Finite Element codes of the response of the cruciform plate specimen of Fig. 2 have been performed in biaxial static loading conditions using the ABAQUS code (Micunovic, 1988) and in static and dynamic biaxial loading conditions using the ADINA code; the results of these calculations have shown a homogeneous stress and strain distribution over the whole central gauge part.

Experiments have been performed at low and high strain rate measuring the strain distribution by filming the deformation of a fine grid of 0.5 mm pitch photoetched over the whole central gauge part; the results of this experimental analysis confirmed the calculations and allow us to affirm that the central gauge part deforms uniformly up to the beginning of necking which takes place mainly in the central zone away from the corner of the specimen (Albertini, 1989).

Therefore the conditions for a correct study of the deformability limits of the plate specimen are verified.

THE CYLINDRICAL SPECIMEN FOR DOUBLE SHEAR DEFORMATION MODE

The proposed specimen is sketched in Fig. 3. It consists of two thick hollow cylindrical parts jointed through a thin circular crown which is the gauge part of the specimen. The



MEASUREMENTS

1. Change of thickness
2. Distributed forces
3. In-plane displacements
4. Temperature
5. Strain gages

The bottom view

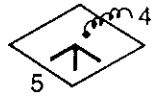


Fig. 2 - The cruciform specimen.

thin circular crown is built up by means of a slight difference between the outer diameter of the smaller cylindrical part and the inner diameter of the larger cylindrical part. Because of its resemblance the specimen has been named "bicchierino", the Italian name for a small beaker.

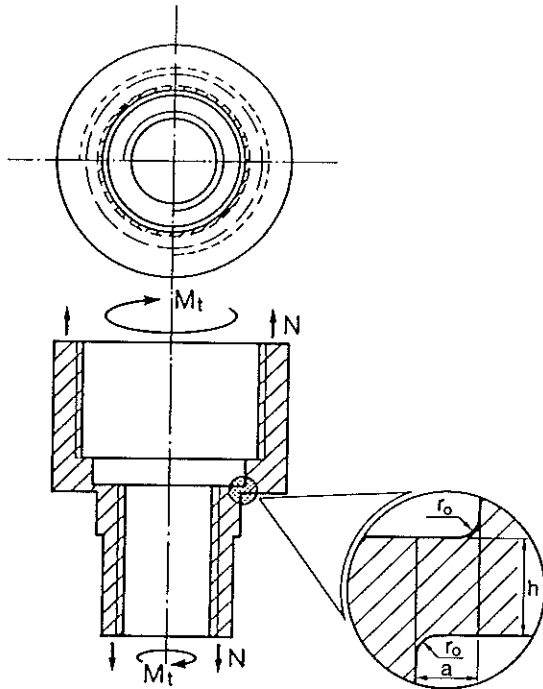


Fig. 3 - The bicchierino specimen.

The deformation mode of the gauge part is simple shear when the specimen is subjected either to axial loading or to a torque as shown in Fig. 3. The simultaneous application of

axial and torque loading to the specimen brings the gauge part to deform in a double shear mode. The longitudinal (radial) section of the gauge part is shown in Fig. 3; it consists of a rectangle of the dimensions axh , and of two appendices bounded by the radii of curvature r_0 necessary both for a gradual transition into thicker parts of the specimens, and for manufacturing reasons.

An optimization study by finite element calculation has been performed, by the last two authors of reference (Albertini, 1990a), of the dimensions of the specimen, in order to obtain a state of uniform shearing stresses in the gauge part and to minimize the other stress components. The equations of state assumed for the shape optimization of the specimen are those of linear elasticity because the elastic case has been judged to pose the most severe requirements for obtaining a homogeneous stress distribution. The optimization procedure led to the following optimal dimensions of the gauge part (Fig. 3): $a/h=0.5$ $r_0/h=0.2$. The actual specimen was constructed following the optimization conditions with a short gauge length $a=0.25$ mm, which allows homogenous stress distribution along the gauge part even when testing at very high strain rate. At the same time the gauge part has a length which contains at least ten grains of the metals under testing and has a cross section of 16 mm^2 , both parameters being sufficient to make the gauge part representative of the average mechanical response of the material to external loading.

Some tests at low strain rate were interrupted before fracture at different strain levels of the gauge part in order to observe the mode of deformation under the optical microscope. An example of such observations, corresponding to a high straining value, is provided in Fig. 4 and

demonstrates that the deformation mode is pure shear. The cross section resisting shear remains practically unchanged although the high strain value. Furthermore, the deformation is practically confined inside the gauge length.



Fig. 4 - Gauge part deformation after a shear strain 1.6 (x100).

Some numerical investigations on the "bicchierino" specimen were performed by means of NIKE 2D, a vectorized implicit finite element code for analyzing the static and dynamic response of 2-D solids developed by Lawrence Livermore National Laboratory (USA) (Albertini, 1990b).

The numerical analysis confirmed that the highly prevalent stress component in the gauge part is uniformly distributed shear and that the plastic deformation is concentrated in the restricted area of the gauge part as desired. Fig. 5 illustrates these conclusions for the case of an interrupted test with large strain. The numerical analysis showed that even at very large strains no geometrical instabilities disturb the material deformation. Good agreement was obtained by comparing the numerically obtained plastic deformations and those derived from microscopic examinations.

SIMPLE EXAMPLES OF DUCTILE-MATERIAL FRACTURE CRITERIA

The existing ductile-fracture criteria have been mainly used equating the equivalent plastic strain (or the equivalent plastic stress) to the fracture strain (or the fracture stress) determined in simple uniaxial tension, defining fracture as occurring when the effective value of strain (or stress) reaches the uniaxial fracture strain (or stress) value.

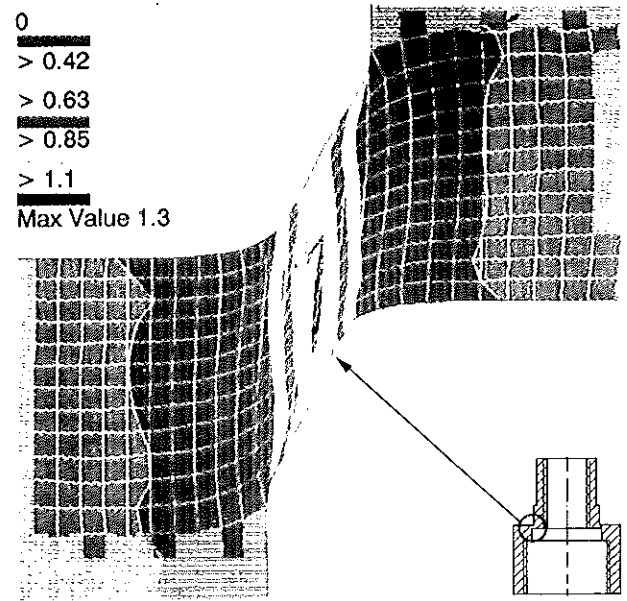


Fig. 5 - Calculated strain distribution in the gauge part at displacement of 0.395.

Flow Stress (σ_{FLOW}) Criterion Based on a Stress Limit

Fracture occurs if the equivalent (Von Mises) plastic stress in the structure ($\sigma_{\text{EQV. STRUCTURE AT FRACTURE}}$) reaches a designated value (σ_{FLOW}) which is defined as the average of the ultimate stress $\sigma_{\text{UTS UNIAXIAL}}$ and the initial yield stress $\sigma_{\text{Y UNIAXIAL}}$, both derived from the uniaxial stress-strain curve of the material at a given strain rate:

$$\sigma_{\text{EQV. STRUCTURE}} = \sigma_{\text{FLOW}} = \frac{\sigma_{\text{UTS UNIAXIAL}} + \sigma_{\text{Y UNIAXIAL}}}{2} \quad (1)$$

Criterion Based on a Strain Limit

Fracture occurs if the equivalent (Von Mises) plastic strain in the structure ($\epsilon_{\text{EQV. STRUCTURE AT FRACTURE}}$) reaches a designated strain value derived from the uniaxial stress-strain curve ($\epsilon_{\text{FRACTURE UNIAXIAL}}$) of the material at a given strain rate (Duffey, 1988).

$$\epsilon_{\text{EQV. STRUCTURE}} = \epsilon_{\text{FRACTURE UNIAXIAL}} \quad (2)$$

Criterion Based on a Strain Limit Corrected by a Triaxiality Factor

Fracture occurs if the equivalent (Von Mises) plastic strain in the structure ($\epsilon_{\text{EQV. STRUCTURE AT FRACTURE}}$) reaches a designated value of strain derived from the uniaxial stress strain curve ($\epsilon_{\text{FRACTURE UNIAXIAL}}$) of the material at a given strain rate, modified by the Davis triaxiality factor T_{DF} (Manjoine, 1982):

$$\epsilon_{\text{EQV. STRUCTURE}} = \epsilon_{\text{FRACTURE UNIAXIAL}} \cdot 2^{(1-T_{\text{DF}})} \quad (3)$$

where:

$$T_{\text{DF}} = \frac{1}{\sqrt{2}} \frac{\sigma_1 + \sigma_2 + \sigma_3}{(\sigma_1 - \sigma_2)^2 + (\sigma_2 - \sigma_3)^2 + (\sigma_3 - \sigma_1)^2}$$

$\sigma_1, \sigma_2, \sigma_3$ = principal stresses in the structure.

DEPENDENCE ON STRAINING DIRECTION IN THE PRINCIPAL STRAIN PLANE OF SOME PARAMETERS OF DUCTILE-FRACTURE CRITERIA IN THE CASE OF TENSILE DEFORMATION MODE

The dependence on straining direction in the principal strain plane of the equivalent stress-strain curve and of some ductile-fracture criteria parameters has been experimentally determined for AISI 316H austenitic stainless steel by using the cruciform specimen shown in Fig. 2 loaded by an electromechanical testing device for the test at strain rate 10^{-3} s^{-1} and by hydropneumatic biaxial testing device for the test at strain rate 6 s^{-1} .

Both testing devices were designed and constructed at the JRC-Ispra and have already been described in (Albertini, 1989).

The biaxial cruciform specimen was instrumented as shown in Fig. 2. The forces on the armfingers (applied at cylindrical holes along the x_1 and x_2 axis, respectively)

were measured outside the specimen on four elastic arms of the machine, as a function of time.

In Fig. 6 the flow curves connecting equivalent plastic strain and Mises equivalent stress are presented for both low and medium strain rates and various straining directions in the principal strain plane; for all straining directions and at both strain rates the flow curves show strain hardening and a slight strain rate hardening.

Fig. 7 shows the dependence on straining direction of the equivalent ultimate tensile strength, which is one parameter entering ductile-fracture criteria based on stress limits.

From Fig. 7 one observes that the ultimate tensile strength (U.T.S.) determined in uniaxial tension is practically coincident with that determined from equibiaxial tension, while the U.T.S. decreases by biaxial testing along straining directions intermediate between uniaxial and equibiaxial; strain rate effects on the U.T.S. are negligible.

The strain at failure, the other parameter used in ductile-fracture criteria based on strain limits, determined from uniaxial tension is practically coincident with that from equibiaxial tension (Fig. 8) while it strongly decreases by biaxial testing along straining directions intermediate between uniaxial and equibiaxial.

The same straining direction dependence of the fracture strain is observed at low (10^{-3} s^{-1}) and at medium (6 s^{-1}) strain rates (Fig. 8), while fracture strains at medium strain rate are always lower than fracture strains at low strain rate.

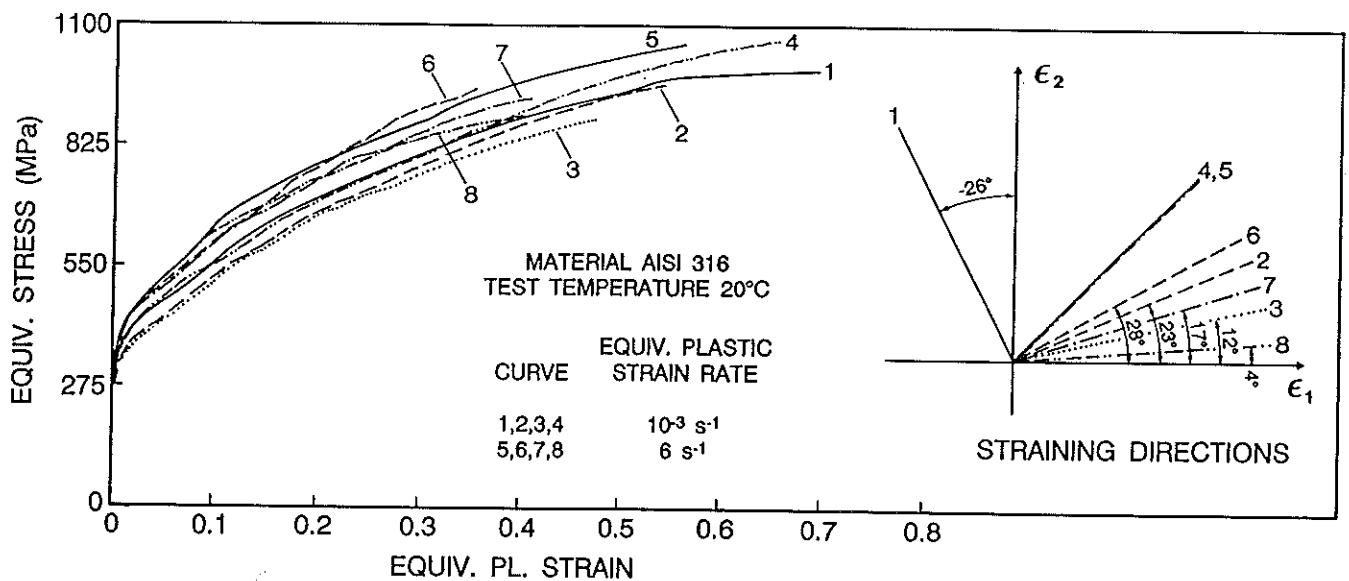


Fig. 6 - Equivalent stress-strain curves at different straining directions.

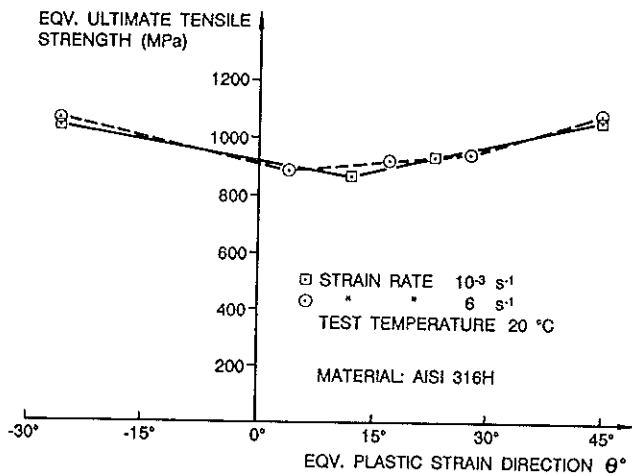


Fig. 7 - Equivalent U.T.S. versus straining direction.

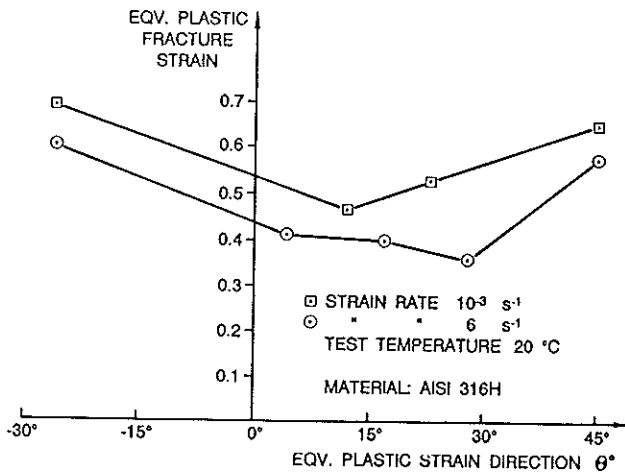


Fig. 8 - Equivalent fracture strain versus straining direction.

DEPENDENCE OF SOME PARAMETERS OF DUCTILE-FRACTURE CRITERIA IN THE CASE OF SHEAR DEFORMATION MODE

Uniaxial tensile tests were performed on AISI 316H at strain rates ranging between 10^{-3} and 10^3 s^{-1} , which were filmed during testing to characterize the necking zone.

Shear tests were performed using the special specimen of Fig. 3.

The comparison of the true stress strain curves in tension with the equivalent stress strain curves obtained from the shear test is shown in Fig. 9. In Fig. 9 the parts of the true stress strain curves in tension of AISI 316, traced with discrete points, correspond to necking and have been reconstructed following the analysis of Bridgman (Bridgman, 1952).

The equivalent stress strain curves in shear of Fig. 9 have been obtained by calculating the equivalent stress by the Von Mises model and by calculating the equivalent strain by Polakowski and Ripling (Polakowski, 1966).

From this comparison it follows that:

- The tension curves by the Bridgman analysis show strain hardening up to fracture, while the equivalent curves from the shear tests show saturation of flow stress. This phenomenon is present at each strain rate.
- As a consequence of the above phenomenon, the true flow stress at a given strain in tension and the equivalent flow stress at the same strain in shear show a modest agreement at low strain, while at large strain they strongly diverge, particularly at high strain rates.
- The fracture strain of the tension curves by the Bridgman analysis and of the equivalent curves from the shear tests are comparable.

It follows that stress and strain characteristics and therefore the stress or strain limits of ductile-fracture criteria depend on the deformation mode and that it is not possible to obtain a unique equivalent flow curve from tension and shear tests, as claimed in classical plasticity.

CONCLUSION

The criteria for stress and strain limits of ductile-fracture of containment shell steel to which the calculated equivalent stress and strain of the shell are compared, cannot be safely deduced only from uniaxial material tension tests because such stress and strain limits are dependent on the straining direction in the principal strain plane, and on the equivalent plastic strain rate.

Therefore such stress and strain limits for containment shells must be determined on the basis of a biaxial testing programme which must take into account different directions both in the principal strain plane and in the principal stress plane and different equivalent plastic strain rates.

Furthermore the stress and strain limits are dependent on the deformation mode as shown by comparing the equivalent flow curves determined in tension and shear.

Therefore in the case of shear loading, the stress and strain limits of ductile-fracture criteria must be determined on the basis of a shear testing programme because the Von Mises equivalence criterion between tension and shear stresses is not consistent at large strains both at low and high strain rates.

In fact the Von Mises equivalence criterion does not take into account the development at large strains of different microscopical textures caused by the different

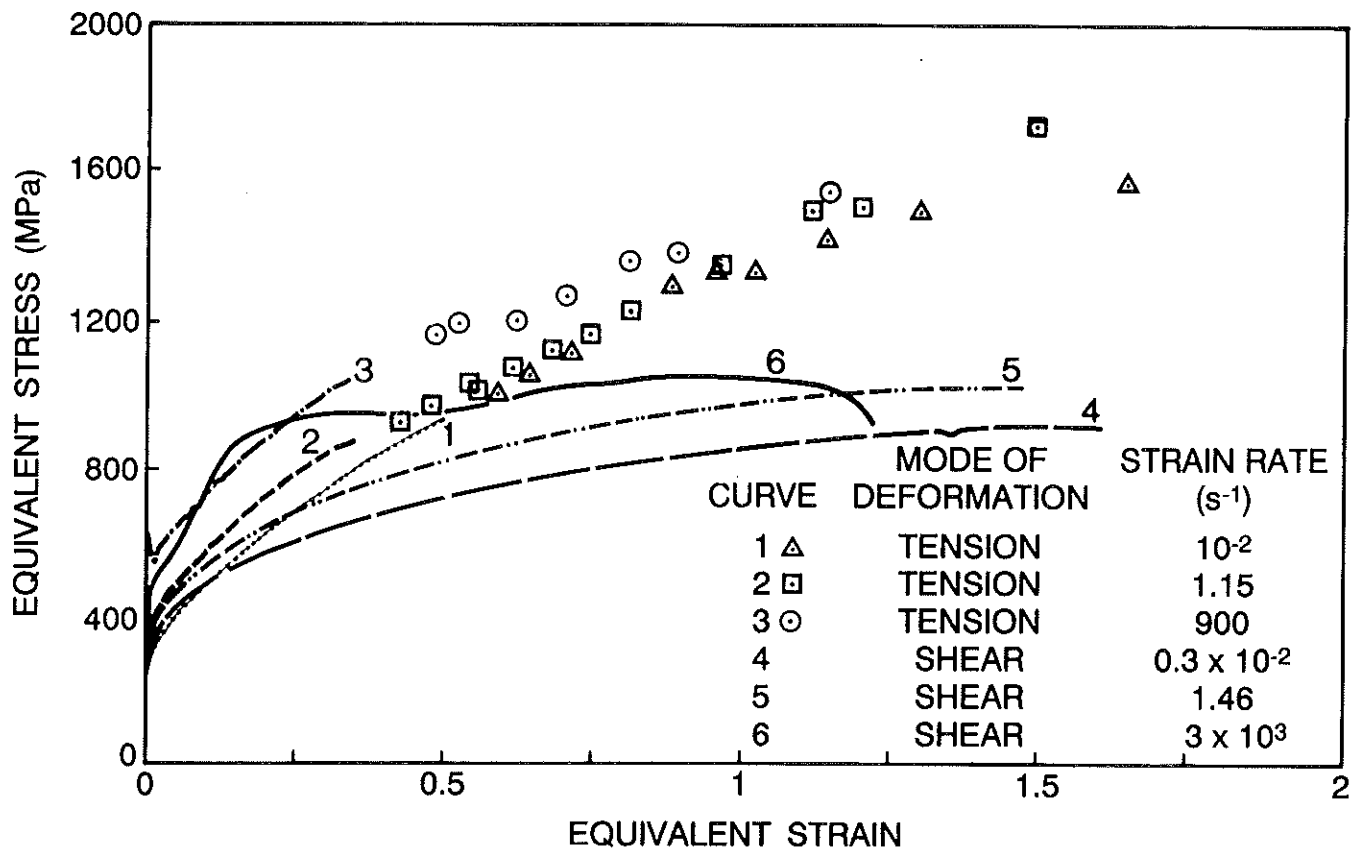


Fig. 9 - Equivalent stress-strain curves of AISI 316H in tension and shear.

straining directions, by low and high strain rates and by tension and shear deformation modes.

ACKNOWLEDGEMENTS

Thanks are due to the Members (Mr. A. Del Grande, C. Delzano, M. Murarotto, V. Pizzinato, W. Schnabel) of the Dynamic Material Properties Laboratory of JRC Ispra for the skilful performance of the experiments.

REFERENCES

- ALBERTINI C., BLERY BLIONAS E., MICUNOVIC M., MONTAGNANI M., PIZZINATO E.V. 1989 - *Biaxial Strain-Rate controlled Viscoplastic Experiments on Cruciforms Specimens of AISI 316H up to 10 s⁻¹*. Inst. Phys. Conf. Ser. No. 102, Session 4.
- ALBERTINI C., IIDA K., DEL GRANDE A., FORLANI M., PACHERA A., MONTAGNANI M. 1990 - *Residual Tensile Properties at Low and High Strain Rates of AISI 316H, Predamaged by Creep, Low Cycle Fatigue and Irradiation*. ASTM STP 1046 Vol. II, pp. 387-403.
- ALBERTINI C., MONTAGNANI M., ZICZKOWSKI M., LACZEK S. 1990a - *Optimal Design of a Bicchierino Specimen for Double Shear*, Int. Jour. of Mechanical Sciences. Vol. 32, No. 9, pp. 729-741.
- ALBERTINI C., MONTAGNANI M., PIZZINATO E.V., RODIS A., BERLENGHI S., BERRINI G., PAZIENZA G., PALUFFI A. 1990b - *Mechanical Properties in Shear at Very High Strain Rate of AISI 316 Stainless Steel and of a Pure Iron*. Proc. of the Int. Conf. on Shock-Wave and High Strain Rate Phenomena in Materials, University of California, San Diego, ISBN 0-8247-8579-7, pp. 681-691.
- ALBERTINI C., MONTAGNANI M., MICUNOVIC M. 1991 - *Viscoplastic Behaviour of AISI 316H: Multiaxial Experimental Results and Preliminary Numerical Analysis*. NED 130, pp. 205-210.
- BRIDGMAN P.W. 1952 - *Studies in Large Plastic Flow and Fracture*. Mac Graw Hill, pp. 9-37.
- DUFFEY T.A. 1988 - *Dynamic Rupture of Shells*. ISBN/ISSN 0-471-63733-5, pp. 161-192.
- EIBL J., SCHLÜTER F.H., CÜPPERS H., HENNIES H.H., KESSLER G. 1991 - *Containments for Future PWR-Reactors*. SMIRT 11th Transactions, Vol. A, pp. 57-68.
- HAYHURST D.R. 1973 - *Journal Strain Analysis*, Vol. 8, pp. 119-123.
- HECKER S.S., STOUT M.G., EASH D.T. 1981 - *Experiments on Plastic Deformation at Finite Strains*. Proc. of Workshop on "Plasticity on Metals at Finite Strains". Stanford University, pp. 162-205.
- JONAS J.J., CANOVA G.R., SHRIVASTAVA S.C., CHRISTODOULOU N. 1981 - *Sources of the Discrepancy Between the Flow Curves Determined in Torsion and Asymmetric Tension and Compression Testing*. Proc. Workshop "Plasticity of Metals at Finite Strains", Stanford University, pp. 206-229.

MANJOINE M.J. 1982. *Creep Rupture Behaviour of Weldments*. 62th AWS Annual Meeting in Cleveland Ohio, April 5-10, 1981 (Welding Research Supplement).

MARESCA G., MILELLA P.P., PINO G. 1991 - *Impulsive Load and Structural Response of a Nuclear Power Plant Steel Containment under H₂ Burning*. SMIRT 11th, Transactions, paper J11/2.

MICUNOVIC M., ALBERTINI C., MONTAGNANI M. 1988 - *Viscoplastic Material Properties at Non-Proportional Strain Histories of AISI 316H Stainless Steel*.

Int. Seminar The Inelastic Behaviour of Solids. MECAMAT, Besançon.

MÖNCH E., GALSTER D. 1963 - *British Journal Applied Physics*. Vol. 14, pp. 810-812.

NADAI A. 1950 - *Theory of Flow and Fracture of Solids*. Mac Graw Hill, Vol. 1.

POLAKOWSKI N.H., RIPLING E.J. 1966 - *Strength and Structure of Engineering Material*. Prentice - Hall Inc., Englewood Cliffs, pp. 382-383.

SIMULATION OF THE TECHNOLOGICAL ACTION ON THE MICROSTRUCTURE AND DYNAMIC PROPERTIES OF METALS

M.A. Anfyorov

Department of Engineering Science, Ufa Aviation University
Ufa, Russia

ABSTRACT

The fundamental concept of construction of modern High technologies is the integrated use of unique methods, such as laser finishing ion-beam implantation, etc.

However, the control these process is possible only with use of the computer because of a considerable multiplicity of changeable in time functional parameters. This fact define the vitality of the construction of the proposed universal mathematical apparatus, which allow to simulate as technological fields as the physical state of the metal, wich is under the action of these fields.

INTRODUCTION

At present unique technological techniques are used for the formation of special operational properties and a metal microstructure of critical jet parts. These are such techniques as laser finishing, ion-beam implantation, ductile hardening strain etc. However there is a problem because different physical phenomena are esed by these techniques. This fact leads to incompatibility of describing mathematical models and negative effect in the time of construction of integrated High technologies. These technologies include combination of unique techniques.

Beside that a technological action is accompanied by number of concurrent processes complicating the general pattern. These are such processes as adhesional interaction of tols with a workable surface layer, thermal processes accompanied by structure phase conversions etc. These processes have a different physical nature also.

All that make a monitoring of the hereditary mutual influence of technological actions in time of the formation of operational metal properties impossible.

Usually used empirical models are resided within the scope of one action and they not allow to receive the desired results.

This paper presents the approach to action modelling wich uses a common physical medium for different techniques. This medium is described on the quantum-mechanical layer.

THE NEW APPROACH

The technological action may to pursue an two aims. That is either an acquiring by the surface of the necessary configuration or the formation of requiring properties and a microstructere. The technological field is the notion concerned with a solution of the second class of problems.

The technological field is defined by a scalar characteristic function value $T(\mathbf{r})$ in the point \mathbf{r} of the geometry space covering the described workable surface layer. The technological field has the form of the vector field $\nabla T(\mathbf{r})$. This definition is accompanied by two requirements.

Firstly the function $T(\mathbf{r})$ value is one of properties of the workable material. Secondly the $T(\mathbf{r})$ function is instationary one for the time coordinate that is $\partial T(\mathbf{r})/\partial t = \text{const.}$

There is the interest to no one but some properties usually. This fact contradict the definition of the technological field on the face of it.

Therefore it is necessary to notice that a use of one a sensitive property characteristic is enough in time of the action research of the material behaviour. This proposition holds tue as other characteristics are existed in the correlation dependence with one. If it is necessary (for example the development of control models etc.) may it make use of some function $T_i(\mathbf{r})$, $i=1,2,\dots$ defining technological field. This use not breaks a correct of the employment mathematical apparatus.

In this paper the characteristic function is defined by a quantum-mechanical condition of microstrusture components of the material surface layer through the phonon levels density [1]

$$g_{\mathbf{r}}(\omega) = \sum_s \int d\mathbf{k} \delta(\omega - \omega_s(\mathbf{k})) / (2\pi)^3 \quad (1)$$

where \mathbf{k} is the wave vector of a reverse gride; ω is the normal mode frequency, s^{-1} ; s is the branch number of the normal mode; $\delta(\cdot)$ is delta-function of Dirac.

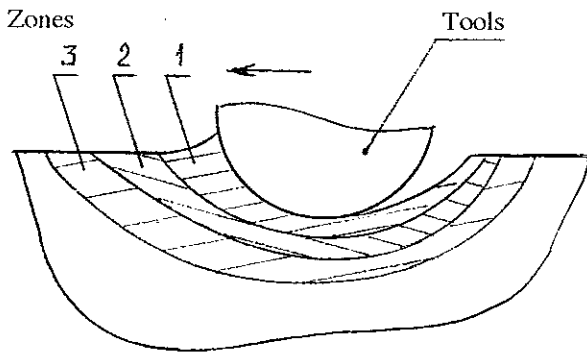


Fig.1.Example of the technological field zones.

This characteristic function is defined as

$$T(\mathbf{r}) = \int d\omega \cdot g_{\mathbf{r}}(\omega) \quad (2)$$

This representation of the characteristic function is possessed by the obvious advantage since a technological field describe a direction and severity of a variation of the internal energy and the force loads causeing to the structure modifications of a material.

The determination of the technological field demands the correspondence of the described $T(\mathbf{r})$ field with a used technological action. Adequacy of this correspondence is ensured by a calculation of empirical coefficients allowing for the phonon-defect interactions.

The crystal defects (dislocations, vacancies, grain boundary etc.) are represented by microobjects with quantization energy levels defined in the wave vector space. These objects are described by the wave vector \mathbf{k}_d of the reverse grid, by the frequency $\omega(\mathbf{k}_d)$ of the grid normal models superposition at the dissipation of phonons on the given defect, by the quasi-momentum $\mathbf{P}_d = \hbar \mathbf{k}_d$ and by the energy $E_d = \hbar \omega(\mathbf{k}_d)$.

For example in case the phonon with the wave vector \mathbf{k} and the branch number s is absorbed at single-phonon dissipation the laws of conservation of energy and quasi-momentum are expressed as

$$\begin{aligned} \hbar \cdot \omega(\mathbf{k}'_d) &= \hbar \cdot \omega_s(\mathbf{k}) + \hbar \cdot \omega(\mathbf{k}_d) \\ \hbar \cdot \mathbf{k}'_d &= \hbar \cdot \mathbf{k} + \hbar \cdot \mathbf{k}_d \end{aligned} \quad (3)$$

As phonon is released we have

$$\begin{aligned} \hbar \cdot \omega(\mathbf{k}'_d) &= \hbar \cdot \omega_s(\mathbf{k}) - \hbar \cdot \omega(\mathbf{k}_d) \\ \hbar \cdot \mathbf{k}'_d &= \hbar \cdot \mathbf{k} - \hbar \cdot \mathbf{k}_d \end{aligned} \quad (4)$$

It is known the ductile strain process is accompanied by the active movement and the interaction of crystal defects. It influences on the phonon density by force of interactions (3) and (4). As a result it permits to find the law between the technological field and the formed material properties.

It is discerned three zones describing the technological field. For example these zones are shown on the figure 1 for the ductile hardening strain.

First zone is characterized by large gradients of energies and temperatures causing to structure-phase transformations. This zone consists of two parts - active and recovering ones (are not shown by fig.1) The energy

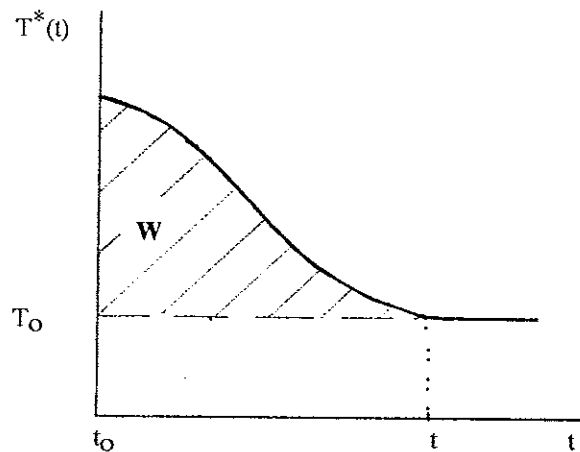


Fig.2.The explanation to the determine of the integrated characteristic W.

transformations in the active part lead to the intensive phonon radiation what characterizes this zone how a phonon source. In the recovering part of the first zone the active influx of the technological energy is ceasing that leads to a placing of the balance state of the microstructure. In just this part the required properties of a surface layer are formed.

The second zone is described by anharmonic models allowing for disturbances created by the transfer of high energy phonons from the first zone.

The therd zone is described by harmonic models allowing for small disturbances from the second zone.

In general the characteristic function for the active part of the first zone is defined by the empirical dependence

$$T(\mathbf{r}) = T_1(\mathbf{r}, I_0, \mathbf{G}, \mathbf{X}, \mathbf{L}, \mathbf{V}(\mathbf{r})) \quad (5)$$

where \mathbf{G} is the vector of parameters describing the tools configuration; \mathbf{X} is the vector of action conditions; \mathbf{L} is the vector of parameters describing travels in time of the ductile strain; $\mathbf{V}(\mathbf{r})$ is the vector of parameters allowing for the phonon scattering (the dislocation density, the dispersion of phase etc.); I_0 is the general characteristic allowing for microstructure and other properties before the action. This characteristic is determined as

$$I_0 = \int d\omega \cdot g_0(\omega) \quad (6)$$

where $g_0(\omega)$ is the phonon levels density before the action.

For the second zone the characteristic function is defined by the empirical dependence

$$T(\mathbf{r}) = T_2(\mathbf{r}, I_0, \mathbf{G}, T_{12}, \mathbf{V}(\mathbf{r})) \quad (7)$$

where T_{12} - the characteristic function value at the boundary of second and first zones.

The technological field modelling not represent of the practice interest in the third zone since new properties are not formed that.

The movement of the surface layer element through the recovering part of the first zone is accompanied by the phonon density lowering with a maximum value $T^*(t_0) = T(\mathbf{r})$ at the time moment t_0 to being settled of a value T_0 within $(t' - t_0)$ time (look fig.2).

The integral characteristic

$$W = \int_1^l dt \cdot (T^*(t) - T_0) \quad (8)$$

allow to define the main formed properties of the surface layer.

With this purpose the experimental dependences of properties from W characteristic are got for the number of materials and actions. The disclosing of the definition and use mechanism of these dependences deviate from this paper framework.

CONCLUSIONS

The proposed approach to the technological action modelling is universal one with reference to the used technological actions.

The definition of a technological field of formed material properties allows to build the function models of technological actions.

The used models allow to solve problems of a technological heredity in time of a designing of integrated technologies as the technological field description is universal one.

NOMENCLATURE

E_d =energy of the crystal defect, J;
 G =vector of parameters describing the tools configuration;
 $g_0(\omega)$ =phonon levels density before the action;
 $g_r(\omega)$ =phonon levels density in the point r ;
 l_0 =general characteristic allowing for microstructure and other properties before the action;

k =wave vector of reverse grid, m^{-1} ;
 k_d =wave vector for the crystal defect, m^{-1} ;
 L =vector of parameters describing travels in time of the ductile strain;
 P_d =quantum-momentum of the crystal defect, J·s/m;
 r =coordinate vector of the point, m;
 s =branch number of the normal mode;
 $T(r), T_j(r)$ =characteristic function in the point r ;
 T_0 =settled characteristic function value;
 $T^*(t)$ =function dependence the characteristic function from the action time;
 T_{12} =characteristic function value at the boundary of second and first zones;
 $T_1()$ =empirical model of the characteristic function for the active part of the first zone;
 $T_2()$ =empirical model of the characteristic function for the recovering part of the first zone;
 $V(r)$ =vector of parameters allowing for the phonon scattering (the dislocation density, the dispersion of phase etc.);
 W =integral characteristic allowing the formed properties;
 X =vector of action conditions;
 $\omega(k)$ =normal mode frequency, s^{-1} ;
 $\delta()$ =delta-function of Dirac.

REFERENCES

1. ASHCROFT N., MERMIN N. 1976 - Solid state physics - Holt, Rinehart and Winston, New York.

MISSILE IMPACT AGAINST METALLIC STRUCTURES

D. Aquaro

Dipartimento di Costruzioni Meccaniche e Nucleari
Universita' di Pisa -56100 Pisa (Italy)

ABSTRACT

This paper deals with a theoretic and experimental research program about the missile perforation of steel circular plates carried on at the Dipartimento di Costruzioni Meccaniche e Nucleari (DCMN) of Pisa University (Italy).

This research program is performed in the frame of the study of nuclear power plant structure and components behaviour under missile impact.

In the experimental tests, a missile accelerator wich permits to obtain impact velocity ranging between 50-100 m/s for missiles weighing 100-20 Kg respectively has been used (Aquaro,1987,1991).

In the first phase of the experimental program a series of impact tests on circular steel plates having thickness ranging between 8- 25 mm and with impact velocity varying in the 30-100 m/s range has been performed. Moreover, the impact phenomena have been simulated by means a FDM computer code PISCES (Pisces) or a FEM code MARC (Marc,1983) and the experimental results have been compared with the ones predicted by several empirical formulas.

INTRODUCTION

Among the most severe accidents considered since the middle of the seventies in the safety analysis of the Nuclear Power Plants (NPP), the impact of several types of internal or external 'missiles' on structures and components are included.

Internal missiles may be generated by the accidental explosion or damage of pressure vessels,

pipe, valves, pumps, turbines. The fragments generated in the failure of these components may induce severe damage on other safety related components. An aeroplane crash on a NPP containment system is one of the above mentioned possible external missile impact situations, the probability of which is not negligible because it is not always so easy to find nuclear sites very far from airports or airways.

Since 1970,after an aeroplane failure near a Nuclear Research Centre in Switzerland,the Competent Authorities of many Countries begun to consider also this type of accident in the design of the containment structures.

In studies performed in the USA, Germany and France, the aeroplane engine have been considered the most dangerous missile generated in these situations.For instance the characteristics of the above mentioned hard missiles,as established also in the Regulations of several Countries, are in the following range:

- weigth < 2000 Kg
- speed < 80-100 m/s
- diameter < 1200 mm.

At DCMN of the Pisa University, a theoretical and experimental research program on the effects of the missile impact against metallic and steel-concrete compound structures is being carried out.

The acceleration of large masses up to 100 m/s requires quite complex experimental set up. At the DCMN a reduced scale accelerator model capable to

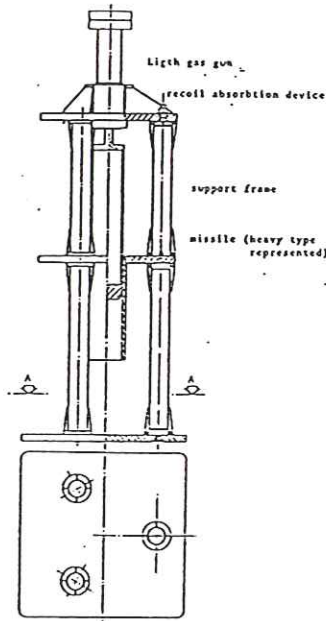


Figure 1 - Main components of the experimental apparatus

push masses having the weight in the range 20-200 kg at maximum speed limits respectively of 100 and 30 m/s was designed and built.

EXPERIMENTAL SETUP USED IN THE TESTS OF MISSILE IMPACT

The fig.1 shows the main components of the experimental apparatus for the simulation of missile impacts, while the fig.2 shows the 'gun' used for the mass acceleration. This gun is essentially a steel cylinder inside of which runs a hollow piston linked to the mass which has to be accelerated.

The cylinder and the piston are connected by means explosive bolts or a set of hydraulic jacks mounted at the lower end of the cylinder.

The acceleration of the missiles is due to the expansion of the pressurized air (maximum pressure 80 MPa) contained in the cylinder once the explosive bolts are blasted or the hydraulic jacks are released.

The gun model under tests is mounted on a tubular structure with its axis in vertical position.

The high pressure air is obtained by means a hydro-pneumatic pressure rising device. The experimental apparatus can accommodate target specimens within maximum dimensions up to

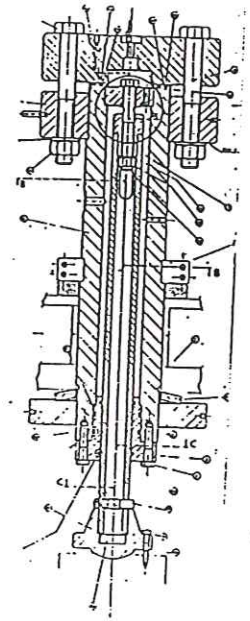


Figure 2 - Pneumatic missile accelerator

500mmx500mmx500mm.

The fig.3 shows the maximum speed of the missile versus its weight for different values of the initial pressure inside the steel cylinder.

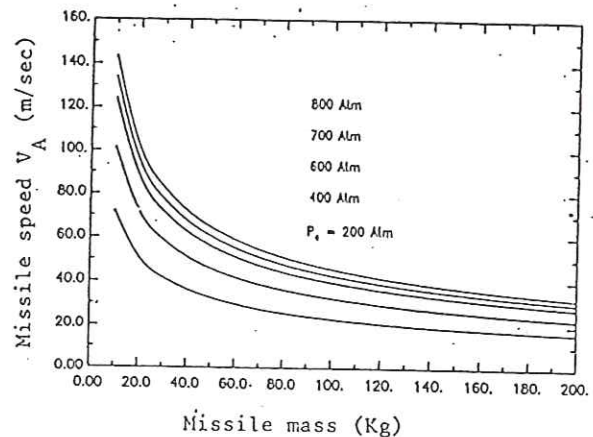


Figure 3 - Missile speed versus missile mass and gas pressure values

test number	Missile velocity (m/sec)	Missile mass (Kg)	Missile diameter (mm)	Plate diameter (mm)	plate thickness (mm)	Missile momentum (N sec)	Steel plates mechanical properties	Maxium permanent (mm)
1	46.08	23.6	60	450	10	1087.5	$\sigma_y = 285\text{MPa}$ $\sigma_R = 444\text{MPa}$ $A = 40\%$	68.1
2	49.40	23.6	60	450	15	1165.8		49.4
3	57.80	23.6	60	450	15	1364.1		94.5
4	61.10	23.6	60	450	15	1442.0	$\sigma_y = 388\text{MPa}$ $\sigma_R = 577\text{MPa}$ $A = 32.5\%$	89.45
5	39.98	36.0	60	450	8	1439.3		P
6	30.70	36.0	60	450	10	1105.2		60.7
7	37.81	36.0	60	450	10	1361.2		P
8	36.39	36.0	60	450	10	1310.0		71.4

σ_y = yielding stress σ_R = ultimate tensile stress A = ultimate tensile strain(%)

Tab. I - Main data of the impact tests

EXPERIMENTAL RESULTS

In the table I, the main data of the impact test on circular tests, elaborated up to date are shown. The plates, made by carbon steel, have a constant diameter equal to 450 mm and thickness ranging between 8-15 mm. The missile, made by a hard high alloy steel, has an emispherical nose and it is characterized by impact velocities varying between

30-60 m/s.

The missile weight ranges between 20-40 Kg.

During the impact test, the missile accelerations as well as the force transmitted by the plate to its supports have been registered. Moreover the radial and hoop strains in different positions of the plates have been measured by means strain gauges.

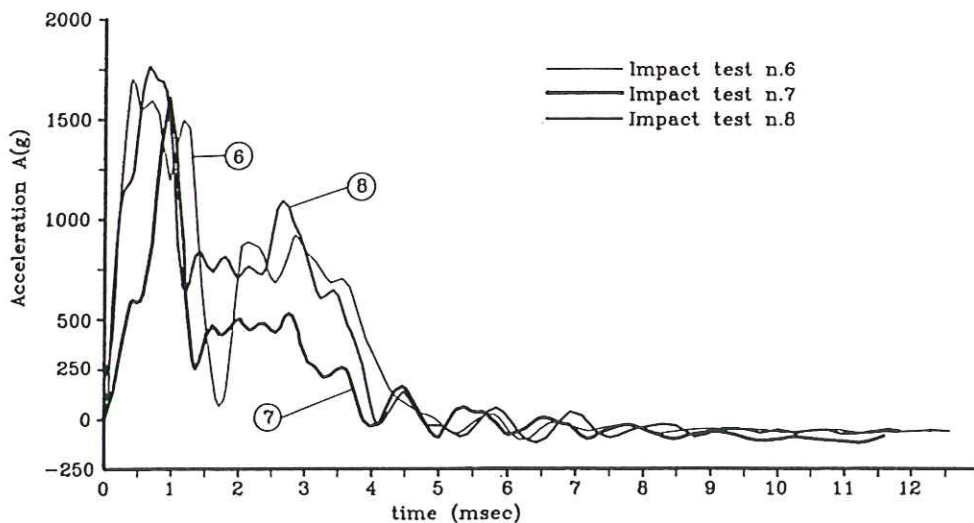


Figure 4 - Missile accelerations registered in impact tests

In fig. 4 the missile accelerations versus the time obtained in three impact tests (test n.6,7 and 8) on plates 10 mm thick are reported. The acceleration maximum value measured in these tests is equal to 1750 g while the transient duration ranges between 4-5 msec.

The fig. 5 shows the total force transmitted by the plate to the supports during the impact test on a plate 15 mm thick (test n.2).

The force diagram corresponds to a target penetration without perforation. The force maximum value is equal to 750 KN, while the impact duration

is equal to 3.9 msec.

The permanent deformations of the plate are shown in fig. 6.

This figure illustrates the global deformation of the plate as well as the local effects. Considering the

local effects we can see that the plate thickness has a great influence on the type of local deformation in the penetration as well as in the perforation. For thickness lower than 15 mm, during the penetration

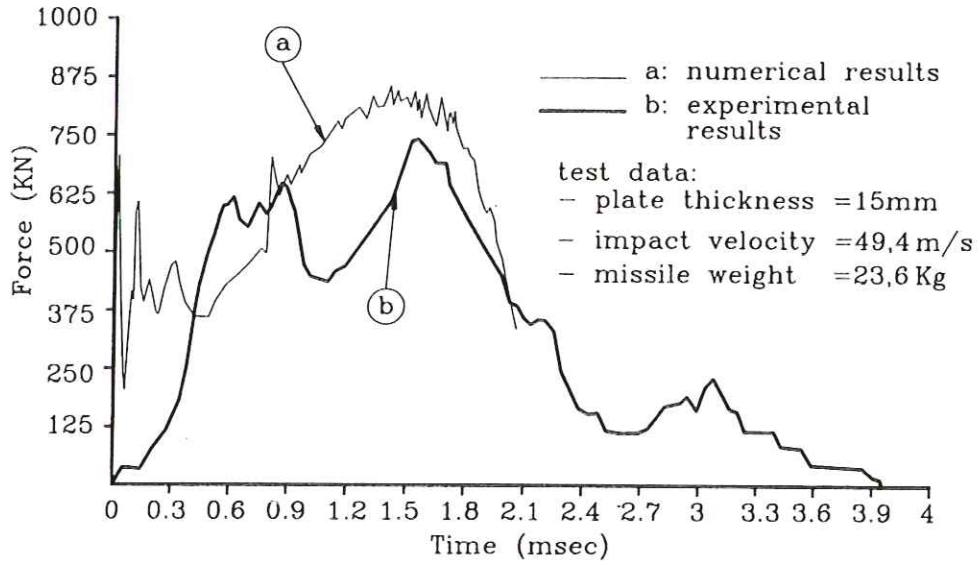


Figure 4 - Force transmitted to the support in a impact test

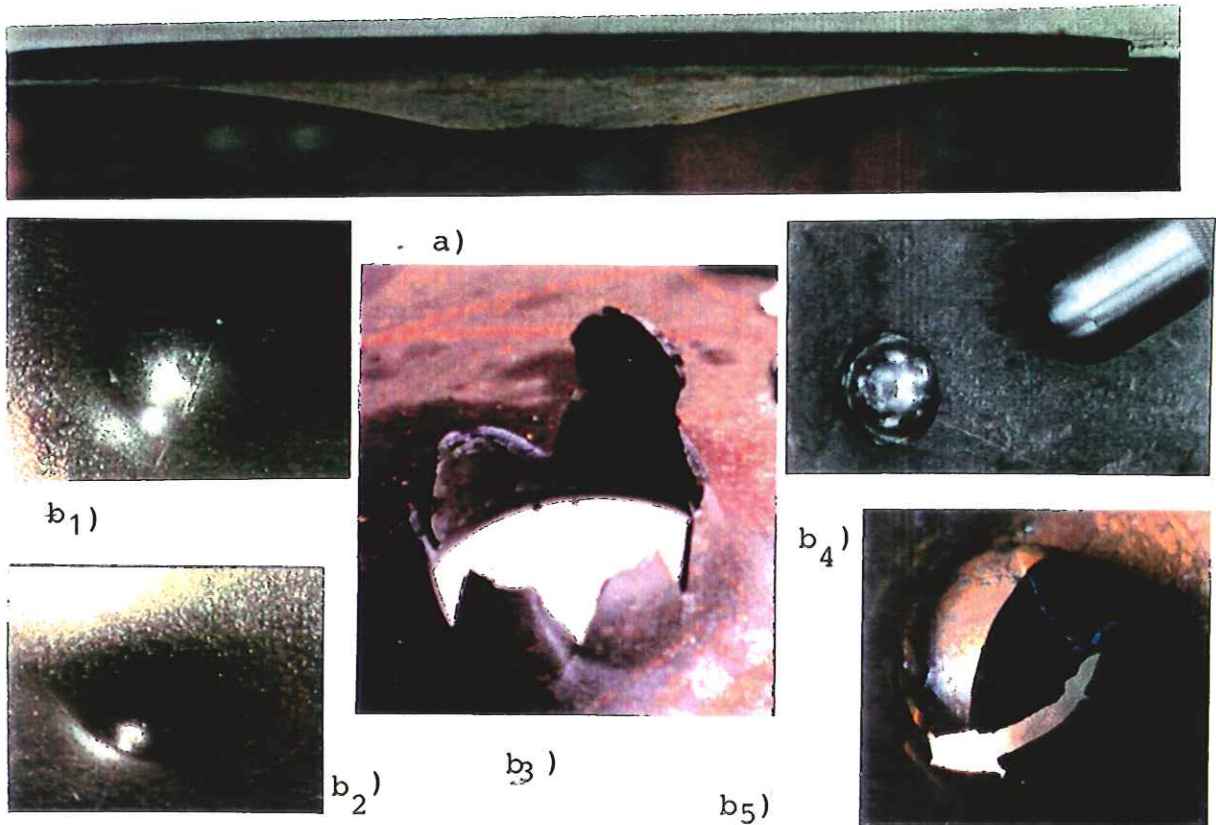


Fig.5-Final deformation of the plate: global (a), local (b)effects

the plate presents a 'bulge' concave or convex on the surface hit by the missile or on the opposite one, respectively (see fig.5-b1 and fig. 5-b2). The perforation produces in these plate a deformation which may be named 'petaling' (fig.5-b3) because the material rupture occurs along radial directions

and pieces of material like 'petals' are formed around the hole caused by the missile.

The deformation mechanism of the impacted zone is different if the plate thickness is equal or greater than 15 mm.

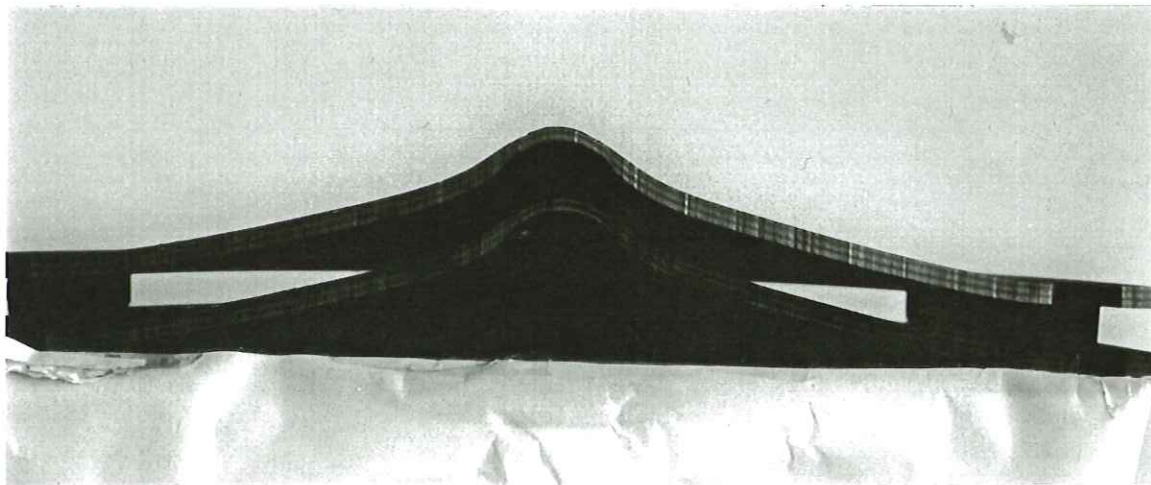


Figure 6 - Cross Section of a penetrated circular steel plate

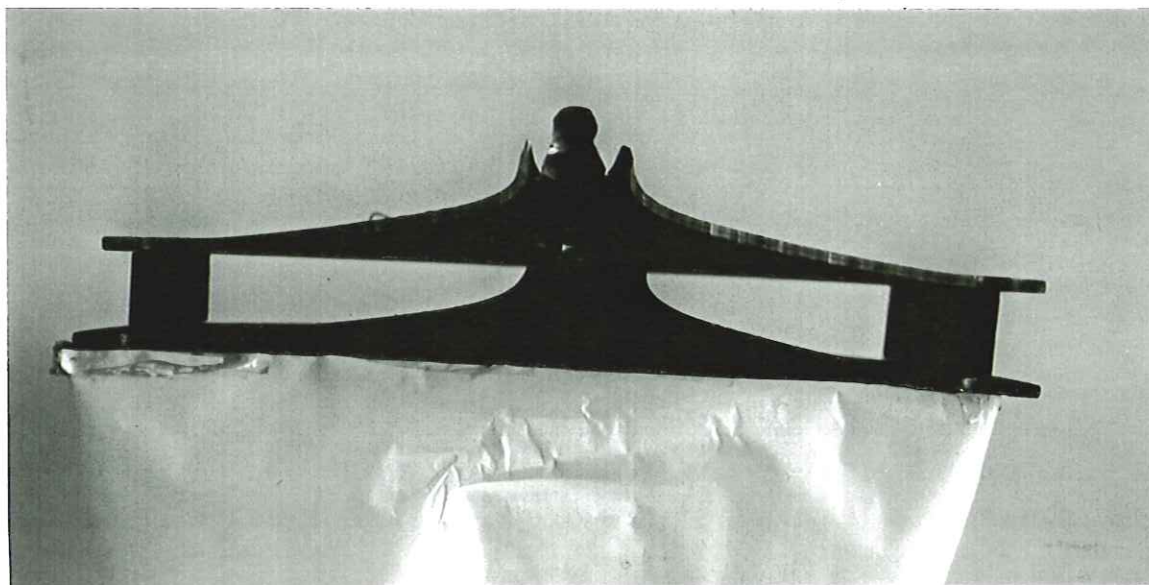


Figure 7 - Cross Section of a perforated circular steel plate

The fig. 5-b4 shows a polished mark determined by the missile on the impacted surface of the plate. The penetration determines locally a very great thickness reduction further a 'bulge' of the same type that it is observed on thinner plates. In the perforation, the missile cracks the plate material along a circumference having a diameter equal to that of the missile and the material is pushed away like a 'plug' (fig.5-b5). This deformation mechanism is named 'plugging'. The figs. 6-7

show the cross sections of a penetrated and a perforated circular steel plate respectively (obtained cutting the deformed plates along a diameter). In the figs. 6-7 the strong reduction of the thickness in correspondance of the impacted area can be seen.

The deformed shape of the target plates, with the exception of a central zone (having linear dimension equal to the diameter missile) where the impact local effect is predominant, seems to be approximated fairly by the following law:

$$W = A \ln(r/R) \quad (1)$$

where:

W = plate displacement (from the undeformed plane) in axial direction (mm)

A = best-fit parameter (mm)

r = current radius

R = target plate radius

As it is possible to see in fig.8 for the test number 2, differences between calculated and experimental data are less than 15%.

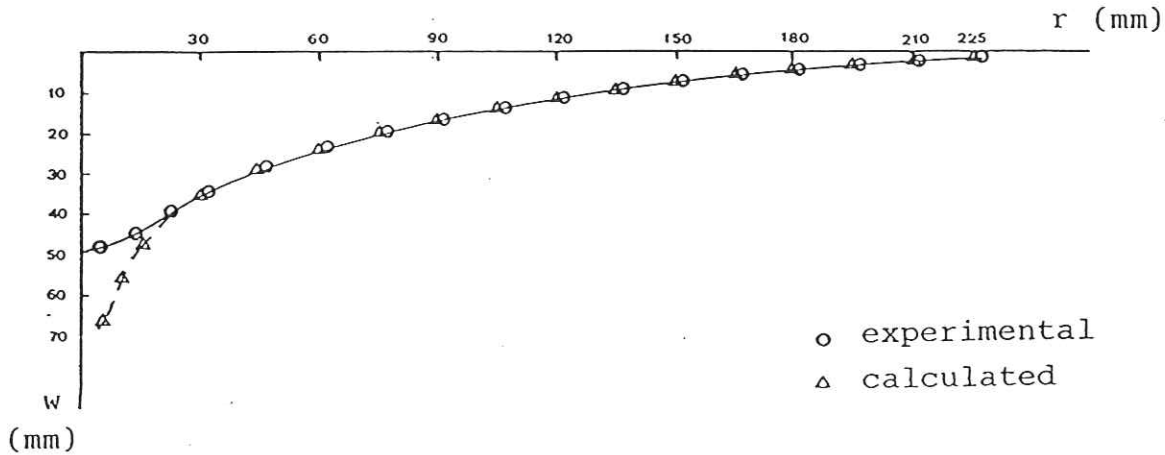


Figure 8 - Comparison between the calculated and experimental displacements of the impacted steel plate

test number	Missile Kinetic energy (J)	PERFORATION ENERGY (J)					Target Final Status
		BRL (1)	De Marre (2)	SRI (3)	Toshiba Hitachi (4)	UKAEA (5)	
1	25056	21016	38291	21870	42621	21390	no perforation
2	28796	38610	67548	40660	78302	42610	no perforation
3	39422	38610	67548	40660	78302	42610	perforation
4	44052	38610	67548	40660	78302	42610	perforation
5	28771	15038.8	28020	20560	30500	19020	perforation
6	16965	21016	38291	28420	42621	27790	no perforation
7	25733	21016	38291	28420	42621	27790	perforation
8	23836	21016	38291	28420	42621	27790	no perforation

(1) BRL: $E_p = 1.431 \cdot 10^9 (e \cdot d)^{3/2}$

(2) Jacob De Marre: $E_p = 1.644 \cdot 10^9 d^{1.5} e^{1.4}$

(3) SRI: $E_p = \frac{de^2 \sigma_R}{10.53} (41.41 + Lp/e)$

for $0.1 < \frac{e}{d} < 0.8$
 $8 < \frac{Lp}{e} < 100$
 $21 < v \text{ (m/s)} < 120$
 $420 < \sigma_R \text{ (MPa)} < 490$

(4) Toshiba-hitachi: $E_p = 2.9 \cdot 10^9 t^{1.5} d^{1.5}$

for $Lp = 1.5m$
 $3 < w \text{ (Kg)} < 250$
 $25 < v \text{ (m/s)} < 180$

(5) UKAEA: $E = 1.4 \sigma_R d^3 \left\{ \left(\frac{e}{d} \right)^{1.7} \left(\frac{Lp}{d} \right)^{0.6} \right\}$

for $1 < w \text{ (Kg)} < 20$
 $1 < e \text{ (mm)} < 25$
 $10 < v \text{ (m/s)} < 100$
 $32 < d \text{ (mm)} < 65$
 $320 < \sigma_R < 473$

d(m) = missile diameter
 $\sigma_R \text{ (N/m}^2\text{)}$ = ultimate tensile stress
Lp(m) = unsupported plate span
v(m/s) = missile impact velocity
w(Kg) = missile weight
e(m) = plate thickness

Table II - Comparison between the missile kinetic energy and perforation energy predicted by empirical formulas

COMPARISON BETWEEN THE EXPERIMENTAL RESULTS AND THE EMPIRICAL FORMULA PREDICTIONS

In the technical literature (Brown-1986, Neilson 1985), a lot of empiric formulas which permit to obtain an estimate of the energy necessary to

perforate a steel plate, are known. Five of these formulas are reported in tab.II with their range of applicability, if known. In the same tab. II, the kinetic energy of the missile in the impact tests is compared with the perforation energy predicted by the different formulas; moreover the target final status is reported.

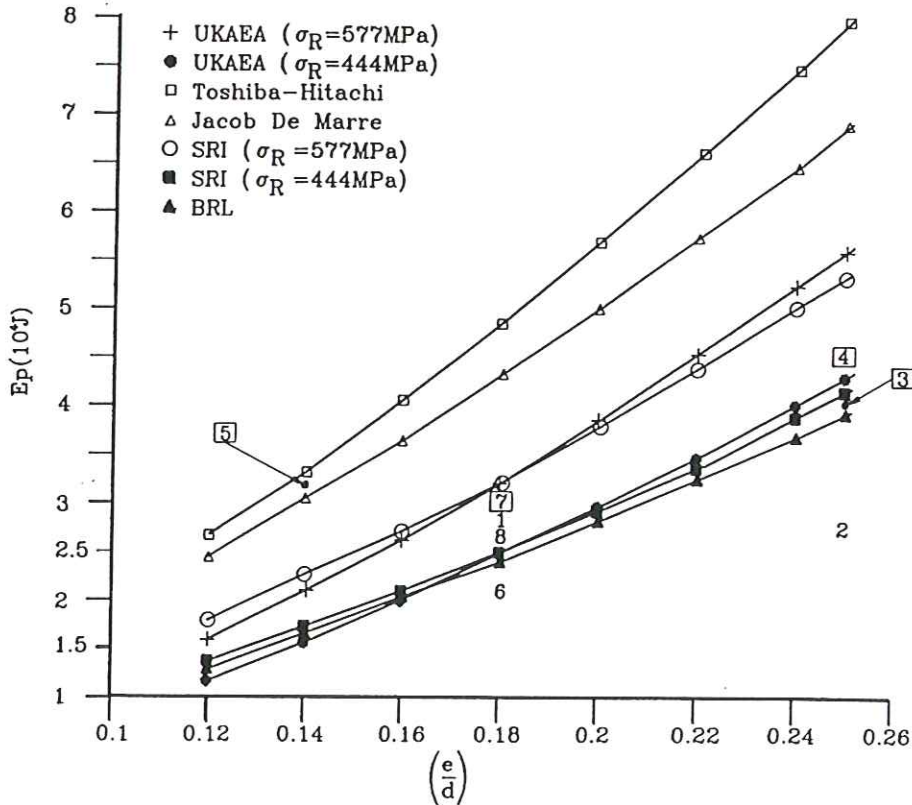


Figure 9 - Comparison between the experimental data and the empirical formulas predictions

The fig. 9 shows the curves corresponding to the formulas taken in consideration in the range of the adimensional parameter e/d of our interest (being e , the plate thickness and d , the missile diameter). The BRL (Ballistic Research Laboratory), the Jacob De Marre and Toshiba-Hitachi formulas give the perforation energy as function the plate thickness and missile diameter. The SRI (Stanford Research Institute) and UKAEA formulas (the latter is an adimensional formulation of the former) calculate the perforation energy as function of the ultimate tensile stress (σ_R) the unsupported plate span (L_p) farther than the plate thickness (e) and missile diameter (d). These two last formulas are reported in fig. 9 for two values of ultimate tensile stress ($\sigma_R=444\text{MPa}$ and $\sigma_R=577\text{MPa}$) and for $L_p=450\text{ mm}$. In the fig. 9, the experimental data are compared with the curves corresponding to the empiric formulas. The comparison shows that the Jacob De Marre and Toshiba-Hitachi overestimate the perforation energy

while the SRI and UKAEA give results in good agreement with the experimental ones with a +/- 15% tolerance.

The BRL formula generally underestimates the perforation energy even if, in our range of interest, the underestimation is contained in a -18% tolerance.

NUMERICAL SIMULATION OF AN IMPACT TEST ON A CIRCULAR PLATE 15MM THICK

The impact phenomenon has been simulated by means the FDM code PISCES and the FEM code MARC . In the following some results of the numerical simulation, performed by the MARC, of the 15 mm thick plate penetration are reported.

Fig.4 - Comparison between the experimental data and the empirical formulas predictions

The fig. 5 shows the deformation pattern of the plate at different instants of the time. The numerical

simulation has regarded the impact test n. 2 (see tab. I). Therefore the impact velocity and the missile weight have been assumed equal to 49.4 m/s and 23.6 Kg respectively. In the fig.5, the force transmitted by the plate to the support, as obtained numerically, is compared with the experimental one. The numerical maximum value of the force (825 KN) is 10% greater than the experimental value (750

KN). But the difference between the initial slopes of the two curves as well as the different transient duration might be due, in some extent, to the simulation of the support. In the calculations the plate is perfectly built-in while the real support is a friction connection realized putting the plate between two bolted flanges. Therefore this type of support permits a little slip respect the flanges under

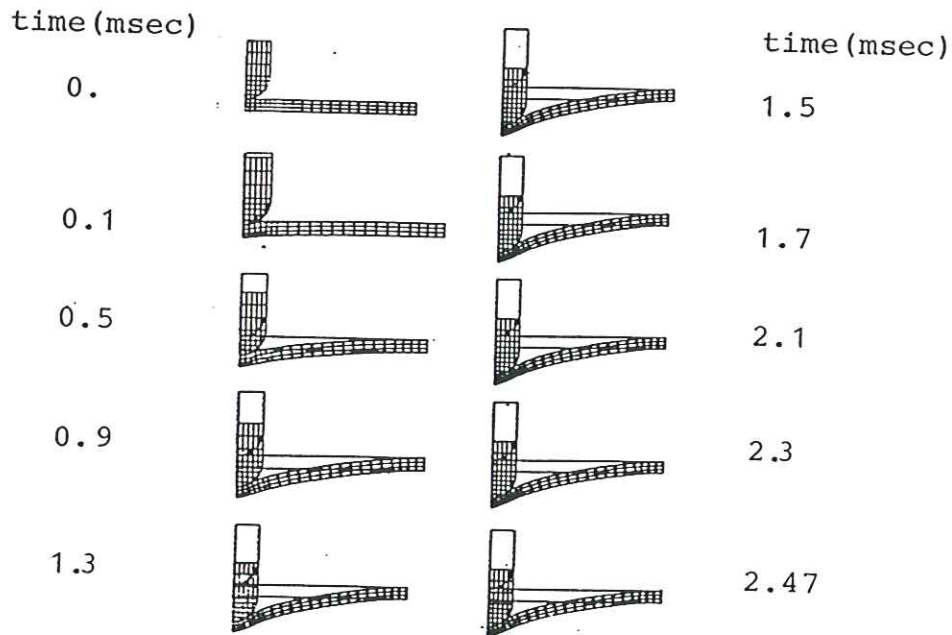


Figure 10 - Deformation pattern of a circular steel plate impacted by an emispherical missile as obtained by numerical simulation

the action of the great tensile force developed during the plate deformation.

The maximum displacement of the middle point of the plate is equal to 52.88 mm while the experimental one is equal to 49.4 mm.

CONCLUSIONS

The results of the impact tests on circular steel plates described in this paper show that the impacted zone is deformed by different mechanism depending on the plate thickness. Thick plates show a strong

thickness reduction and a rupture like a 'plug' in correspondance of the impacted zone, while thinner plates present a pronounced 'bulge' in the penetration and a rupture like 'petals'.

The SRI and UKAEA formulas predict with a +/- 15% tolerance the perforation energy while other empirical formulas seem to overestimate or underestimate the energy.

The FEM simulation of the penetration gives plate deformation, maximum force and maximum displacement in a good agreement with the experimental values.

REFERENCES

- D.Aquaro-G.Forasassi(1987)-'An experimental setup for intermediate speed impact simulation studies related to the safety of NPP structures and components' 9th I.C.SMIRT August 1987-Lausanne-A.A.Balkema
- D.AQUARO ' Missile perforation resistance of circular plates: comparison between numerical and experimental results' Tr. 11th SMIRT- Atomic Energy Society of Japan - Tokyo August 1991
- PISCES-Int.bv-Groningenweg6-2803PVGouda-Netherlands
- MARC Analysis Research Co.- Palo Alto-California,1983
- S.Brown-(1986) Appl.Mech.Rev.,vol.39,n.2,feb 1986
- A.J.Neilson-Int.J.ImpactEngng.vol.3,n.2,pp137-142,1985-Pergamon
- S.Yamamoto et alii-7th Int. Conf. SMIRT-Chicago 1983

CRACK PROPAGATION IN IMPACT LOADED DUCTILE STEEL THREE POINT BEND SPECIMEN WITH A QUARTERNOTCH

Anders Bergmark

Division of Solid Mechanics, Lund Institute of Technology
Box 118, S-221 00 LUND, Sweden

ABSTRACT

Static and dynamic experiments on crack growth in three point bend specimens have been made for two different ductile steels. The specimen size is 320x75x10mm and the impact velocities were 30 and 45 m/s. The loading device includes a U-shaped impact hammer in order to minimize the movement of the specimen midsection the crack growth can therefore be tracked by the high speed camera through the specimen. A modified 3PB specimen design is used to minimize the influence of friction and mechanical locking where the impact heads hit the specimen. Three properties are evaluated from the photos namely the crack growth, the crack tip opening displacement at the position of the original crack tip, CTOD, and the relative rotation of the two specimen halves, $\Delta\varphi$. CTOD and $\Delta\varphi$ are the loading parameters. Load rate dependence is found from the relation between CTOD and the crack growth.

INTRODUCTION

Dynamic fracture testing of three point bend (3PB) specimens is widely used in order to evaluate criteria for onset of crack growth and for running cracks in brittle as well as in ductile materials. Data are needed for characterization of materials and also for calibration of numerical models [Shivakumar, 1989].

Dynamic 3PB tests may be performed in drop weight towers, by means of a gas gun or other device to accelerate the projectile or hammer which hits the specimen. Experiments performed in the acceleration track at the Division of Solid Mechanics at Lund Institute of Technology will be presented here. The dynamic loading device combines the heavy impact hammer weight normally used in drop weight towers with the high impact velocity which can be reached using a gas gun. Relatively large steel specimens may therefore be investigated.

Static and dynamic fracture experiments are normally evaluated under the assumption that there exists a one parameter relation between the loads acting on the specimen and the stress state close to the crack tip. This is the *autonomy* concept and the results are presented as stress intensity factors (SIF) or *J*-integral values. Static

fracture tests may be evaluated by calculating the SIF or *J*-integral from the loads acting on the specimen. Optical methods may also be used for the analysis of static experiments, for example caustics, Moire interferometry and photoelasticity [Smith, 1987].

Evaluation of dynamic tests cannot be based on the forces acting on the specimen as these might be completely dominated by inertia effects [Böhme, 1982]. Direct measurement of the crack tip behavior is therefore needed. Caustics has been used with great success in dynamic experiments, for example [Ravi-Chandar, 1984; Zehnder, 1990; Theocaris, 1981], but, as already mentioned, the method is limited to cases where autonomy of the process region is obtained. Autonomy of the process region is not likely to be expected in ductile material where the crack growth process is preceded by the development of a plastic hinge at the crack tip [Broberg 1986].

In general the *crack tip load* constitutes of the properties of the stress and strain field which contributes to the separation of material in front of the crack tip and thus creating new fracture surfaces. In this paper, two well defined geometric properties are chosen as crack tip load, namely the crack tip opening displacement (CTOD) at the original crack tip position and the relative rotation ($\Delta\varphi$) of the two specimen halves.

CTOD has been used as criteria for onset of crack growth at static loading, for example [Lou, 1989]. Here CTOD and $\Delta\varphi$ will be used as criteria for the dynamic cases. These properties are also suitable with respect to the experimental situation as they are easily measurable properties from the high speed camera recordings.

EXPERIMENTS

A U-shaped hammer is used for the dynamic experiments. The standstill midsupport was introduced as minimum movement of the specimen midsection is wanted for the high speed camera recordings. Quasistatic experiments were made in order to analyze the difference between static and dynamic loading. The displacement velocity at the quasistatic tests were 50 mm/minute and a 24x36 mm camera was used to record the event.

MATERIALS

The experiments were on two ductile steels. The first is the Swedish microalloyed structural steel SIS 142134 (similar to steel Grade E355, quality DD of ISO 4950/2) with carbon equivalent not exceeding 0.41%. The second is the hardened and tempered structural steel with commercial name SSAB: WELDOX700 (similar to ASTM A514).

Results from two experiments at impact velocities 30.2 and 45.2 m/s are presented for material number one and from one experiment on material number two at 30.4 m/s impact velocity.

SPECIMEN

Earlier dynamic experiments on 18mm thick 3PB quarter-notched 320x75mm specimens in material number one [Drar, 1993] showed transition to partly brittle behavior in the specimen interior at dynamic loading. The thickness of the shear lips obtained at these earlier experiments were approximately 5 mm. Here the specimen thickness was reduced to 10 mm in order to avoid the ductile-brittle transition. Earlier experiments on material number two using 18mm thick specimens (not reported elsewhere) did not show such transition. The same thickness was, however, used for both materials.

A modified specimen design with reduced width at the ends is introduced. The aim is to avoid the influence of friction and mechanical locking caused by the excessive plastic indents at the ends where the U-shaped hammer hits the specimen. The specimen geometry is shown in Fig.1.

MEASUREMENTS

All data presented are obtained from direct measurements on the negative films using a microscope. Three properties are evaluated: $\Delta\varphi$, CTOD and the crack growth. Moiré interferometry was used to display the relative rotation of the two specimen halves and $\Delta\varphi$ was calculated from the moiré interference pattern. The principle crack propagation as seen on the photos is shown in Fig.2. With reference to this figure, the crack growth may be described in 4 steps:

1. The original fatigue precrack.
2. Initial crack surface separation is first obtained in combination with blunting of the crack tip. The crack propagation, Δa , during the blunting is best seen on the high resolution photos from the quasi-static tests.
3. Necking is obtained to the right of the broken line. The necking edge is seen as a sharp shadow on the photos.
4. Crack propagation continues from the blunting root. The crack plane is turned 45° a few mm from the original crack tip. The crack growth as presented in the diagrams is measured from the blunting root.

RESULT

The results for material one is shown in Fig.3 and Fig.4. Fig.3 displays the Crack growth as a function of the relative rotation. The crack growth is measured from the blunting root (post-blunting crack growth). The difference between the static and the 30 m/s case is small. A clear load rate dependence is seen for the 45 m/s impact velocity case. Onset of crack growth starts at about 0.1

rad relative rotation with a slightly smaller value at the highest impact velocity.

Fig.4 shows the post-blunting crack growth as a function of the CTOD. Here a clear influence of the load rate is seen with onset of crack growth at smaller CTOD for increased impact velocity. Onset of crack growth starts at about 3 mm CTOD for static loading and at about 2 mm for the highest impact velocity.

The results for material two are shown in Fig.5 and Fig.6. Fig.5 displays the crack growth as a function of the relative rotation $\Delta\varphi$. No load rate influence is seen from the diagram. Crack growth starts at about 0.06 rad relative rotation.

Fig.6 shows the crack growth as a function of CTOD. Onset of crack growth starts for a smaller CTOD at dynamic loading, which indicates load rate influence also for material two. Onset of crack growth starts at about 2 mm CTOD for static loading and at about 1.7 mm CTOD for 30 m/s impact velocity.

CONCLUSION

The post-blunting crack growth at static and dynamic loading has been investigated as a function of two different loading parameters: CTOD and $\Delta\varphi$, the relative rotation of the two specimen halves. A clear load dependence has been found between the crack growth and the CTOD for both materials.

NOMENCLATURE

CTOD	mm	Crack tip opening displacement at the position of the original crack tip
Δa	mm	Crack growth from the blunting root
$\Delta\varphi$	rad	Relative rotation of the two specimen halves

REFERENCES

- BÖHME W. and KALTHOFF J.F. 1982 - *The Behavior of Notched Specimens in Impact Testing*. Int Journal of Fracture, 20:R139
- BROBERG K.B. 1986 - *Crack Tip Characterizations*. Engng Fracture Mech, 23(1):161-166.
- DRAR H. and BERGMARK A. 1993 - *Load rate Influence on the Fracture Morphology of a Ductile Steel*. Engng Fracture Mech.; in press.
- LUO L.G. QUARRINGTON A.I. and EMBURRY J.D. 1988 - *Effect of Specimen Geometry on Ductile Initiation CTODi Using a Direct Method*. Engng Fracture Mech 31(2):349-356.
- RAVI-CHANDAR K. and KNAUSS W.G. 1984 - *An Experimental Investigation into Dynamic Fracture: I. Crack Initiation and Arrest*. Int Journal of Fracture, 25:247-262.
- SHIVAKUMAR K.N. and NEWMAN Jr J.C. 1989 - *Numerical Fracture Simulation of Bend Specimens Using a CTOD Criterion*, Engng Fracture Mech 32(2):203-210.
- SMITH C.W. and KOBAYASHI A.S. 1987 - *Experimental Fracture Mechanics*. Chapter 20:891-956. Prentice-Hall Inc.
- THEOCARIS P.S. and ANDRIANOPOLOUS N.P. 1981 - *Dynamic Three-Point Bending of Short Beams Studied by Caustics* Int Journal of Solids and Structures, 17(7):707-715.
- ZEHNER A.T. ROSAKIS A.J. and KRISHNASWAMY S. 1990 - *Dynamic Measurement of the J-integral in ductile metals: Comparison of experimental and Numerical Techniques*. Int Journal of Fracture 42:209-230.

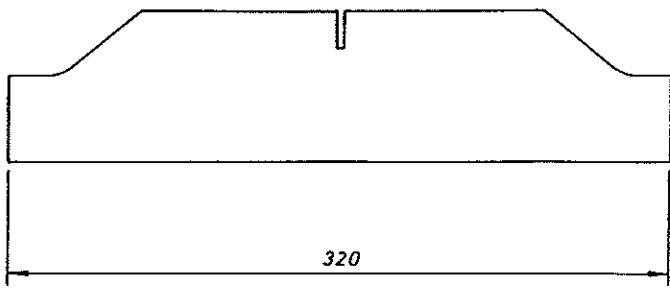


Fig. 1. Modified 3PB specimen with reduced width at the ends.

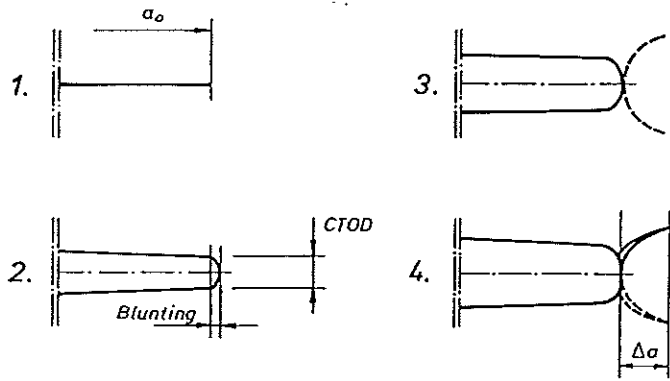


Fig. 2. Principle crack growth in ductile steel.

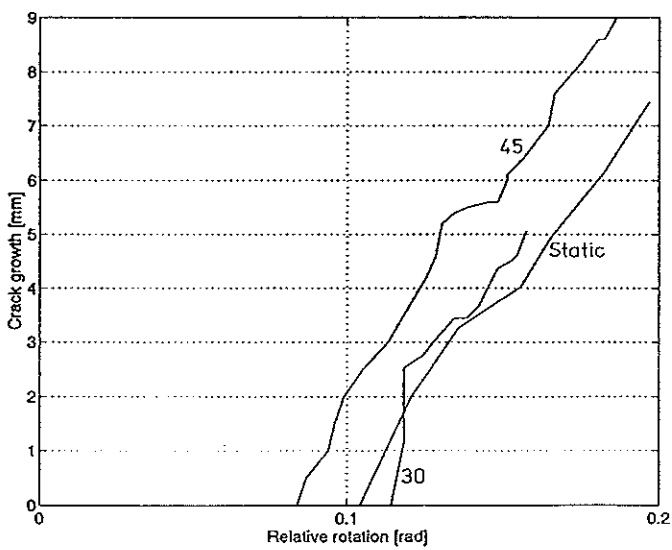


Fig. 3. Crack growth as a function of the relative rotation $\Delta\varphi$. Material 1, static and 30 and 45 m/s impact velocities.

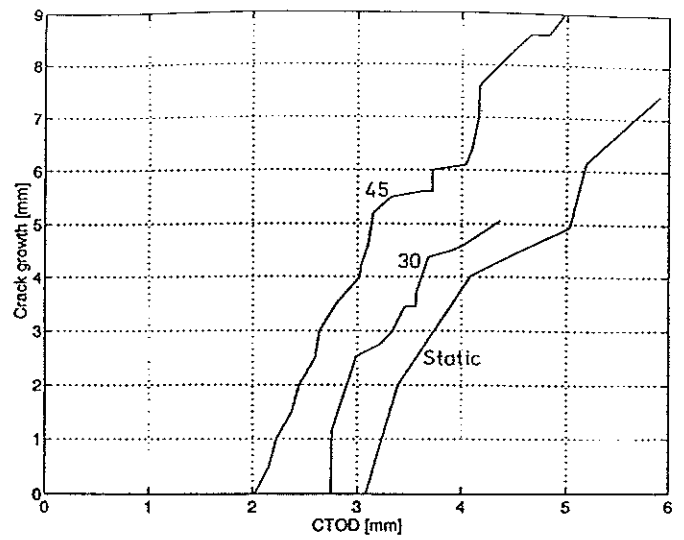


Fig. 4. Crack growth as a function of CTOD. Material 1, static and 30 and 45 m/s impact velocities.

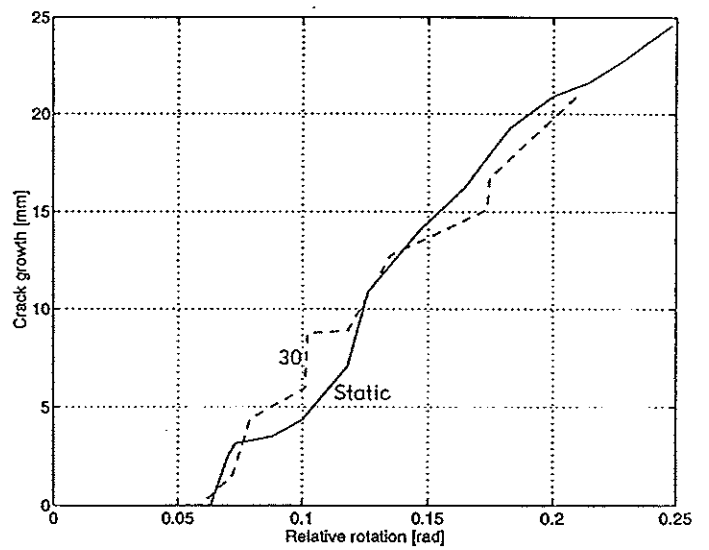


Fig. 5. Crack growth as function of the relative rotation $\Delta\varphi$. Material 2, static and 30 m/s impact velocity cases.

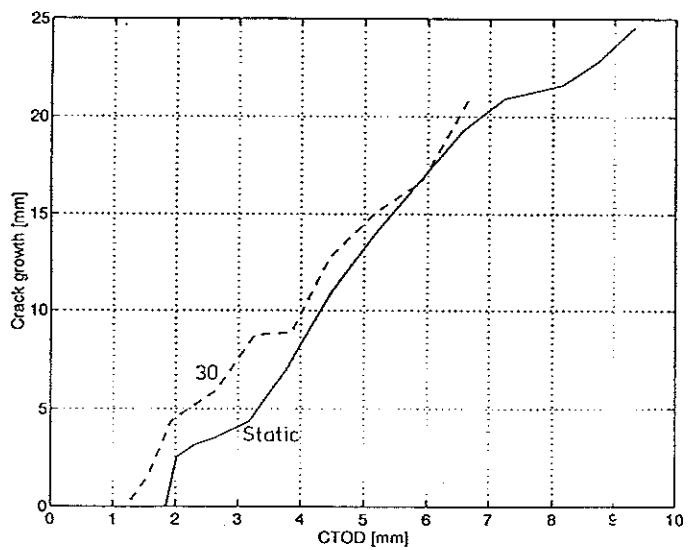


Fig. 6. Crack growth as a function of CTOD. Material 2, static and 30 m/s impact velocity.

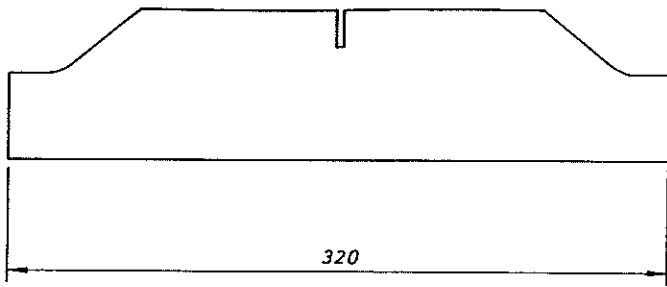


Fig. 1. Modified 3PB specimen with reduced width at the ends.

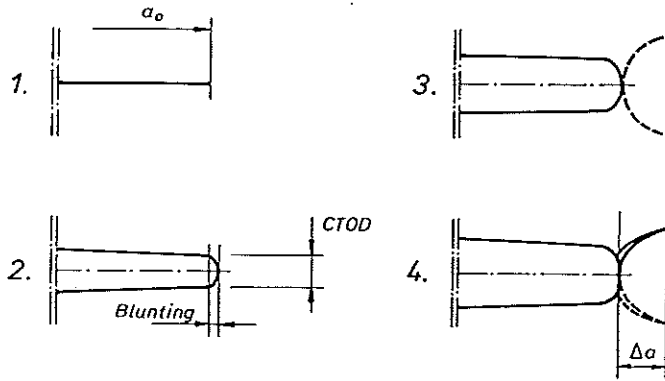


Fig. 2. Principle crack growth in ductile steel.

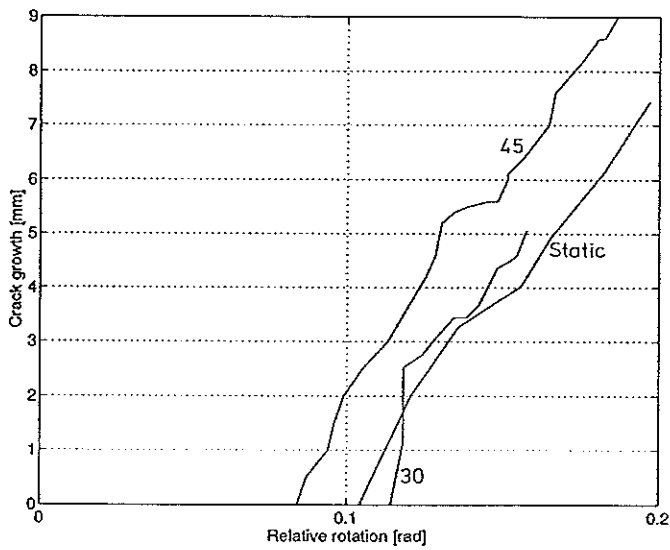


Fig. 3. Crack growth as a function of the relative rotation $\Delta\varphi$. Material 1, static and 30 and 45 m/s impact velocities.

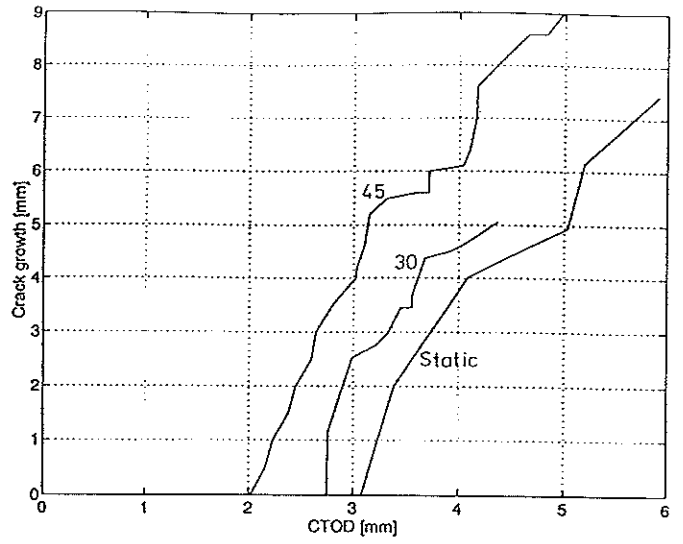


Fig. 4. Crack growth as a function of CTOD. Material 1, static and 30 and 45 m/s impact velocities.

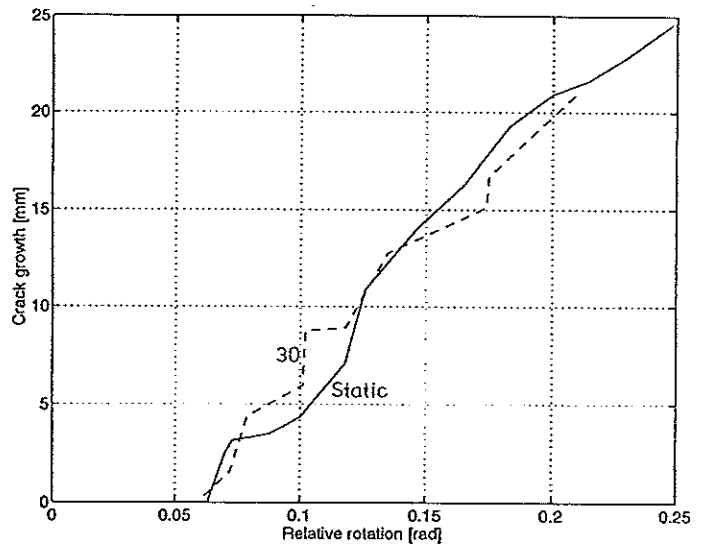


Fig. 5. Crack growth as function of the relative rotation $\Delta\varphi$. Material 2, static and 30 m/s impact velocity cases.

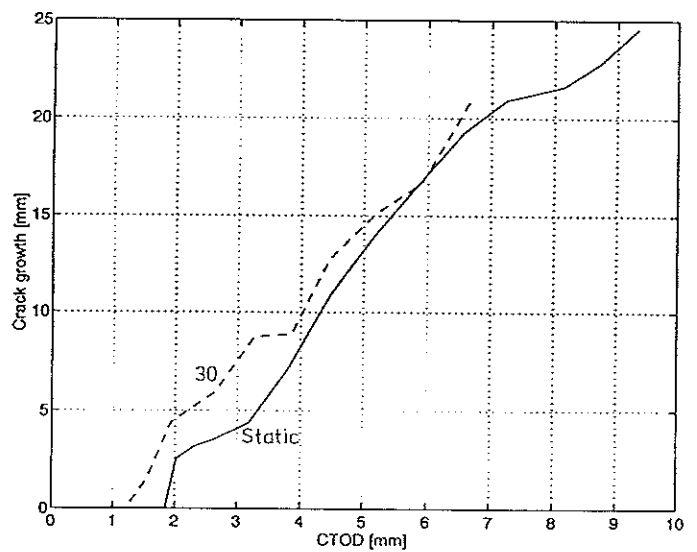


Fig. 6. Crack growth as a function of CTOD. Material 2, static and 30 m/s impact velocity.

THE INFLUENCE OF THE INITIAL MICROSTRUCTURE
OF LOW ALLOYED HIGH STRENGTH STEEL
ON ITS RESPONSE TO IMPACT LOADING

Jaroslav Buchar

Department of Physics, University of Agriculture
Zemědělská 1, 613 00 Brno, Czech Republic

Jan Krejčí

Institute of Physical Metallurgy, AS CR
Žižkova 22, 616 62 Brno, Czech Republic

ABSTRACT

The influence of different microstructures of the low alloyed high strength steel (LAHS) on its response to the different types of impact loading is studied. The crack initiation at stress pulse loading, spall behaviour and the penetration of this steel by shaped charge jets are investigated. The experimental results obtained by different loading suggest that the initial microstructure of the steel affects the steel's response to the impact loading regardless of loading type and intensity.

INTRODUCTION

The term impact loading involves many different loading processes, e.g. the impact of solid projectile, irradiation by a pulse laser, detonation of explosive in contact with material etc. In the case of the first of these examples, the material behaviour is usually characterized by means of a dimensionless damage number [Hutchings 1983].

$$D = \rho V^2 / Y \quad (1)$$

where ρ is the density of the target material, V is the impact velocity and Y is the yield strength of the target material.

For $D \gg 1$, the strength of the

material is expected to be unimportant compared with its density, while for $D < 1$, the response of the target should depend entirely on its strength properties.

Our preliminary results reported in [Krejčí et al. 1992] revealed that the strength properties were important also for $D \gg 1$. In order to clarify this problem a serie of experiments was performed on low alloyed high strength steel.

EXPERIMENTAL

For the experiments LAHS steel (0.75C, 1.8Mn, 1.68Si, 0.014P, 0.005S, 1.03Cr, 0.14Ni, 0.08Cu - in wt%) was used. In order to obtain different levels of strength characteristics different heat treatments were used. Heat treatment and relevant mechanical properties are given in Table 1. Beside these characteristics obtained at strain rate $5 \times 10^{-4} \text{ s}^{-1}$, the dynamic properties were determined at strain rates $10^3 - 10^4 \text{ s}^{-1}$ by Hopkinson Split Pressure Bar technique [Buchar and Bílek 1983]. The dynamic behaviour of the steel was characterized by parameter, β , which gives the dynamic overstress

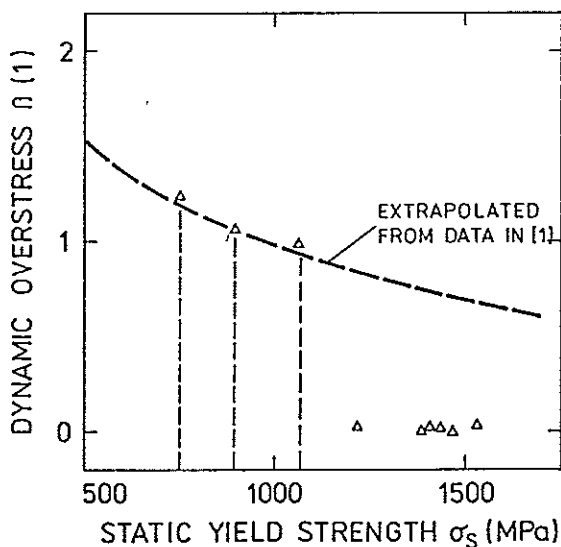
$$\beta = (\sigma_y - \sigma_s) / \sigma_s$$

where σ_y is the dynamic yield

Table 1. Tensile and fracture properties of the tested steel.

Code	Heat treatment (Quenching and Tempering)	Yield strength [MPa]	Ultimate Tensile Strength [MPa]	Fracture toughness [MPa m ^{1/2}]
R	1100°/0.5h/oil +180°/2h/air	1390	1818	69
C	840°/0.5h/oil +180°/2h/air	1530	1978	52
D	840°/0.5h/oil +250°/2h/air	1470	1732	49
E	840°/0.5h/oil +320°/2h/air	1440	1620	52
F	840°/0.5h/oil +400°/2h/air	1401	1518	72
G	840°/0.5h/oil +500°/2h/air	1220	1256	95
H	840°/0.5h/oil +600°/2h/air	1070	1104	124
K	840°/0.5h/oil +650°/2h/air	890	929	140
L	840°/0.5h/oil +700°/2h/air	750	867	168

Fig. 1. The dynamic overstress as a function of the static yield strength.



strength at strain rate approaching infinity and σ_s is the quasi-static yield strength. According to the results [Buchar and Bilek 1983], the parameter, β , is decreasing as σ_s increases, as shown in Fig. 1. Experimental data obtained for different microstructures of the steel follow this curve up to value of σ_s about 1220 MPa. The microstructures

which exhibit higher values of σ_s show almost no dynamic overstress.

The following experiments were performed:

- Crack stability studies by the procedure which is described in [Buchar 1992].

- The spall strength of the steel studied was evaluated as a function of the strain rate. The details of these experiment are given e.g. in [Buchar and Elices 1991].

- Time resolved measurements of the jet penetration velocity have been performed - see [Buchar et al. 1993] for details.

All experiments were performed at room temperature .

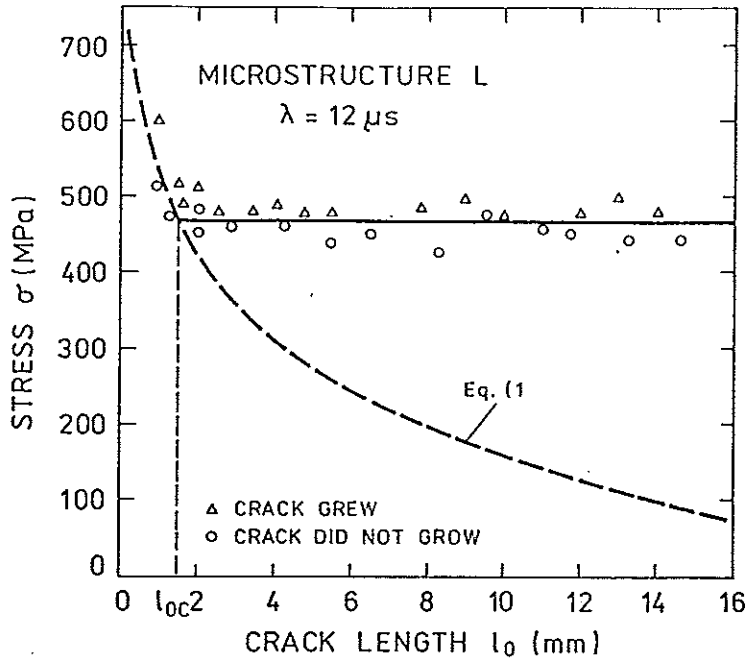
RESULTS AND DISCUSSION

In the first step a study of crack stability under stress pulse loading was performed. It is well known that under quasi-static loading, an initial crack becomes unstable if the stress intensity factor, K_I , equals or exceeds the fracture toughness, K_{IC} , i.e.

$$K_I \geq K_{IC} \quad (2)$$

When the load is applied very rapidly (e.g. when stress pulse strikes the crack), the prediction

Fig. 2. Crack stability data.



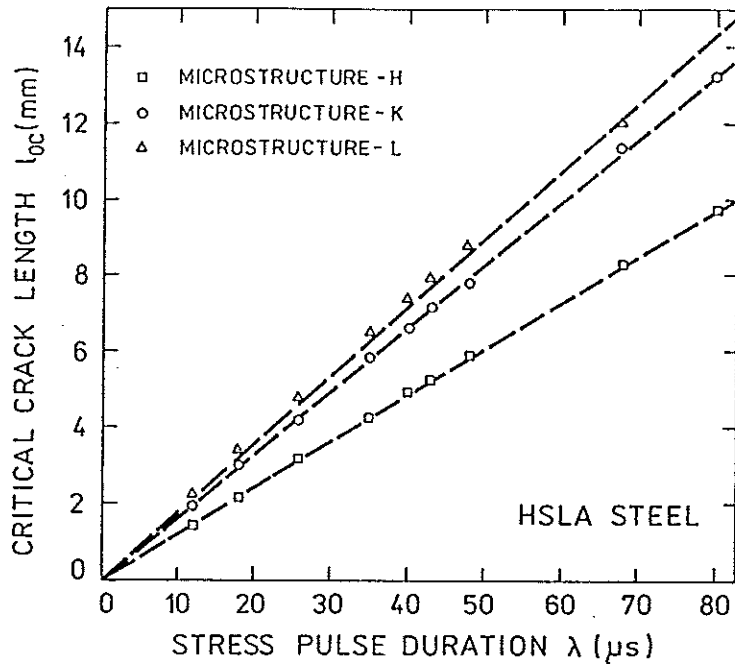
of crack instability may become more complicated. The material may exhibit a different fracture resistance and the crack tip stress intensity usually becomes more or less complicated function of time. The experimental results obtained till now [Kalthoff 1977, Shockey 1983] show that the instability criterion (2) mostly fails under these loading conditions.

In Fig. 2 an example of such crack behaviour is given. For short crack lengths, the crack growth initializing stress decreases with increasing crack length in accordance with criterion given by Eq. (2). Increasing the crack length, the critical stress reaches a constant value. The crack length, $l_0 = l_{0c}$, corresponding to this transition in the crack behaviour is an increasing function of the stress pulse duration, λ , as documented in Fig. 3. Figure 3 also shows that this critical length of the crack depends on the type of microstructure. The detail analysis performed in [Buchar 1992] revealed that this crack behaviour was observed only for the microstructures which exhibited some dynamic overstress - see Fig. 1. The remaining microstructures exhibited the usual crack behaviour predic-

ted by the Eq. (2). These results suggest that there is a time interval during which K_I must exceed the K_{Ic} for crack to start propagating. This incubation period is an increasing function of the strain rate sensitivity given by parameter β , or a decreasing function of the static yield strength, σ_s .

Even if the crack existing in the structure play a role in its final failure under impact loading, the more typical failure of dynamic loaded body is spallation. Spallation is a type of fracture that consists of planar separation along the plane parallel to the incident and reflected plane wave front. The development of spall in a body subjected to the impact loading involves cooperative nucleation, growth and coalescence of voids that depend on both the pre-existing microstructure of the spalling body and its development during the loading [Grady 1988]. The exact description of the spall - fracture taking into account all possible microstructural changes is very difficult if not impossible. This is why a new approach to the spall evaluation is used. This approach is based on the theory given in [Grady 1988]. For solids which fail through the

Fig. 3. The dependence of the critical crack length on the stress pulse duration.



growth and coalescence of cracks this theory leads to the following expression for the spall strength

$$\sigma_c = \sqrt[3]{\rho c_0 K_{Ic} \dot{\epsilon}} \quad (3)$$

where ρ is the material density, $c_0 = \sqrt{K/\rho}$, K is the bulk modulus and $\dot{\epsilon}$ is the strain rate in the spall plane.

Equation (3) can be applied to both brittle and ductile crack growth.

There are many materials which fail through the growth and linking up of voids (copper, aluminium etc.). For these materials the spall strength is given by

$$\sigma_c = \sqrt{2\rho c_0 Y_f \epsilon_c} \quad (4)$$

where Y_f is the flow stress which is assumed to completely characterize the local plasticity during spall failure and ϵ_c is the critical void volume fraction. The rise above this value is followed by coalescence of voids and fast loss of tensile load - carrying capability ensue.

For metals which fail by ductile crack growth we may expect a transition from K_{Ic} - dominated spall to Y_f - dominated [Grady 1988]. The strain rate correspon-

ding to this transition may be determined by equating the spall strengths in Eqs. (3) and (4), i.e.,

$$\dot{\epsilon}_c = \frac{2}{3} \left(\frac{c_0}{K_{Ic}} \right)^2 \sqrt{2\rho Y_f \epsilon_c^3} \quad (5)$$

In Fig. 4 the experimental results, i.e. σ_c vs $\dot{\epsilon}$ dependences are displayed. The spall strength, σ_c , depends on the strain rate according to Eq. (3) up to some value, $\dot{\epsilon}_c$, and then remains nearly constant. The observation of fracture surfaces revealed that the fracture was ductile for all strain rates. The lower rate experiments, $\dot{\epsilon} < \dot{\epsilon}_c$, showed evidence of mature crack formation prior to coalescence failure. The micrographs of the higher rate spalled specimens suggested that failure occurred through void linkup without full crack formation.

In Fig. 5 the dependence of $\dot{\epsilon}_c$ on the parameter K_{Ic}/Y is plotted. The values of ρ and c_0 were determined experimentally. An average of the yield strength and ultimate tensile strength was taken as the flow stress Y . The values of $\dot{\epsilon}_c$ given by Eq. (5) lie well above

Fig. 4. The influence of $\dot{\epsilon}$ on the spall strength σ_c for different microstructures of LAHS steel.

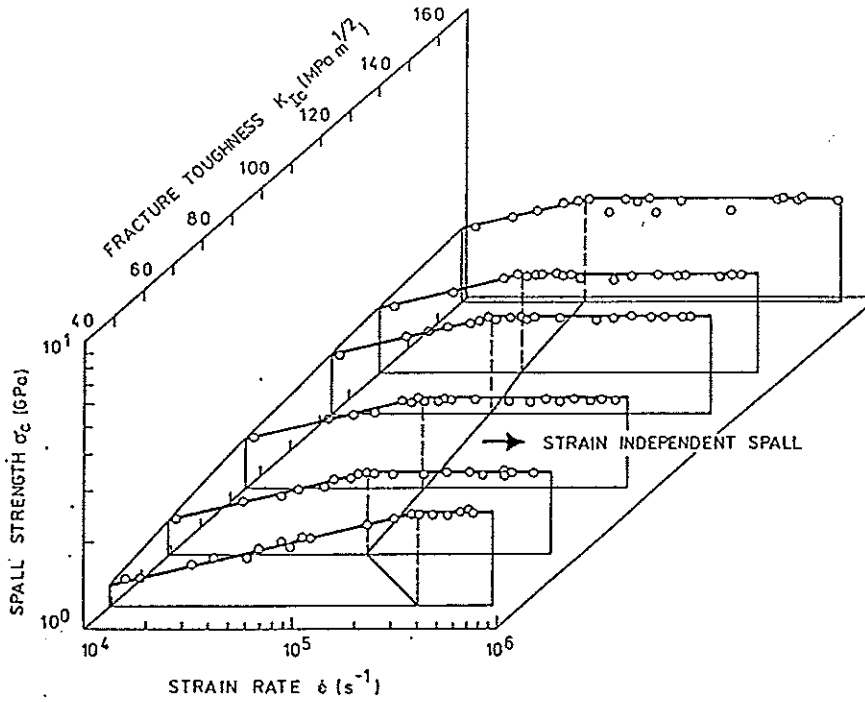
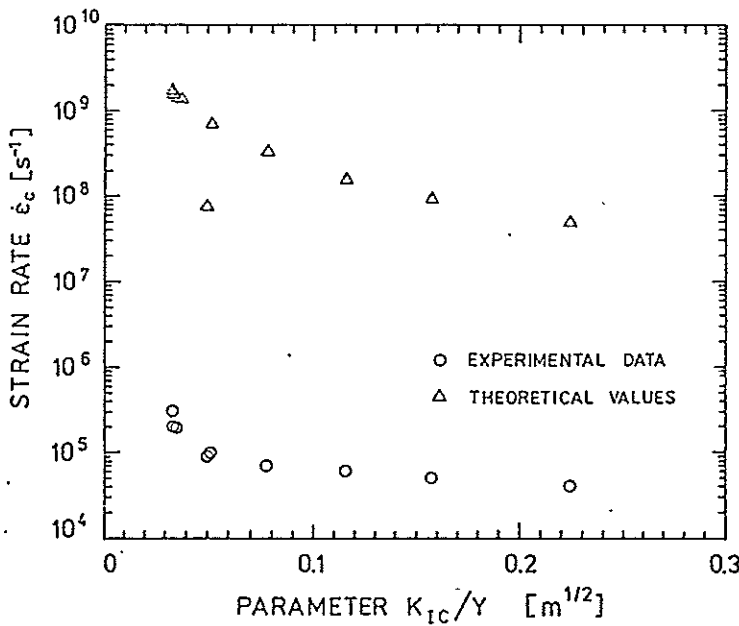


Fig. 5. The dependence of critical strain rate $\dot{\epsilon}_c$ on the K_{IC}/Y parameter.

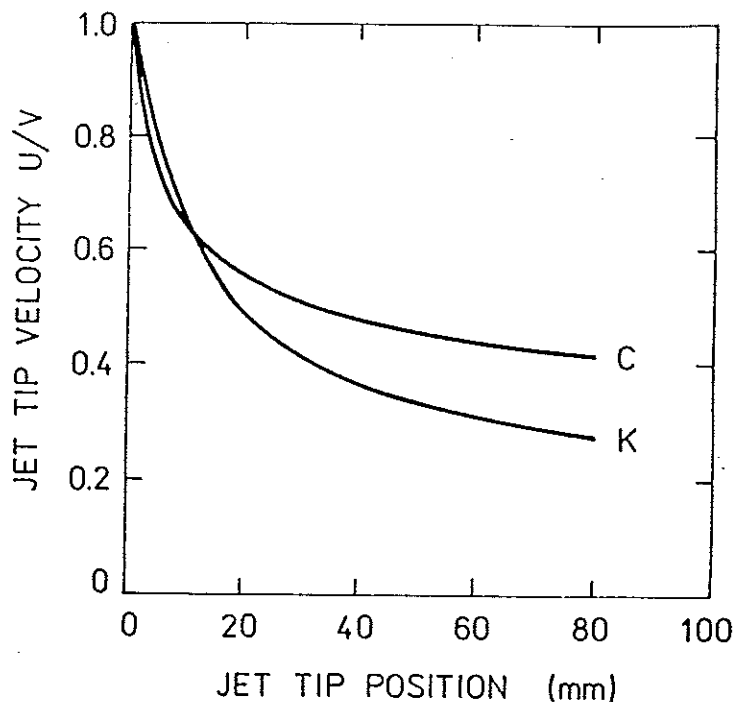


the experimental data. It means the theory of the spall transition given in [Grady 1988] should be modified. These results suggest that the spall behaviour can be predicted by means of the ratio K_{IC}/Y where both quantities depend on the material microstructure.

In the last step we used a very

intensive impact loading, i.e. the impact of shaped charge jet [Walters and Zukas 1989]. When a jet strikes the target it induces high pressures, around 30 GPa, and forces the target material to flow plastically at strain rates reaching $10^6 s^{-1}$ [Walters and Zukas 1989].

Fig. 6. Jet tip velocity, U/V , vs jet tip position x .



Usually, it is taken for granted that material strength is unimportant at first stages of the jet's penetration. It should become important at relatively low jet velocities, i.e. after attaining certain depth of penetration where the penetration velocity, U , is expressed as [Walhers and Zukas 1989]

$$\frac{U}{V} = \frac{1}{2} - \frac{Y_s}{\rho V^2} \quad (6)$$

where V is the impact velocity and Y_s is the strength characteristic of target, e.g., yield strength.

The verification of this supposition is important not only for general understanding of high strain rate behaviour of materials but it also has some practical consequences as e.g. the development of layered armours.

In [Buchar et al. 1993] we performed a serie of time-resolved measurements of the jet penetration velocity. Experimental results displayed in Fig. 6 show that there are two distinct phases of jet penetration. An initial phase is characterized by rapid decrease of the jet tip velocity, the second one displays a nearly constant velocity of penetration.

It was found, see [Buchar et al. 1993], that the penetration velocity reduction at the beginning of penetration was greater in material with lower yield strength. In contrast to the prevailing opinion these results suggest that the structure of the target material plays a role from the very beginning of the penetration process.

As a conclusion we can postulate that the initial microstructure exhibits significant influence on the process of impact loading regardless of its type or strain rate achieved even when damage number, D , exceeds considerably the unity. It also influences whole deformation process through specific microstructure changes which take place in the process. The results presented here call for further reexamination of the relation of microstructure and high strain-rate deformation - impact loading.

NOMENCLATURE

c_0 = elastic wave velocity (m/s), D = damage number (1), K = bulk modulus (GPa), $K_{I1/2}$ = stress intensity factor ($\text{MPa m}^{1/2}$), K_{Ic} = fracture toughness ($\text{MPa m}^{1/2}$), l_0 = crack length (mm), U = jet pe-

netration velocity (m/s), V =
 impact velocity (m/s), Y = yield
 strength (MPa), Y_f = flow stress
 (MPa), Y_s = strength
 characteristic (MPa), β = dynamic
 overstress (1), ϵ = strain (%),
 $\dot{\epsilon}$ = strain rate (s^{-1}), $\dot{\epsilon}_c$ =
 critical strain rate (%), ρ =
 material density ($kg\ m^{-3}$), σ_s =
 static yield strength (MPa), σ_c =
 spall strength (GPa), σ_y = dynamic
 yield strength (MPa), λ = stress
 pulse duration (μs).

REFERENCES

HUTCHINGS I.M. 1983 - The beha-
 viour of metals under ballistic
 impact at sub-ordonance veloci-
 ties. Material Behaviour Under
 High Stress and Ultrahigh Loading
 Rates (J. Mescall and V. Weiss,
 Eds.) Plenum Press, New York and
 London.
 KREJČÍ J., BŘEZINA J., BUCHAR J.
 1992 - The influence of the
 microstructure on the layered
 target response to shaped charge
 jets. Proc. of the 13th Symp. on
 Ballistics - Stockholm.
 BUCHAR J., BÍLEK Z. 1983 - Beha-

viour of Metals under High Strain
 Rates of Loading - Academia,
 Prague.

BUCHAR J. - Crack initiation in
 low alloyed high strength steel
 under stress pulse loading. Acta
 Tech. 37, pp. 445-453.

BUCHAR J., KREJČÍ J., BŘEZINA J.,
 MAJZLÍK J. 1993 - The influence of
 steel target strength on the
 velocity of shaped charge jet.
 Acta Tech. 38; pp. 357-366.

BUCHAR J., ELICES M. 1991 - The
 influence of grain size on the
 spall fracture of copper Journal
 de Physique Vol. IV; pp. 623-630.

KALTHOFF J.F., SHOCKEY D.A. 1977
 - Instability of cracks under im-
 pulsive loads. J. Appl. Phys. Vol.
 48; pp. 986-997.

SHOCKEY D.A., KALTHOFF J.F.,
 EHRLICH D.C. 1983 - Response of
 cracks to short pulse loads. Int.
 J. Fracture Vol. 22; pp. 271-282.

GRADY D.E. 1988 - Incipient spall,
 crack branching and fragmentation
 statistics in the spall process.
 Journal de Physique Vol. IV; pp.
 175-183.

VALTERS V.P., ZUKAS J.A. 1989 -
 Fundamentals of Shaped Charges -
 Wiley, New York.

ANISOTROPY DIAGRAMS AND THEIR APPLICATION TO TERMINAL BALLISTICS

Alain BURIE

Technological Research Centre, Giat Industries
Bourges, FRANCE

Jean CONDOURE

Technological Research Centre, Giat Industries
Tarbes, FRANCE

ABSTRACT

Studies have been made in order to predict the ballistics properties of materials which looks identical. Using ultrasonic characterisation, we have been able to link the measured characteristics with terminal ballistics properties. Easy and cheap measures, using ultrasonic waves, have been made on two identical materials. After firing the results of the ultrasonic wave characterisation and ballistics properties are compared. The results are rather good. Numerical simulations have been made in order to explain the observed phenomenas.

INTRODUCTION

In order to choose between two different manufacturers, ultrasonic wave characterisation have been made of the two products. The static characteristics were the same. After characterisation, the two products has been used as liner for HEAT warheads. After firing, comparison have been made between the jet characteristics and the ultrasonic characteristics. Part one describes the experimental set up that has been used to characterise the materials, part two describes the simulations that has been conducted on the subject, and part three gives an explanation of the results.

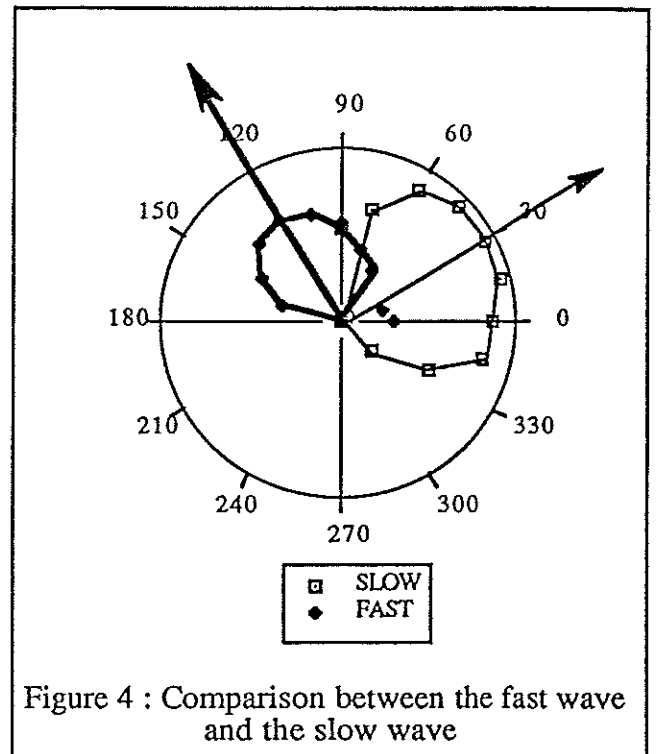
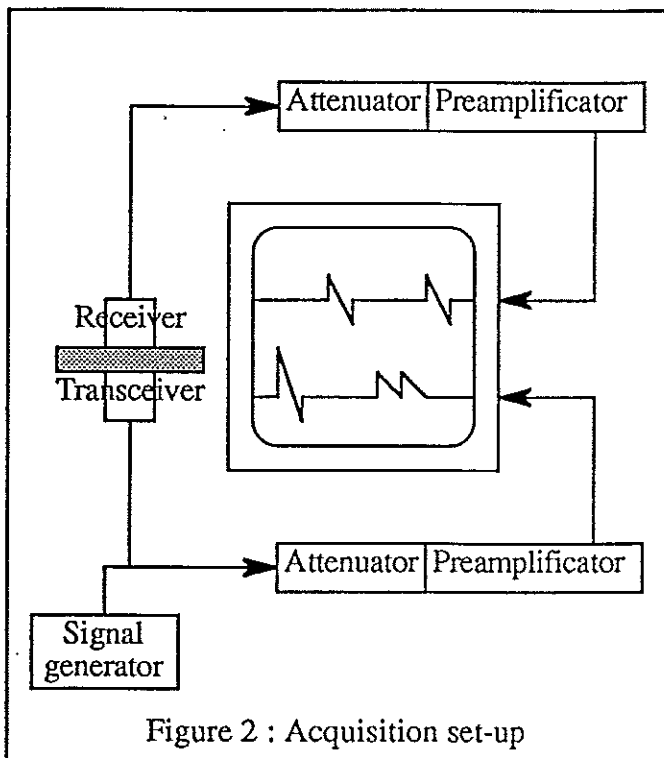
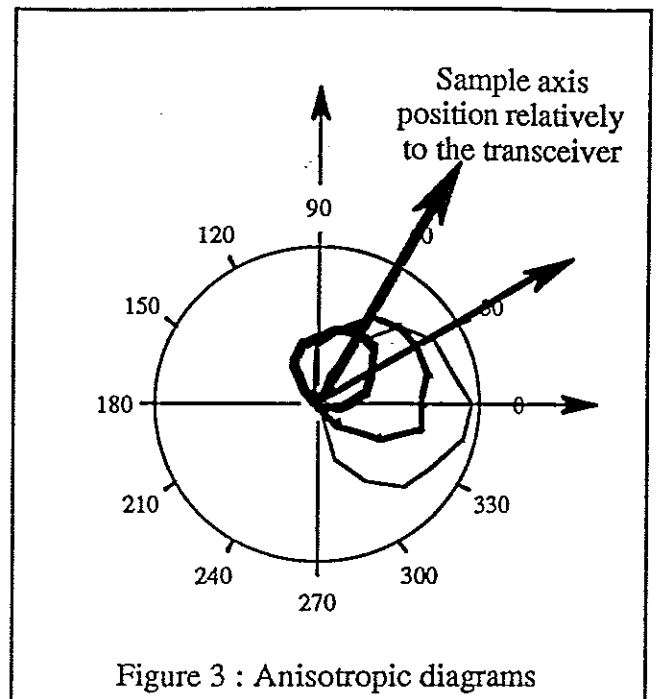
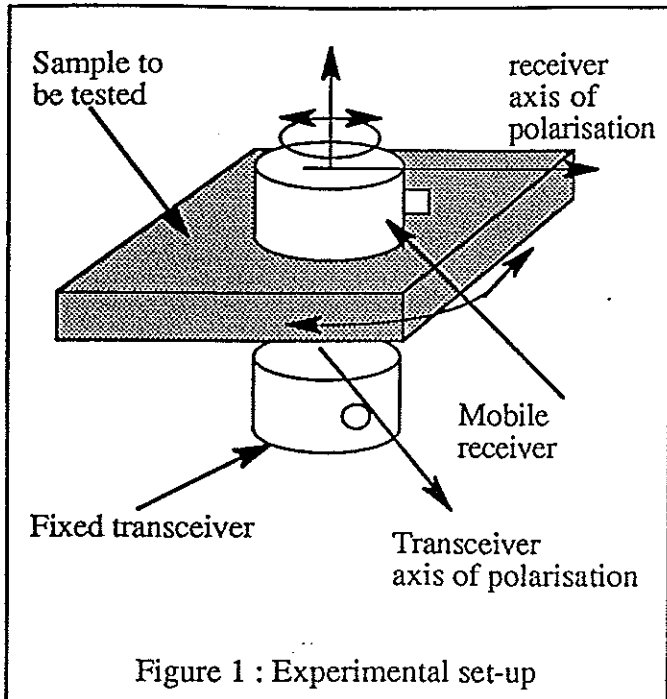
EXPERIMENTAL SET UP

We have measured the ultrasonic characteristics of the two materials in their final phase (that is just before firing). The experimental set up is the following one : a fixed transceiver transmit transverse ultrasonic waves into a plate of the material to be tested. A second receiver is located just over the transceiver, but as it can rotate freely around the vertical axis, the angle of rotation of the ultrasonic wave (Fig.1 gives a scheme of the experimental set up) is measured.

Angles (between the transceiver and the sample and between the transceiver and the receiver) are measured thanks to graduated scales.

The transceiver and receiver are linked to an oscilloscope through an attenuator and a preamplificator (Fig.2. gives a scheme of the acquisition system). The time resolution is adapted to the frequency of the signal (as examples, for a 5 MHz frequency, resolution is inferior to 0.2 μ s, for a 20 MHz frequency, resolution is inferior to 0.05 μ s).

In order to determine when there is a zero angle between the transceiver and the receiver, the receiver is put directly on the transceiver and is



rotated till the signal reaches its maximum value. Then we plot the received signal amplitude as a function of the angles between the transceiver and receiver (θ_1), and between the transceiver and axis of the sample to be tested (θ_2). For each couple, we note the amplitude of the two signals that appear on the scope (as the material is not isotrop, transverse waves arrive at different times on the receiver, and are then differentiated as "fast one" and "slow one"). Figure 3 gives an example of the results obtained for a such a wave. Figure 4 gives

an example of the two waves for the same orientation of the sample. In fact, the two lobes are perpendicular, and as one grows up, the other one decreases proportionally. When rotating the sample, the maximum of propagation of a given wave is always in the same direction (relatively to the material axis), and as the absorption is different along each axis, the two waves are not linked. Using this method, we are able to determine the mechanics characteristics of a material in each direction. The two principal directions are easily

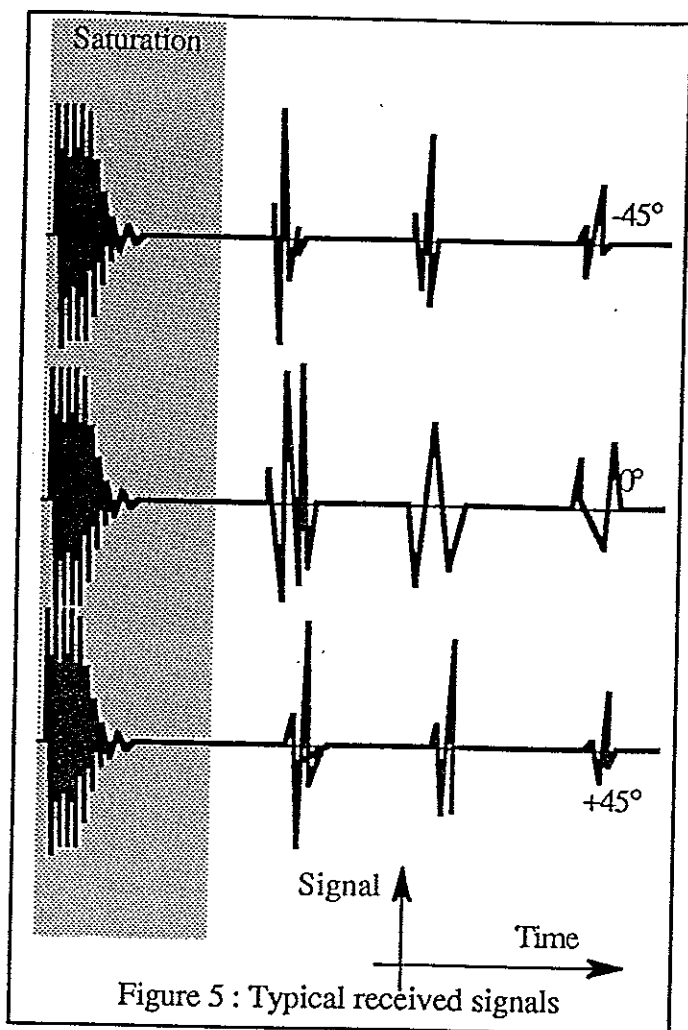


Figure 5 : Typical received signals

detected and characterised. Figure 5 gives a view of typical received signals for angles of -45° , 0° and 45° . On an orthotropic material, the velocities of the two transverse waves are different. As can be seen on the sketch given in figure 5, the two transverse waves arrive at different time, but the received signal is a composition of the two waves, that means that standart measures are unable to separate the two waves. Using our method, we are able to separate the two waves. Tests have been made on two samples of the same material (but manufactured using two different methods). After firing, the most anisotropic material has prove to be the best (jet more stable).

SIMULATIONS

Simulations have been conducted using LS-DYNA3D. We have simulated the propagation of a longitudinal wave and of a transverse wave on three materials, that is an isotropic material, an ortotropic material (with a transverse wave velocity 30% fastest than the other), and an orthotropic material with the same mean transverse waves velocity as the isotropic material. The simulations have been conducted for several duration of the load curve and for several time step scaling factor.

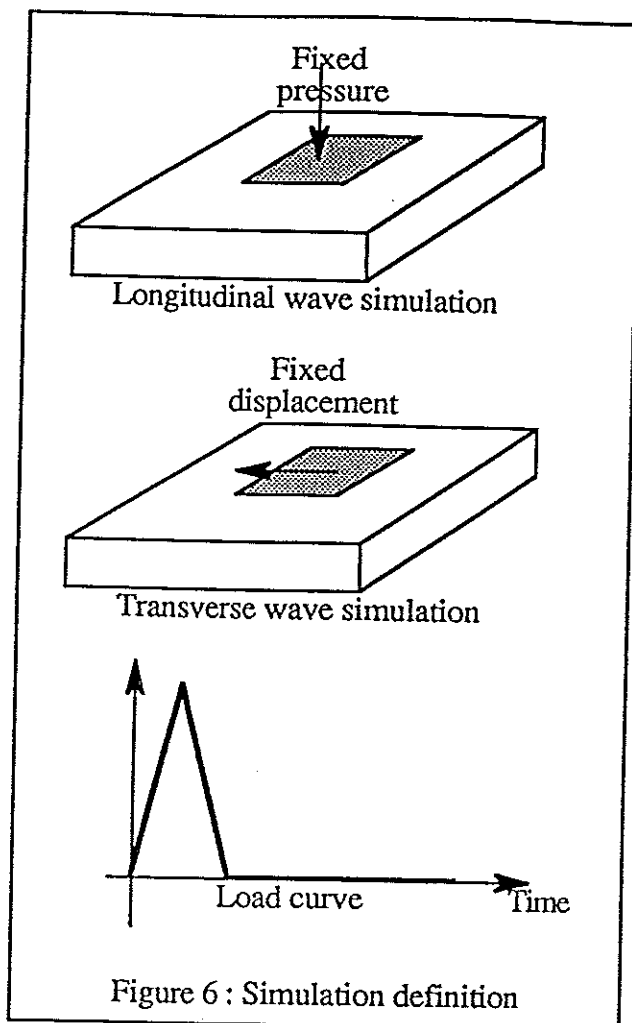


Figure 6 : Simulation definition

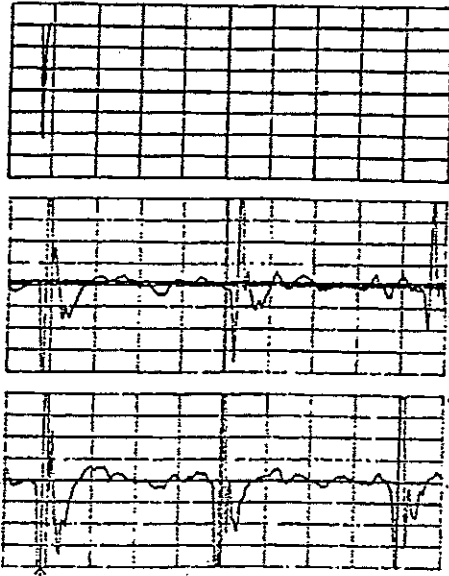
As shown on figure 6, longitudinal waves has been generated by applying a pulse pressure on the top of the sample, and transverse waves by forcing the displacement of the top of the sample.

As it has already be seen experimentally, we have not been able to generate a pure longitudinal wave (or transverse wave), the other kind of wave beeing generated (around 10% of the main wave).

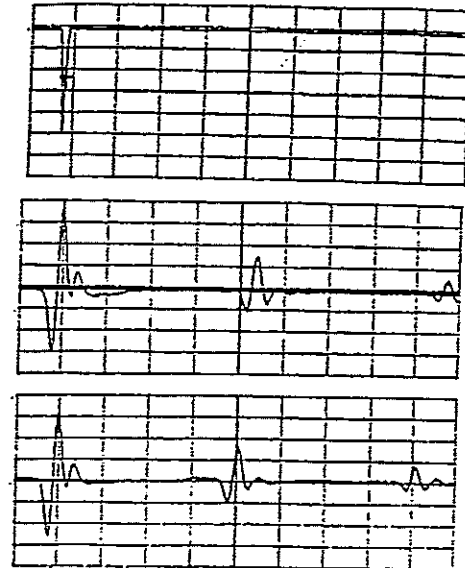
For short pulse duration, the simulation is unable to see the pulse, and if the time step decrease, the longitudinal wave travel faster than predicted by the laws of mechanics. That mean that when using a lagrangian code, the time step being controlled by the smallest cells, waves will propagate at unphysical velocities (this is due to the fact that a "message" propagate from one cell to the other at a velocity of one cell per step).

Figure 7 gives an example of numerical simulation results plotted versus experimental measures.

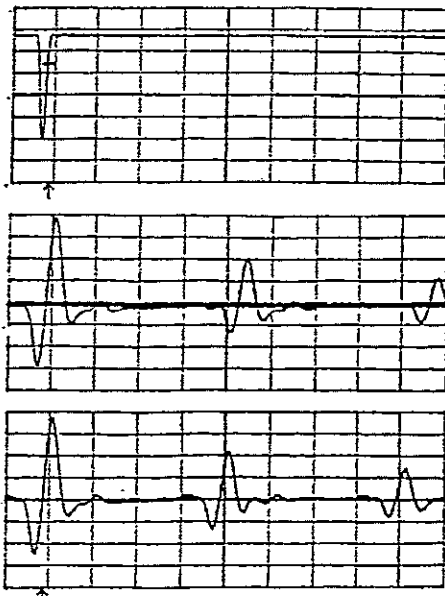
Experimental signal 50 ns
(pulse, fast and slow wave)



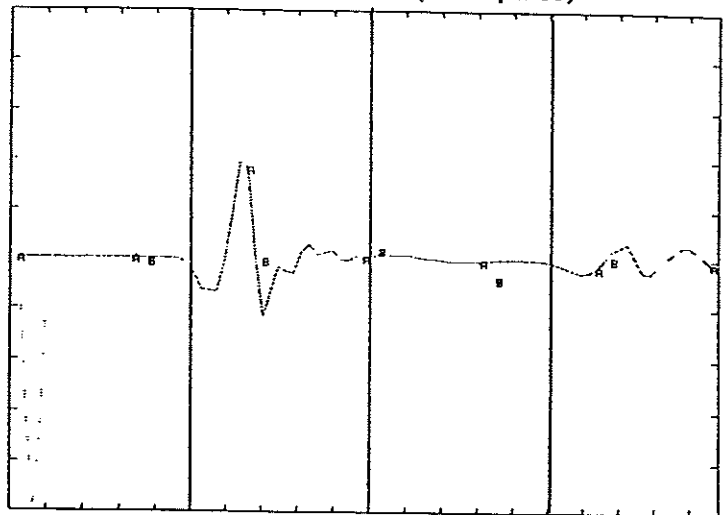
Experimental signal 100 ns
(pulse, fast and slow wave)



Experimental signal 200 ns
(pulse, fast and slow wave)



Simulation result (short pulse)



Simulation result (long pulse)

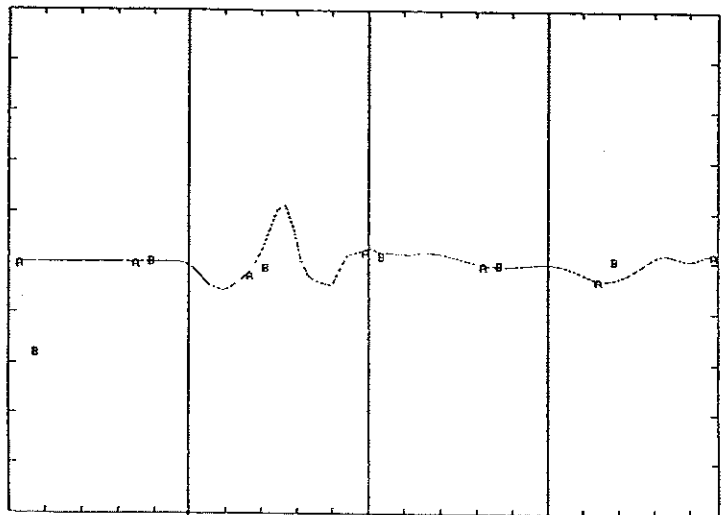


Figure 7 : Simulation results and experimental results

EXPLANATION

We have tried to explain those results. The first explanation is that an initially spherical shock wave propagating into an anisotropic media, will do so as an elliptical wave. As the energy density is located on the surface of the shock, for a given volume of shocked material, the energy per area is less (the area of a ellipsoide is less than that of a sphere). Thus the material can sustain higher shock pressure.

CONCLUSION

Ultrasonic characterisation and waves propagation phenomena can be used to predict the terminal ballistics behaviour of materials.

REFERENCES

BARREAU P., GERARD C., FRIES J.F., TRAVERSE J.P. 1990 - *Influence de la ségrégation dynamique du soufre sur le comportement mécanique du nickel pur* - Acta. metal. mater.

CONDOURE J. 1987 - *Propagation d'une impulsion ultrasonore de type transversal dans les matériaux texturés* - Giat Industries internal report.

CONDOURE J. 1991 - *Caractérisation par ultrasons de matériaux utilisés dans l'armement terrestre : cas des matériaux pour charges formées* - Giat Industries internal report.

CONDOURE J. 1991 - *Caractérisation par ultrasons de matériaux utilisés dans l'armement terrestre : techniques d'analyse* - Giat Industries internal report.

DELACENSERIE D. 1985 - *Influence de l'état de surface et de l'anisotropie de la matière sur la propagation des ultrasons dans les aciers* - Thèse EDF.

GERARD C., BARREAU P., FRIES J.F. 1990 - *Caractérisation mécanique et métallurgique de nuances de nickel de haute pureté* - Giat Industries internal report.

HALLQUIST J.O. 1992 - *LS-DYNA3D user's manual* - LSTC report.

ROBERT A. 1985 - *Polarimètres acoustiques*. - Revue technique de l'armement.

Influence of macro and micro structures of 2124mmc (SiCp) on the behaviours at high strain rate and temperature from 25°c to 550°c

J.C.FU*, C.LABBE* and E.SELLIER**, J.L.LATAILLADE*

*LAMEF, Esplanade des Arts et Métier 33405 TALENCE

**Laboratory of solids chemistry, University of Bordeaux

The composite materials are used more and more widely as the manufacturing needs being daily on the increase. In the field of industries, particularly in the aerospace industry, engineer wish to explore certain kinds of composite material with good performance, which could be easily manufactured at a modest price and used within a large temperature range.

2124mmc(SiCp) is a kind of composite materials with the above-mentioned characteristics. It is a new family of MMC based on Al reinforced with SiCp. Evidently, it is a mixture of metal and ceramics and it possesses the performances of both of them.

This paper presents a part of the result of " WORKABILITY OF METAL AND METAL MATRIX COMPOSITES, IN PARTICULAR Al-Li ALLOYS AND Al BASED COMPOSITE", a research project of CEE. The aim of this project is to develop the production processes by using powder metallurgy techniques for ceramic short fibres reinforcement and to investigate it's characteristics. This technology is suitable for manufacturing extruded or forged composite structural components with high strength metal matrices.

Some physical regularities are introduced in this paper, which help us to explain the behaviour of this material in the plastic domain with a mathematical expression similar to JOHNSON-COOK law, at the high strain rate ($100-300s^{-1}$) and the high temperature (25°c-550°c). We effected tests on HOPKINSON tension bar and considered the influence of temperature for input and output bars.

The results of the tension experiment show that the extension of the material augments as the strain rate rises, however the strength remains insensitive to the strain rate ranged from 100 to 300 (s^{-1}). (In compression tests, we discover that the elastic limit decreases and there is a little change in critic limit as the strain rate ranged from 600 to 1600 (s^{-1})) This material has a high sensitivity to the temperature, the strength and extension decrease with the rising of the temperature.

The research of micro structure supports our macro conclusions and it also explain the physical causes of crack in the particles level . The analysis for different changes of the micro structure at different temperatures, and the comparison of the micro structures between the Al based composite material and Al-Li alloys, allow us to obtain a more comprehensive knowledge about this material.

RESPONSE OF VARIOUS POLYMERS TO IMPACT LOADING

A.M. Hamouda and M.S.J. Hashmi

School of Mechanical & Manufacture Engineering, Dublin City University , Ireland

ABSTRACT

Polymers are increasingly being used in applications where they are liable to be subjected to rapid loading. Examples of such uses include aircraft components exposed to particle impact, crash helmets, aerospace vehicles, and various military applications. However, compared to metals, relatively few studies of their mechanical properties at high strain rate have been carried out.

This paper presents the dynamic stress-strain behaviour of Nylon 6, Nylon 66 (polyamide), Polycarbonate, and Polyethylene subject to a wide range of high strain rate compressive loading. A one dimensional rate dependent constitutive flow model has been developed. A combined experimental and numerical technique has been used to determine the material constants of the proposed flow model.

The effect of water saturation in the mechanical properties of Nylon 6 and Nylon 66 has also been investigated.